

Diss. ETH No. 18435

ENERGY MANAGEMENT STRATEGIES FOR HYBRID ELECTRIC VEHICLES

A dissertation submitted to
ETH ZURICH

for the degree of
Doctor of Science

presented by
Daniel Ambühl

Dipl. Ing. ETH in Mechanical Engineering
born October 5, 1979
citizen of Davos, Graubünden

accepted on the recommendation of
Prof. Lino Guzzella, examiner
Prof. Sergio M. Savaresi, co-examiner

2009

Daniel Ambühl
daniel.ambuehl@alumni.ethz.ch

2009

ETH Zürich
Measurement and Control Laboratory
Sonneggstrasse 3
8092 Zürich, Switzerland

printed by
www.onlinedruck.ch
in a climate-neutral process

IMRT  *Institut für Mess- und Regeltechnik
Measurement and Control Laboratory*

 **myclimate**
Protect our planet

For my family, Patricia, and the mountains

Acknowledgments

First of all, I would like to thank my supervisor, Prof. Dr. Lino Guzzella, for the continuous support throughout my doctoral study, for organizing the funding, for the confidence he expressed in me, and for the great academic freedom he gave me. Further, I am grateful to Prof. Dr. Sergio Savaresi who accepted to be my co-examiner.

I want to greatly acknowledge Robert Bosch GmbH for the funding of this project, that was initiated by Dr. Karsten Mann and continued by Dr. Jan Lichtermann. Further, special thanks go to Dr. Sandra Sterzing-Oppel and Thomas Huber from Robert Bosch GmbH for the fruitful technical discussions and for proofreading my publications. I also want to thank Martin Pulfer from the Swiss Federal Office of Energy (BfE) for his interest in my research and the co-funding.

The time I spent at the Control and Measurement Laboratory was very enjoyable and inspiring to me. I wish to thank all my colleagues for the great working environment and the in-depth technical discussions. I want to express a special thank to Dr. Chris Onder and Dr. Antonio Sciarretta for their valuable advices they gave me in many discussions. Further, I want to thank Olle Sundström for the excellent collaboration, resulting in two joint publications. I also want to thank Dr. Markus Wiesendanger, Moritz Oetiker, Matthias Schibli, Christian Dönitz and Daniel Rupp for the great discussions and the hints in many topics.

Finally, I would like to express my overwhelming gratitude to my family and Patricia. Their support and encouragement were important to me to realize this dissertation.

Zürich, June 22, 2009

Daniel Ambühl

Abstract

Hybrid electric vehicles are commonly known as a promising solution to reduce the fuel consumption with existing technology for the near future. Due to the presence of at least two power converters in the powertrain, there is a new degree of freedom compared to conventional vehicles. An appropriate control of this degree of freedom is required to achieve lowest possible fuel consumption.

The objective of this thesis is to develop novel control algorithms for the before mentioned degree of freedom in order to minimize fuel consumption. These algorithms are evaluated in simulations, but finally, they have to be applicable to real vehicles. Therefore, the algorithms must be causal, which means that they can only exploit information available in the present and the past. Further, they have to be computationally very efficient, since the computational power and the memory capacity in the engine control unit are limited.

This objective is approached by first evaluating the global optimum with dynamic programming as a benchmark for any real-time capable control strategies. Such globally optimal solutions are acausal and can only be evaluated in simulation. In this thesis, a new method is presented that allows to enhance the accuracy and the computational efficiency of dynamic programming for single-state optimal control problems with final state constraints.

Causal control strategies are derived and investigated in a second step. A simplified model for the hybrid powertrain is introduced in addition to the original model. This simplified model allows to derive explicit solutions for the optimal control, resulting in a strategy that is computationally very attractive and allows to gain insight into its structure. An investigation of these causal control strategies with the original and the simplified model has shown, that they achieve very good performance in terms of fuel consumption as long as there are no severe recuperation phases. For driving cycles with elevation profiles, the fuel consumption achieved by

these strategies differ significantly from the theoretical optimum.

In order to extend these strategies such that they show good performance even in environments with elevation profiles, some knowledge on the future driving conditions is taken into account. A novel algorithm has been developed in this thesis that evaluates a reference trajectory for the future state-of-charge of the battery such that low fuel consumption can be achieved in conjunction with the previously proposed strategy even in driving conditions with elevation changes. This algorithm exploits data from the navigation system on the trip that is planned such as the topographic profile and the average traveling speeds on each road segment. This predictive algorithm is computationally very efficient and the resulting fuel consumption is improved considerably compared to the non-predictive strategy.

In a last step, the optimal starting and stopping decision for the engine has been investigated. For the case of a full electric hybrid, it is optimal to shut the engine off for some time intervals and to drive electrically. However, if there is no cost in terms of fuel consumption assigned to an engine start, the solutions resulting from optimal control can show frequent starting and stopping of the engine. In order to approach this problem systematically, modeling of the energetic cost assigned to each engine start is required. An investigation of the optimal solution of the energy management problem including starting cost has shown, that this energetic starting cost cannot be neglected for an appropriate control. A model predictive control scheme is introduced for the decision on the engine operation. The performance in terms of fuel consumption of this model predictive control is evaluated as a function of the prediction horizon. These results revealed that a very short prediction horizon is sufficient to achieve close to optimum performance.

Zusammenfassung

Elektrische Hybridfahrzeuge stellen eine vielversprechende Lösung dar, um den Treibstoffverbrauch mit bestehender Technologie für die nahe Zukunft zu reduzieren. Die Verfügbarkeit von mindestens zwei Leistungsquellen im Antriebsstrang ergibt einen zusätzlichen Freiheitsgrad im Vergleich zu konventionellen Fahrzeugen. Eine geeignete Steuerung dieses Freiheitsgrades ist notwendig um einen tiefst möglichen Treibstoffverbrauch zu erzielen.

Das Ziel dieser Arbeit ist die Entwicklung neuer Regelalgorithmen für den erwähnten Freiheitsgrad, so dass der Treibstoffverbrauch minimiert wird. Diese Algorithmen werden zwar in Simulationen untersucht, letztlich müssen sie jedoch im echten Fahrzeug eingesetzt werden können. Folglich müssen diese Algorithmen kausal sein. Dies bedeutet, dass sie nur Informationen aus der Gegenwart und der Vergangenheit ausnützen dürfen. Des Weiteren müssen sie recheneffizient sein, da die Rechenleistung und die Speicherkapazität im Motorsteuergerät begrenzt sind.

Um dieses Ziel zu erreichen, wird zuerst das globale Optimum mittels Dynamischer Programmierung als Referenz für echtzeitfähige Regelstrategien ausgewertet. Solche global optimalen Lösungen sind akausal und können nur in Simulationen gefunden werden. In dieser Arbeit wird eine neue Methode gezeigt, welche es erlaubt, die Präzision und die rechnerische Effizienz der Dynamischen Programmierung für skalare, optimale Regelungsprobleme mit beschränktem Endzustand signifikant zu verbessern.

Kausale Regelstrategien werden in einem zweiten Schritt hergeleitet und untersucht. Zusätzlich zum ursprünglichen Modell des hybriden Antriebsstranges wird ein vereinfachtes Modell eingeführt. Dieses vereinfachte Modell erlaubt die Herleitung expliziter Lösungen für die optimale Regelung, was zu einer Strategie führt, welche rechnerisch attraktiv ist und eine klare Struktur aufweist. Die Untersuchung dieser kausalen Strategien, welche auf dem ursprünglichen und dem vereinfachten Modell basieren, hat aufgezeigt, dass diese sehr gute Resultate bezüglich Treibstoffver-

brauchs erzielen, solange keine drastischen Rekuperationsphasen vorliegen. Für Fahrmuster mit Höhenprofil hingegen, weicht der Treibstoffverbrauch, welcher mit solchen Strategien erzielt wird, deutlich vom theoretischen Optimum ab.

Die bisher entwickelten Strategien wurden so erweitert, dass sie Informationen über das zukünftige Fahrmuster berücksichtigen, damit auch in hügeligen Umgebungen gute Treibstoffverbräuche erzielt werden. In dieser Arbeit wurde ein neuer Algorithmus entwickelt, welcher eine Referenztrajektorie für den zukünftigen Ladestand der Batterie vorgibt, so dass, in Kombination mit der bestehenden kausalen Strategie, tiefst mögliche Treibstoffverbräuche auch in Fahrmustern mit Höhenprofil erzielt werden können. Dieser Algorithmus nutzt Daten über die geplante Fahrstrecke aus dem Navigationssystem. Diese Daten bestehen aus dem Höhenprofil und den durchschnittlichen Reisegeschwindigkeiten der jeweiligen Streckenabschnitte. Dieser prädiktive Algorithmus ist rechnerisch sehr effizient und der erzielte Treibstoffverbrauch ist gegenüber der nicht-prädiktiven Strategie deutlich verbessert.

Als letzter Schritt wurde die optimale Start/Stop-Entscheidung für den Verbrennungsmotor untersucht. Im Falle eines Vollhybridfahrzeuges ist es in gewissen Zeiträumen optimal den Verbrennungsmotor abzuschalten und rein elektrisch zu fahren. Wenn allerdings für einen Start des Verbrennungsmotors keine Kosten betreffend Treibstoffverbrauch berücksichtigt sind, resultiert in Lösungen aus der optimalen Regelung häufiges Starten und Stoppen des Motors. Um dieses Problem systematisch anzugehen, müssen diese energetischen Startkosten modelliert werden. Die Untersuchung der optimalen Lösung des Energiemanagementproblems mit Startkosten hat gezeigt, dass diese Kosten in der Regelstrategie nicht vernachlässigt werden sollten. Eine modellbasierte prädiktive Regelung für den Betrieb des Verbrennungsmotors wurde eingeführt und der erzielte Treibstoffverbrauch dieser modellbasierten prädiktiven Regelung wurde als Funktion des Prädiktionshorizontes untersucht. Die Resultate haben gezeigt, dass ein sehr kurzer Prädiktionshorizont ausreicht, um Treibstoffverbräuche zu erzielen, welche nahe beim theoretischen Optimum liegen.

Wenn man sich überlegt, dass die Mona Lisa mit lauter einzelnen Pinselstrichen entstanden ist . . .

Mani Matter, 1936–1972, in Tagebuch I (1958–1961)

Contents

Abstract	ii
Zusammenfassung	iv
1 Introduction	1
1.1 Motivation	1
1.2 Goals of the Project	3
1.3 Contributions	3
1.4 Structure of the Thesis	5
2 Model of the Parallel HEV	7
2.1 Chassis Model	8
2.2 Gearbox	9
2.3 Torque Coupler	10
2.4 Internal Combustion Engine	11
2.5 Electric Motor	12
2.6 Battery	13
2.7 Auxiliary Systems	15
3 Dynamic Programming	17
3.1 Problem Formulation	18
3.2 Basic DP Algorithm	20
3.3 Numerical Issues	22
3.4 Boundary Line Method	24
3.4.1 Computation of the Boundary Line	25
3.4.2 Interpolation Near the Boundary Line	27
3.5 Example: Optimal Fishing	28
3.5.1 Continuous-Time Problem	29
3.5.2 Discrete-Time Problem	30
3.5.3 Resolution Study	31

3.5.4	Computational Effort	34
3.6	Application on the Hybrid Vehicle	36
3.7	Conclusions	38
4	From Optimal Toward Causal Control	39
4.1	Pontryagin's Minimum Principle	40
4.1.1	Necessary Conditions for Optimality	41
4.1.2	Physical Interpretation of the Necessary Conditions	42
4.1.3	Two-Point Boundary Value Problem	43
4.2	Causal Approach	46
4.2.1	Derivation of Causal Control with SoC-Penalty . . .	46
4.2.2	Summary of the Causal Control: ECMS	49
4.2.3	Results and Limitations of the ECMS	51
4.3	Optimal Control with a Simplified Model	54
4.3.1	Optimal Control with Unconstrained, Speed-Independent Model	54
4.3.2	Optimal Control with Input-Constrained and Speed-Dependent Model	66
4.3.3	Model Validation	74
4.3.4	Application of Simplified Model	77
4.3.5	Conclusions for the Simplified Model	79
5	Predictive Control for the State-of-Charge	81
5.1	Method	82
5.1.1	Prediction of Recuperation Time Segments	83
5.1.2	Synthesis of an SoC Reference Trajectory	85
5.2	ECMS with Predictive Reference Signal Generator	89
5.2.1	Definition of Test Framework	89
5.2.2	Simulation of the Navigation System	90
5.3	Simulation Results	91
5.4	Conclusions	92
6	Predictive Engine Start/Stop Decision	97
6.1	Model of the Hybrid Powertrain Including Engine Start . .	98
6.1.1	ICE Start	98
6.1.2	ICE Stop	100
6.1.3	Combined Backward/Forward Approach	101
6.2	Optimal Control	102

6.2.1	Three Different Models	102
6.2.2	Results from DP for the Three Models	103
6.2.3	Sensitivity Analysis	103
6.3	Suboptimal Control	106
6.3.1	Model Predictive Control	106
6.3.2	Simulation Results	107
6.4	Conclusion	108
7	Summary & Conclusions	111
	Appendix	115
A	Nomenclature	115
B	Regulatory Driving Cycles	118
C	Power Limits	120
D	Matrices of the QP	122
E	Construction of the Simulated Data Output of the Navigation System	124
	Curriculum Vitae	130

Chapter 1

Introduction

Ecological awareness and economical reasons call for a substantial reduction of the fuel consumption of all future automobiles. Conventional vehicles propelled by internal combustion engines (ICEs) profit from the very high energy density of gasoline or diesel fuel, but suffer from a low part-load efficiency. Hybrid electric vehicles (HEVs) represent a promising approach to reduce the fuel consumption considerably using existing powertrain components. HEVs improve the overall efficiency by:

1. downsizing of the engine to reduce friction losses and compensating for the lacking power by the electric motor,
2. recuperating kinetic and potential energy during braking phases by using the electric path instead of the conventional brakes,
3. shutting off the engine during standstill to avoid idling losses, and
4. avoiding part-load operation of the engine by shifting these operating points to higher torques or shutting off the engine and driving in the electric-only mode.

1.1 Motivation

The new degree of freedom available in HEVs, namely the power distribution between the engine and the electric motor, must be judiciously exploited to achieve the best possible fuel economy. In literature, strategies that control this power distribution within the hybrid powertrain are often referred to as *energy management strategies* [1]. Such strategies are typically divided into two groups, namely heuristic strategies and optimal strategies.

Heuristic approaches are often applied in real-time implementations. Low fuel consumption can be achieved, but the performance is very sensitive to the tuning of the rules. This sensitivity becomes important, when the tuning is carried out for a standard driving cycle and the driving patterns that occur in reality differ considerably from the cycle used for the tuning. This results in an increased fuel consumption compared to what would be possible to achieve. A typical rule-based method is fuzzy logic as it was used by the authors of [2, 3]. Such heuristic control strategies are in general not scalable, since these rules are often not model-based. A different approach is presented in [4], where the results obtained from dynamic programming are deployed to extract rules.

Optimal strategies on the other hand, are typically derived with methods from optimal control theory and are using an appropriate physically based model. Such strategies are often minimizing a local cost function at every time-step to find the control signal. This proved to achieve low fuel consumption. Such a local cost function is typically an equivalent fuel consumption that consists of the actual fuel consumption and a weighted electric consumption. These approaches were introduced by the authors of [5, 6, 7] and further improved in [8, 9]. These local minimization strategies require a model of the powertrain and are easily scalable as a consequence. However, such strategies typically require more computational power than rule-based methods, since an online optimization has to be carried out in real-time operation. In [10, 11], Pontryagin's minimum principle was used to derive similar strategies that minimize a local cost function.

The performance of any energy management strategy strongly depends on the information available [12]. Truly optimal fuel consumption can be achieved only if the entire driving cycle is perfectly known a priori. The resulting strategy is not causal, but defines a benchmark to which any causal strategy can be compared to. Dynamic programming (DP) [13, 14] is well suited to find such an optimal solution for the problem at hand. Notice that in some situations acausal solutions might be useful even in practical situations. The authors of [15], for example, present an acausal supervisory control that optimizes the fuel consumption of a hybrid electric bus for repeatedly driven routes.

1.2 Goals of the Project

The goal of this project was to develop control strategies that decide on the power distribution between electric motor and engine in order to minimize the fuel consumption over some driving cycle. The main focus was on full parallel hybrid electric vehicles. Since the aim of these strategies is to be applicable in real-time on the engine control unit, they must be computationally efficient and they have to be causal. Furthermore, the strategies have to be applicable to various dimensions of the components without the need for extensive re-tuning. Therefore, the strategies have to rely on physical models. Such model-based strategies are not only easier to transfer to other component dimensions, they are also well suited for diagnosis during vehicle operation to detect changes or defects in some components.

1.3 Contributions

The research carried out within the framework of this dissertation lead to the following scientific publications:

- D. Ambühl, A. Sciarretta, C. H. Onder, L. Guzzella, S. Sterzing, K. Mann, D. Kraft, M. Küsell, “A Causal Operation Strategy for Hybrid Electric Vehicles based on Optimal Control Theory”, *In Proceedings of the 4th Symposium on Hybrid Vehicles and Energy Management*, Braunschweig, Germany, 2007.
- Olle Sundström, Daniel Ambühl, Lino Guzzella, “On Implementation of Dynamic Programming for Optimal Control Problems with Final State Constraints”, *In Proceedings of Les Rencontres Scientifiques de l’IFP: Advances in Hybrid Powertrains*, Rueil-Malmaison, France, 2008.
- Olle Sundström, Daniel Ambühl, Lino Guzzella, “On Implementation of Dynamic Programming for Optimal Control Problems with Final State Constraints”, *Oil & Gas Science and Technology — Rev. IFP*, 2009, accepted for publication.

- Daniel Ambühl, Lino Guzzella, “Predictive Reference Signal Generator for Hybrid Electric Vehicles”, *IEEE Transactions on Vehicular Technology*, accepted for publication.
- Daniel Ambühl, Olle Sundström, Antonio Sciarretta, Lino Guzzella, “Explicit Optimal Control Policy and its Practical Application for Hybrid Electric Powertrains”, *Control Engineering Practice*, submitted for publication.

The first publication is a conference paper. The novelty presented in this paper is the acausal evaluation of the optimal equivalence factor by means of Hamilton-Jacobi-Bellman-theory together with dynamic programming. Finally, this optimal equivalence factor is approximated to derive a causal strategy.

The second publication has been published on a conference and it is accepted to be reprinted in a journal being the third publication. In these publications, a novel method is presented that allows to improve the accuracy and the computational efficiency of dynamic programming significantly. This method is referred to as *boundary line method* and applies to single-state optimal control problems with final state constraints.

The fourth publication has been submitted to the journal in July 2008 and is accepted for publication. A novel algorithm is presented that allows to reduce fuel consumption significantly in driving cycles with elevation profile. This algorithm is called *predictive reference signal generator*. It only requires data on the topography of the future trip and the average traveling speeds on these future road segments. Real-time capability of this algorithm is achieved by formulation as a quadratic program.

The fifth publication has been submitted in April 2009 and is also in the journal’s reviewing process. A simplified model for a parallel hybrid powertrain is presented and validated. This model allows to derive a novel explicit optimal control law for the energy management problem. This control law can be represented as simple analytical rules that rely on powertrain parameters only. This explicit control law requires very little computational effort and further allowed to derive an analytic expression of a saturation for the equivalence factor. This can be used to introduce an anti-windup scheme, which to the author’s knowledge is novel in the field of equivalent consumption minimization strategies.

1.4 Structure of the Thesis

This thesis is organized as follows. The model of the full parallel electric hybrid vehicle is introduced in Chapter 2. In Chapter 3, the optimal control problem is formulated and dynamic programming is introduced briefly. The main part of this chapter introduces a new method to improve the accuracy and the computational efficiency of dynamic programming for single-state problems with final state constraints. The step from an optimal, but acausal strategy toward a suboptimal, but causal strategy is shown in Chapter 4. In Chapter 5, a method is introduced that allows to extend the previously developed causal strategy such that information on the future driving conditions can be taken into account. This information consists of the topographic profile and the average traveling speed expected for the future road segments. Chapter 6 extends the model with costs for each engine start. An investigation on the energetic impact of these starting cost is carried out and a predictive control is introduced. The required prediction horizon is investigated. Finally, the the main findings of this research are summarized in Chapter 7.

Chapter 2

Model of the Parallel HEV

The vehicle studied in this thesis is a full parallel HEV. Parallel means that the engine and the electric motor act on the same shaft. The connection is often realized by mounting the electric motor directly on the shaft, but it can also be coupled to the shaft by means of a belt or some gears. A full HEV is characterized by the capability for pure electric driving. In a parallel configuration, this typically requires a controllable clutch between the engine and the electric motor, such that the engine can be decoupled from the rest of the powertrain. If this clutch is missing, the vehicle is typically referred to as ‘mild’ parallel HEV. Theoretically, pure electric driving would still be possible. However, this would require the motor to drag the engine during electric propulsion. As it has been shown in [16], pure electric driving is energetically not favorable for ‘mild’ parallel HEVs.

The topology of this full parallel HEV is illustrated in Fig. 2.1. The parameters of the vehicle are those of a midsize passenger car with a mass of 1580 kg, a maximum power of the spark-ignition (SI) engine of 80 kW, a maximum power of the electric motor of 25 kW, and a NiMH-battery with a capacity of 6.2 Ah at a nominal voltage of 230 V. The energy content of this battery is comparable with the traction battery used in the Toyota Prius, Generation III.

As discussed in [17, 18], a quasi-static ‘backward’ approach is used to model the vehicle. The ‘backward’ approach is well suited for the actual problem statement: The speed profile $v(t)$ and the corresponding road grade $\gamma(t)$ are prescribed externally, i.e., they are considered to be disturbances. The ‘quasi-static’ approach assumes that the speeds, accelerations, and loads of powertrain components can be considered to be constant over one sample time. This allows for considerable reduction of the simulation time. The assumption of quasi-static signals can be justified by compar-

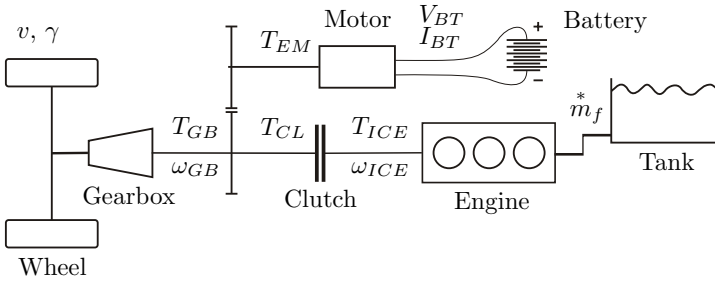


Figure 2.1: Topology of the full parallel hybrid electric powertrain.

ing the time constants of the relevant dynamics of the powertrain to the time constants of the dynamics that are neglected. In [19], this assumption has been verified for engines of passenger cars. It is obvious that this assumption is also valid for electric machines because the time constants of the electric components are even smaller than those being present in combustion engines.

In the following, the relevant powertrain components shown in Fig. 2.1 are being discussed with their respective inputs, outputs, and, for dynamically modeled components, state-variables. Effects caused by changes of the temperatures of the battery, the electric motor, and the engine are neglected throughout this work. The parameters of the powertrain are summarized in Table 2.1.

2.1 Chassis Model

The chassis model encompasses all parts of the vehicle that yield the relation between speed $v(t)$, acceleration $\dot{v}(t)$, road grade γ , and the resulting speed ω_{WH} , acceleration $\dot{\omega}_{WH}$, and torque T_{WH} at the gearbox output, which is the 'wheel-side' of the gearbox. For this relation, the vehicle mass, its aerodynamic properties, wheel properties, and transmission ratio of the final drive are relevant. The tractive force F_t required at the wheel is the sum of the force due to inertia F_i , the aerodynamic drag F_a , the rolling

friction force F_r , and the force induced by gravity F_g . This results as

$$F_t = F_i + F_a + F_r + F_g, \quad (2.1)$$

where

$$F_i = m_v \cdot \dot{v}(t) \quad (2.2a)$$

$$F_a = \frac{1}{2} \rho_a A_f c_d v^2(t) \quad (2.2b)$$

$$F_r = (c_{r,1}v + c_{r,0}) \cdot m_v g \cos(\gamma) \quad (2.2c)$$

$$F_g = m_v g \sin(\gamma). \quad (2.2d)$$

The parameter m_v is the vehicle mass, ρ_a the density of the air, A_f the frontal area of the vehicle, c_d its aerodynamic drag coefficient, $c_{r,1}$ and $c_{r,0}$ the rolling friction coefficients, and g the gravitational acceleration.

The torque and speed required at the gearbox output can be computed with the tractive force and the speed by

$$\omega_{WH} = \frac{v}{r_{WH}} \quad (2.3)$$

$$\dot{\omega}_{WH} = \frac{\dot{v}}{r_{WH}} \quad (2.4)$$

$$T_{WH} = \begin{cases} r_{WH} F_t + \Theta_{WH} \frac{\dot{v}}{r_{WH}} + T_{WH,loss}, & \text{if } v > 0 \\ 0, & \text{if } v = 0 \end{cases}, \quad (2.5)$$

where r_{WH} is the effective wheel radius, Θ_{WH} the wheel's inertia, and $T_{WH,loss}$ a constant loss torque.

2.2 Gearbox

The gearbox is modeled including the gear ratio of the final drive. The efficiency η_{GB} of the gearbox is assumed to be constant. The resulting speed and torque required at the gearbox input to satisfy the requested speed and torque at the wheel are calculated by

$$w_{gb} = \nu_{GB}(k_{GB}) \cdot \omega_{wh} \quad (2.6)$$

$$\dot{w}_{gb} = \nu_{GB}(k_{GB}) \cdot \dot{\omega}_{wh} \quad (2.7)$$

$$T_{GB} = \begin{cases} \frac{T_{WH}}{\eta_{GB} \cdot \nu_{GB}(k_{GB})}, & \text{if } T_{WH} \geq 0 \\ \frac{T_{WH} \cdot \eta_{GB}}{\nu_{GB}(k_{GB})}, & \text{if } T_{WH} < 0, \end{cases} \quad (2.8)$$

where k_{GB} is the selected gear number and $\nu_{GB}(k_{GB})$ the corresponding transmission ratio.

The gear switching strategy is assumed to be defined by the manufacturer of the gearbox and is therefore not part of the energy management for the HEV. The strategy used throughout this thesis is a purely speed-based strategy as illustrated in Fig. 2.2. This figure shows that there is a hysteresis to avoid too frequent switching if the vehicle speed is close to one of the thresholds. The arrows indicate what characteristic is relevant for upshifts and downshifts, respectively.

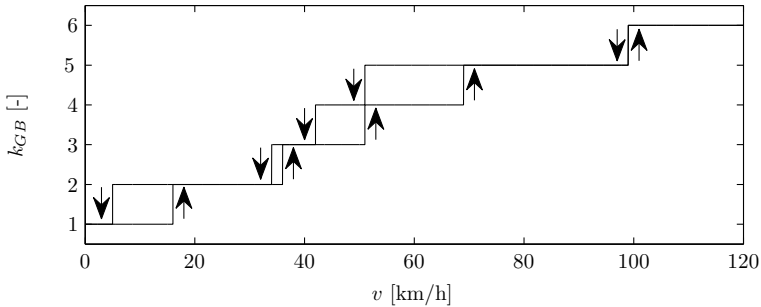


Figure 2.2: Speed-dependent gear switching.

2.3 Torque Coupler

The electric motor is directly connected to the shaft of the gearbox input. Therefore, the transmission ratio between electric motor and gearbox input is one and consequently not explicitly expressed in the following. The node where the torques of the electric motor and the engine are superposed is called torque coupler. The following torque balance must be satisfied:

$$T_{GB} = T_{ICE} + T_{EM}. \quad (2.9)$$

Due to limitations of engine and motor torque, it can happen that this torque balance is not satisfied. Torque demands which are high, i.e., $T_{GB} > T_{ICE,max} + T_{EM,max}$, result in an infeasible torque balance (2.9). If this happens, the driving cycle is infeasible. On the other hand, high negative torque demands $T_{GB} < T_{EM,min}$ cannot satisfy the torque balance (2.9), too. This case represents strong braking phases that cannot be

captured by the electric motor anymore. Hence, the conventional brakes supply the torque difference. Since the actuation of the conventional brakes is obvious from an energetic point of view, these are not modeled explicitly.

As a consequence of the torque balance (2.9), the operation points of the powertrain are fully determined by choosing either the engine torque or the torque of the motor. For consistency with the common literature, the motor torque is chosen as the control input. Normalized with the requested torque at the gearbox, the control signal u is defined as the split factor

$$u = \frac{T_{EM}}{T_{GB}}. \quad (2.10)$$

2.4 Internal Combustion Engine

To model the internal combustion engine quasi-statically, the inputs are the torque T_{ICE} , the rotational speed ω_{ICE} , and the acceleration $\dot{\omega}_{ICE}$. The torque, that internally needs to be provided by the piston, is calculated by adding the torque that is required to overcome the engines inertia to the torque that is requested from the engine. The parameter Θ_{ICE} is the rotational inertia of the engine. The internal torque is given by

$$T_{ICE,i} = T_{ICE} + \Theta_{ICE}\dot{\omega}_{ICE}, \quad (2.11)$$

where the requested engine torque can be expressed by the split factor as

$$T_{ICE} = (1 - u) \cdot T_{GB}. \quad (2.12)$$

The (internal) engine torque is limited by the engines maximum torque line, namely

$$T_{ICE,i} \in [0, T_{ICE,max}(\omega_{ICE})]. \quad (2.13)$$

The corresponding fuel mass flow \dot{m}_f^* is evaluated from a stationary consumption map

$$\dot{m}_f^* = \begin{cases} f_{ICE}(T_{ICE,i}, \omega_{GB}), & \text{if } u < 1 \\ 0, & \text{if } u = 1. \end{cases} \quad (2.14)$$

This formulation assumes that the engine is shut off if no torque is required, i.e., the clutch is then disengaged and the injection is stopped.

The corresponding efficiency map of the engine motor with the maximum torque line is shown in Fig. 2.3.

The engine's rotational speed is limited to

$$\omega_{ICE} \in [\omega_{ICE, idle}, \omega_{ICE, max}] \quad (2.15)$$

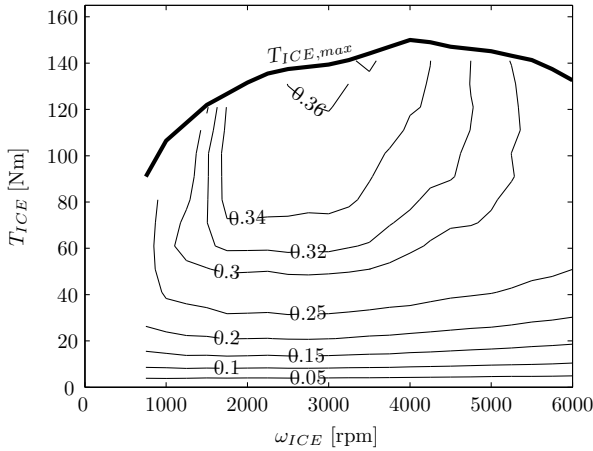


Figure 2.3: Engine map with iso-efficiency and peak torque lines.

2.5 Electric Motor

Similarly to the internal combustion engine, the electric motor is also modeled with a quasi-static map of the electric power P_{EM} as a function of the requested torque T_{EM} and speed ω_{GB} . The torque is again superposed with the torque due to inertia. Hence, the following equations describe the electric motor.

$$T_{EM,i} = T_{EM} + \Theta_{EM} \dot{\omega}_{EM} \quad (2.16)$$

$$T_{EM} = u \cdot T_{GB} \quad (2.17)$$

$$P_{EM} = f_{EM}(T_{EM,i}, \omega_{GB}) \quad (2.18)$$

$$T_{EM,i} \in [T_{EM,min}(\omega_{EM}), T_{EM,max}(\omega_{EM})] \quad (2.19)$$

$$\omega_{EM} \in [0, \omega_{EM,max}] \quad (2.20)$$

The parameter Θ_{EM} is the rotational inertia of the electric motor.

The corresponding efficiency map of the electric motor with the maximum and minimum torque lines is shown in Fig. 2.4. The efficiency in this figure is expressed for the motor and the generator separately such that it is less than one.

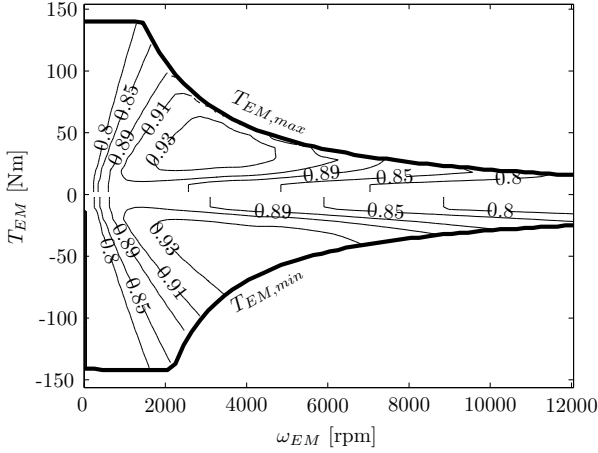


Figure 2.4: Motor map with iso-efficiency and peak torque lines.

2.6 Battery

The battery is modeled by a Thévenin equivalent circuit model. Such a model neglects the dynamics of the electrochemistry. However, these dynamics are relatively fast and can be neglected for a model dedicated to energetic considerations. The equivalent circuit is represented in Fig. 2.5, where $V_{oc}(\xi)$ is the open-circuit voltage of the battery depending on the state-of-charge ξ . The variable $R_i(\xi, \text{sign}(I_{BT}))$ is the inner resistance as a function of the state-of-charge, but also of the direction of the current I_{BT} . This simple model allows to express the terminal voltage of the battery as

$$V_{BT}(\xi, I_{BT}) = V_{oc}(\xi) - R_i(\xi, \text{sign}(I_{BT})) \cdot I_{BT}, \quad (2.21)$$

where a discharging current is defined to be positive in accordance with the literature, as for example in [8].

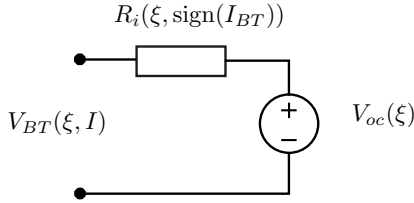


Figure 2.5: Equivalent circuit model for the battery.

The battery power results then as

$$P_{BT} = V_{BT}(\cdot) \cdot I_{BT}(\cdot) = V_{oc}(\cdot) \cdot I_{BT}(\cdot) - R_i(\cdot) \cdot I_{BT}^2(\cdot). \quad (2.22)$$

In order to formulate the battery model corresponding to the backward-approach, the above equation is solved for the battery current as a function of the power that is drawn/supplied from/to the battery. This yields

$$I_{BT}(\xi, \text{sign}(P_{BT})) = \frac{V_{oc}(\xi) - \sqrt{V_{oc}^2(\xi) - 4R_i(\xi, \text{sign}(I_{BT})) \cdot P_{BT}}}{2R_i(\xi, I_{BT})}. \quad (2.23)$$

The state-of-charge of the battery is the only state variable of this model and results from current integration

$$\frac{d\xi}{dt} = -\frac{I_{BT}}{Q_0}, \quad (2.24)$$

with an initial condition $\xi(t = 0) = \xi_0$. The parameter Q_0 is the nominal battery capacity. The state-of-charge of the battery is physically limited to $[0, 1]$. In order to prevent the battery from excessive wear, operation of the battery is only allowed in some limited range

$$\xi \in [\xi_{\min}, \xi_{\max}], \quad (2.25)$$

given by hard constraints that lie within the physical SoC limits. These hard constraints are defined by the manufacturer of the battery pack. In this thesis, the state constraints are set to $\xi_{\min} = 0.4$ and $\xi_{\max} = 0.7$ in accordance with [16].

The battery used in this thesis is a nickel-metal hydride battery (NiMH). Its open-circuit voltage $V_{oc}(\xi)$ is shown in Fig. 2.6, its inner resistance is kept constant due to the lack of better data. Its value is given in Table 2.1. Since measurements were performed on a lithium-ion battery (Li-ion) at a later stage, the Li-ion battery with the measured data is used in Sec. 4.3.2.

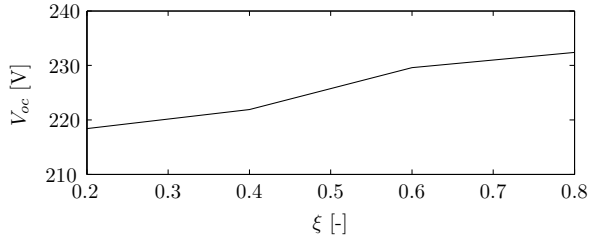


Figure 2.6: Open-circuit voltage of the NiMH battery.

2.7 Auxiliary Systems

The power demand of the auxiliary systems are summarized in an electric power demand P_{aux} . For the sake of simplicity this value is kept constant throughout this thesis.

Table 2.1: Parameters for the powertrain.

Parameter	Value	Unit
m_v	1578	[kg]
A_f	2.51	[m ²]
c_d	0.3167	[-]
$c_{r,0}$	$9 \cdot 10^{-3}$	[-]
$c_{r,1}$	$8.53 \cdot 10^{-5}$	[s/m]
r_{WH}	0.308	[m]
Θ_{WH}	3.8925	[kg m ²]
$T_{WH,loss}$	7.912	[Nm]
ν_{GB}	[17.4812, 9.8806, 6.4858, ... 4.9657, 3.9523, 3.3949]	[-]
η_{GB}	0.9	[-]
Θ_{ICE}	0.079	[kg m ²]
$\omega_{ICE,idle}$	89	[rad/s]
$\omega_{ICE,max}$	655	[rad/s]
Θ_{EM}	0.0289	[kg m ²]
$\omega_{EM,max}$	1262	[rad/s]
R_i	0.273	[Ω]
Q_0	22320	[C]
P_{aux}	350	[W]

Chapter 3

Dynamic Programming

This chapter gives a brief overview of the deterministic dynamic programming algorithm, which throughout this thesis is referred to as dynamic programming (DP). This algorithm relies on the principle of optimality that was introduced by Bellman [13]. In this chapter, the algorithm is introduced with a focus on its application, the interested reader is referred to [14] for more details.

Since DP requires evaluation of the entire discretized state/time-space, it is computationally expensive. However, it allows to find the global optimal control signal if the disturbance is completely known. This global optimum is very valuable to quantify the performance of suboptimal, causal control strategies on an objective basis. Further, the results can be used to get insight into the structure of the optimal solution and help to understand the problem.

Since the algorithm relies on the discretized state-space, some numerical problems appear that lead to some deviations of the achieved final state from the targeted final state. During this work, a method was developed to improve the numerics of the algorithm. This finally increases the precision of the final state considerably. Further, this method allows for reduction of the computational cost considerably. The method is so far only applicable to problems with a scalar state and is published in [20, 21]. In Chapter 6, the method is applied with a second state variable which is only a binary variable. The extension for this special case is explained in more details in [22].

The method to improve the numerics is investigated on the example of the optimal fishing problem in a Lotka-Volterra population. This standard optimal control problem can be solved analytically for the continuous-time problem and allows therefore for a complete evaluation of the method.

3.1 Problem Formulation

The goal of this project is to find an optimal control that minimizes the fuel consumption of a full parallel hybrid electric vehicle. In order to be able to use typical optimization tools, such as dynamic programming or Pontryagin's minimum principle, the problem must be formulated mathematically in a suitable form, first.

A non-mathematical formulation of the current problem would be: Find the optimal control signal, that actuates the hybrid vehicle such that its integral fuel consumption over a given driving cycle is minimized. This control signal must further assure that the state-of-charge of the battery remains within well defined bounds. It must also take into account that the torque provided by the electric motor, as well as the engine torque, are limited. At the beginning of the driving cycle, the battery is at some initial state-of-charge. Obviously, the fuel optimal solution would be to deplete the battery over the driving cycle since the electric energy can be used to replace fuel energy. To avoid such charge depleting solutions, a condition on the final state-of-charge must be defined. In this thesis, we define a target set for the final state.

A general mathematical formulation of such an optimal control problem with fixed final time t_f is

$$\min_{u(t)} J(u(t)) \quad (3.1a)$$

s.t.

$$\dot{x}(t) = F(x(t), u(t), t) \quad (3.1b)$$

$$x(0) = x_0 \quad (3.1c)$$

$$x(t_f) \in [x_{f,min}, x_{f,max}] \quad (3.1d)$$

$$x(t) \in \mathcal{X}(t) \quad (3.1e)$$

$$u(t) \in \mathcal{U}(t), \quad (3.1f)$$

where

$$J(u(t)) = G(x(t_f)) + \int_0^{t_f} H(x(t), u(t), t) dt \quad (3.1g)$$

is the cost functional.

The energy management problem for the parallel hybrid electric vehicle

can be formulated as an optimal control problem as follows:

$$\min_{u(t)} J(u(t)) \quad (3.2a)$$

s.t.

$$\dot{\xi}(t) = -\frac{I_{BT}(\xi(t), u(t), t)}{Q_0} \quad (3.2b)$$

$$\xi(0) = \xi_0 \quad (3.2c)$$

$$\xi(t_f) \in [\xi_{f,min}, \xi_{f,max}] \quad (3.2d)$$

$$\xi(t) \in [\xi_{min}, \xi_{max}] \quad (3.2e)$$

$$u(t) \in [u_{min}(t), u_{max}(t)], \quad (3.2f)$$

where

$$J(u(t)) = \int_0^{t_f} H_l \cdot \dot{m}_f^*(u(t), t) dt \quad (3.2g)$$

is the cost functional. This cost integrates the fuel mass flow $\dot{m}_f^*(u(t), t)$ multiplied with the (constant) lower heating value H_l over the driving cycle. Hence, this formulation minimizes the fuel energy consumption which is equivalent to minimizing the fuel mass consumption.

The only state variable is the state-of-charge of the battery. Its dynamics are given by (2.24). Together with the expressions of the current (2.23) and the motor characteristics (2.17), the rate of change of the battery (3.2b) is expressed as a function of the control u , the state ξ , and the time. The time variance of the model results because the disturbance defined by the driving cycle $w_{GB}(t)$, $T_{GB}(t)$ is included in the model instead of a disturbance input.

The problem formulated above by (3.2) is a typical optimal control problem. Its following properties are worth to note:

- *Nonlinearity*: The state dynamics (3.2b) as well as the cost functional (3.2g) are nonlinear. The system could be linearized around some operating points. However, this would not yield useful results because important characteristics of the system would be lost. The most prominent characteristic is the discontinuity of the engine's fuel consumption between on and off condition.
- *State constraints*: The constraints on the state-of-charge are time-invariant.

- *Input constraints:* The input constraints are directly given by limitations of the electric motor. Further, there are indirect limitations given by the engine limitations and the torque balance. The input constraints are time-variant, here.
- *Time variance:* The problem is defined over a driving cycle. Hence, the rotational speed and the torque that are requested from the powertrain vary with time. As a consequence, the problem is time-variant.

3.2 Basic DP Algorithm

Since dynamic programming is a numerical algorithm used here to solve a continuous optimal control problem, the continuous-time model (3.1b) must be discretized in time. Let the discrete-time model be given by

$$x_{k+1} = F_k(x_k, u_k), \quad k = 0, 1, \dots, N - 1 \quad (3.3)$$

with the state variable $x_k \in \mathcal{X}_k$ and the control signal $u_k \in \mathcal{U}_k$. Furthermore, assume that the disturbance is perfectly known in advance and at every time instance k . This disturbance signal is included in the state update function (3.3) in the formulation here. Hence, the update function is a function of the time step, what is indicated with the function's index k .

Let $\pi = \{\mu_0, \mu_1, \dots, \mu_{N-1}\}$ be a control policy. Further let the discretized cost of (3.1g) using π with the initial state $x(0) = x_0$ be

$$\begin{aligned} J_\pi(x_0) = & g_N(x_N) + \phi_N(x_N) \dots \\ & + \sum_{k=0}^{N-1} h_k(x_k, \mu_k(x_k)) + \phi_k(x_k), \end{aligned} \quad (3.4)$$

where $g_N(x_N) + \phi_N(x_N)$ is the final cost. The first term $g_N(x_N)$ corresponds to the final cost in (3.1g). The second term is the additional penalty function $\phi_N(x_N)$ forcing a partially constrained final state (3.1d). The function $h_k(x_k, \mu_k(x_k))$ is the cost of applying $\mu_k(x_k)$ at x_k , according to $H(x(t), u(t), t)$ in (3.1g). The state constraints (3.1e) are enforced by the penalty function $\phi_k(x_k)$ for $k = 0, 1, \dots, N - 1$.

The optimal control policy π^o is the policy that minimizes J_π

$$J^o(x_0) = \min_{\pi \in \Pi} J_\pi(x_0), \quad (3.5)$$

where Π is the set of all admissible policies.

Based on the principle of optimality [13], dynamic programming is the algorithm, which evaluates the optimal cost-to-go¹ function $\mathcal{J}_k(x^i)$ at every node in the discretized state-time space² by proceeding backward in time:

1. End cost calculation step

$$\mathcal{J}_N(x^i) = g_N(x^i) + \phi_N(x^i) \quad (3.6a)$$

2. Intermediate calculation step for $k = N - 1$ to 0

$$\mathcal{J}_k(x^i) = \min_{u_k \in \mathcal{U}_k} \{h_k(x^i, u_k) + \phi_k(x^i) + \mathcal{J}_{k+1}(F_k(x^i, u_k))\} \quad (3.6b)$$

The optimal control is given by the argument that minimizes the right-hand side of equation (3.6b) for each x^i at time index k of the discretized state-time space.

The cost-to-go function $\mathcal{J}_{k+1}(x)$ used in (3.6b) is evaluated only on discretized points in the state space. Furthermore, the output of the model function $F_k(x^i, u_k)$ is a continuous variable in the state space which can be between the nodes of the state grid. Consequently, the last term in (3.6b), namely $\mathcal{J}_{k+1}(F_k(x^i, u_k))$ must be evaluated appropriately. There exist several methods of finding the appropriate cost-to-go $\mathcal{J}_{k+1}(F_k(x^i, u_k))$ such as using a nearest-neighbor approximation or using an interpolation scheme. Throughout this thesis, linear interpolation of the cost-to-go \mathcal{J}_{k+1} is used to account for the problem of the discretized state space.

The output of the algorithm (3.6) is an optimal control signal map. This map is used to find the optimal control signal during a forward simulation of the model (3.3), starting from a given initial state x_0 , to generate the optimal state trajectory. In the map the control signal is only given for the discrete points in the state space grid. The control signal is therefore interpolated when the actual state does not coincide with the points in the state grid.

¹The terms *cost-to-go* and *optimal cost-to-go* are used equivalently throughout this chapter referring to *optimal cost-to-go*. It is important to note that the term *optimal* is used in the sense of optimality achievable under the numerical errors.

²The following notation is used: x_k^i denotes the state variable x in the discretized state-time space at the node with time-index k and state-index i . x_k denotes a (state-) continuous state-variable at time k .

3.3 Numerical Issues

When implementing the algorithm numerical errors must be considered and minimized. One issue to consider is the definition of the cost function for infeasible states and inputs. Infeasible states and inputs are of course infinitely expensive and should therefore have infinite cost $\phi_k(x^i \notin \mathcal{X}_k) \rightarrow \infty$ for $k = 1, \dots, N$ since the defined objectives (such as final state constraints and model limitations) cannot be achieved. When using infinite cost for such states, some substantial numerical errors occur due to the discretization of time and state space.

Define the set of reachable states Ω_k^i over one time-step by using all admissible inputs and starting at a given state x^i at time k

$$\Omega_k^i = \{x | x = F_k(x^i, u) \forall u \in \mathcal{U}_k\}. \quad (3.7)$$

Consider the grid point/time step domain in Fig. 3.1 (bottom graph) and that the DP algorithm is calculating the cost-to-go for the state x^i at time $k+1$. If an infinite cost is used for infeasible states and linear interpolation is used the feasible part of Ω_{k+1}^i would use an interpolation between an infinite cost-to-go $\mathcal{J}_{k+2}(x^i)$ and a finite cost-to-go $\mathcal{J}_{k+2}(x^{i+1})$. As a result, the cost-to-go for x^i at time $k+1$ becomes infinite, i.e., $\mathcal{J}_{k+1}(x^i) \rightarrow \infty$, although the grid point $\{k+1, i\}$ is perfectly within the feasible domain.

Now consider the algorithm at time k and the step of calculating the cost-to-go for the state x^i . The cost-to-go $\mathcal{J}_k(x^i)$ will, for the same reason as for the time $k+1$, be infinite since $\mathcal{J}_{k+1}(x^i)$ was calculated before to be infinite. When these effects continue and the algorithm proceeds backwards in time, the calculated infeasible region will grow into the actual feasible region.

A first step to tackle this problem is to use a big, but finite value for the cost instead of infinity $\phi_k(x^i \notin \mathcal{X}_k) = \mathcal{J}_\infty$ for $k = 1, \dots, N$. This big finite value \mathcal{J}_∞ must be bigger than the maximum value of the cost-to-go function $\mathcal{J}_k(x^i)$. Using a finite cost value for infeasible domains improves the solution, but the effect shown above for infinity cannot be completely eliminated close to the boundary line. Throughout this chapter the method of using a finite cost value \mathcal{J}_∞ for infeasible domains together with the algorithm in Sec. 3.2 is referred to as *basic DP*.

Due to the interpolation between feasible and infeasible states, the infinite gradient at the boundary line is being blurred. This is shown in

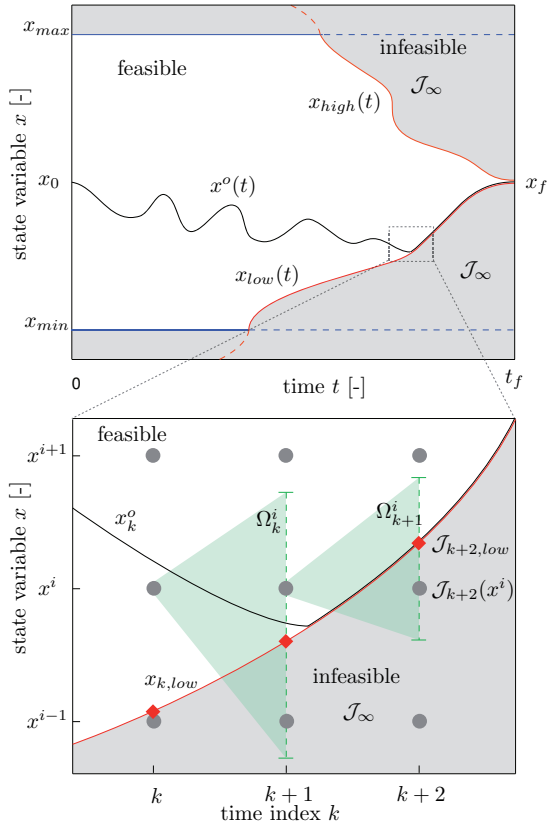


Figure 3.1: Schematic overview of an optimal control problem solved using the dynamic programming algorithm. The figure shows the state variable boundaries for the dynamic programming algorithm for the entire problem domain (top) and in the grid point/time step domain (bottom).

Fig. 3.2 for the fishing problem (introduced later), where the dashed line is the cost-to-go computed by DP with a finite cost for infeasible states, i.e., the basic DP method. The solid line corresponds to the cost-to-go from DP improved by the new method introduced in this work. As a result of the blurred cost-to-go function, the optimal state trajectory cannot approach the boundary line since the computed cost-to-go near the boundary line

is too high. Figure 3.3 shows the corresponding state trajectory (dashed) being deviated by this effect. The solid line is the state trajectory from DP improved by the new method.

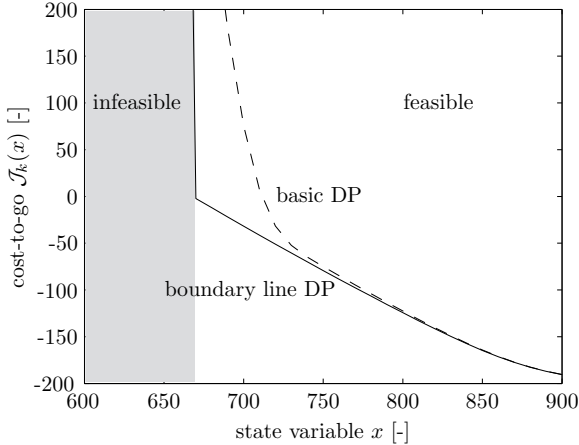


Figure 3.2: Section of the cost-to-go function $\mathcal{J}_k(x)$ at time index k such that $t = 180$ h for the fishing problem. State space discretization is $\Delta x = 10$, penalty for infeasible states is set to $\mathcal{J}_\infty = 1200$.

3.4 Boundary Line Method

The method presented in this section tackles the problem of a blurred gradient at the boundary line due to interpolation of the cost-to-go between a feasible and an infeasible state-grid point. Therefore, the boundary line between feasible and infeasible regions must be found. This is shown in the first part of this section. The second part shows a simple, yet powerful, method to improve the DP by accounting for this boundary line. This improved DP is referred to as *boundary line DP*.

Throughout this section, equation (3.3) is reformulated as

$$x_{k+1} = f_k(x_k, u_k) + x_k, \quad k = 0, 1, \dots, N - 1 \quad (3.8)$$

where

$$f_k(x_k, u_k) = F_k(x_k, u_k) - x_k. \quad (3.9)$$

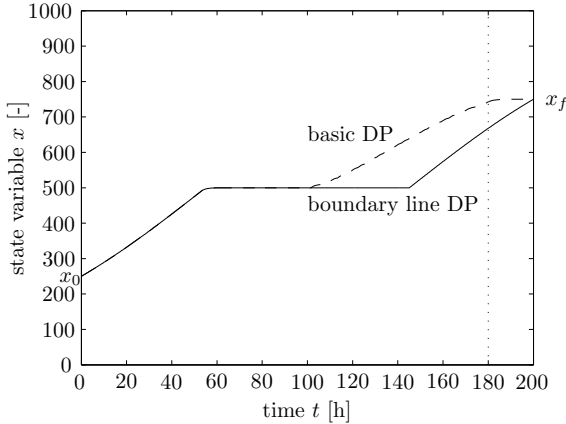


Figure 3.3: State trajectories from DP for the fishing problem. The solid line shows the result based on the boundary line method. The dashed line is the state trajectory resulting from the basic DP. The dotted vertical line at $t = 180$ h indicates the time where Fig. 3.2 is evaluated. State space discretization is $\Delta x = 10$, penalty for infeasible states is set to $\mathcal{J}_\infty = 1200$.

3.4.1 Computation of the Boundary Line

There exist infeasible regions in the state-time space of an optimization problem with fixed final time and a partially constrained final state if the state dynamics are bounded. Since the dynamic system is assumed to be one-dimensional, there exist only two infeasible regions, namely an upper and a lower region. This is depicted in Fig. 3.1. In this section, the lower boundary line between feasible and infeasible region is derived. The upper boundary line is found in analogy.

The partially constrained final state is given by (3.1d). The lower boundary line is defined as the lowest state $x_{k,low}$ at each time instance k that allows to achieve the minimal final state $x_{f,min}$. Note that the lower boundary line is only discretized in time, i.e., it is continuous in the state variable. The lower boundary line can be evaluated by sequentially going backward in time from $k = N - 1$ back to $k = 0$ and solving the following

optimization problem at each time instance k :

$$\min_{x_{k,low}, u_k} x_{k,low} \quad (3.10a)$$

s.t.

$$f_k(x_{k,low}, u_k) + x_{k,low} = x_{k+1,low} \quad (3.10b)$$

$$u_k \in \mathcal{U}_k \quad (3.10c)$$

$$x_{k,low} \in \mathcal{X}_k. \quad (3.10d)$$

The problem is initialized with $x_{N,low} = x_{f,min}$. At each time-step, u_k and $x_{k,low}$ are the only unknowns, $x_{k+1,low}$ is a parameter at time k . By solving (3.10b) for $x_{k,low}$ and inserting it in (3.10a) the following, more direct problem is obtained:

$$\max_{x_{k,low}, u_k} f_k(x_{k,low}, u_k) \quad (3.11a)$$

s.t.

$$f_k(x_{k,low}, u_k) + x_{k,low} = x_{k+1,low} \quad (3.11b)$$

$$u_k \in \mathcal{U}_k \quad (3.11c)$$

$$x_{k,low} \in \mathcal{X}_k. \quad (3.11d)$$

If the state is assumed to be unconstrained, i.e., (3.11d) is omitted, the following formulation is equivalent:

$$x_{k,low} = x_{k+1,low} - \max_{u_k \in \mathcal{U}_k} f_k(x_{k,low}, u_k) \quad (3.12)$$

Equation (3.12) is a fixed point problem ($x = f(x)$), where $x_{k,low}$ is the unknown.

The lower boundary line is finally found by the following algorithm:

1. Initialize with the lower bound of the partially constrained final state

$$x_{k,low} = x_{f,min}.$$
2. Proceed backward in time for $k = N - 1, \dots, 0$
 - (a) Solve the fixed point problem (3.12) without state constraints as shown below in (3.13).
 - (b) Check whether the solution found respects the state constraints.
 - (c) If the constraints are not respected, solve the general problem (3.11).

- (d) Store the solution $x_{k,low}$ with the respective minimizer $u_{k,low}$ and the cost-to-go $\mathcal{J}_{k,low}$.

The fixed point problem (3.12) of time step k without state constraints can be solved with the following algorithm³:

1. Initialization:

$$x_{k,low}^{j=0} = x_{k+1,low} \quad (3.13a)$$

2. Iteration over j until a specified tolerance is achieved:

$$x_{k,low}^{j+1} = x_{k+1,low} - \max_{u_k \in \mathcal{U}_k} \{f_k(x_{k,low}^j, u_k)\} \quad (3.13b)$$

This algorithm converges if

$$\left| \frac{\partial}{\partial x_{k,low}^j} \max_{u_k \in \mathcal{U}_k} \{f_k(x_{k,low}^j, u_k)\} \right| < 1. \quad (3.13c)$$

Note that the algorithm mentioned above (3.13) finds the limit value $x_{k,low}$ in the first iteration if the update function f_k is independent of the state variable x_k .

3.4.2 Interpolation Near the Boundary Line

It is assumed that the state boundary lines $x_{k,low}$ (and $x_{k,high}$) shown in Fig. 3.1 with their corresponding cost-to-go $\mathcal{J}_{k,low}$ (and $\mathcal{J}_{k,high}$) along the boundary line have been calculated prior to the DP algorithm. Therefore, when the set Ω_k^i contains the boundary it is possible to interpolate between the exact boundary and a feasible state grid point as illustrated in Fig. 3.4 with the solid and the dashed lines. The dotted line illustrates the interpolation by the basic algorithm at the boundary between feasible and infeasible regions.

Consider the DP algorithm to evaluate the cost-to-go for the state-grid point x^i at time $k + 1$ (see Fig. 3.1, bottom graph). Starting from state x^i , the state achieved at the end of this time-step

$$x_{k+2} = f_{k+1}(x^i, u_{k+1}) + x^i \in \Omega_{k+1}^i \quad (3.14)$$

³The index j placed on the top right of x is the iteration index, here. It is not the index of the state-grid as used in the rest of this chapter.

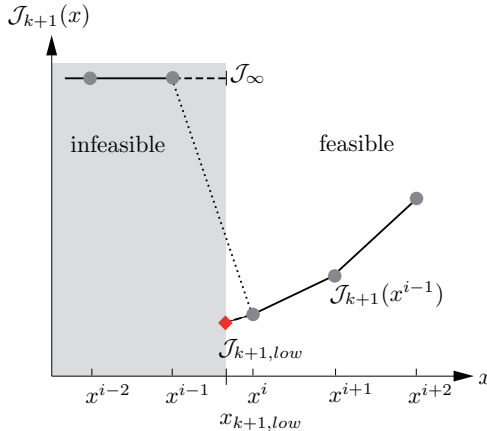


Figure 3.4: Interpolation of $\mathcal{J}_{k+1}(x)$ near the boundary line. The dashed lines illustrate the (linearly) interpolated values including the boundary line. The dotted line illustrates the interpolation used by the basic algorithm.

can reach the feasible as well as the infeasible region. The corresponding cost-to-go $\mathcal{J}_{k+2}(x_{k+2})$ is evaluated by interpolation between $\mathcal{J}_{k+2}(x^{i+1})$ and $\mathcal{J}_{k+2,low}$ if the state x_{k+2} is above or on the boundary line $x_{k+2,low}$. Otherwise, the cost-to-go is set infinite or to the big, finite value \mathcal{J}_{∞} . This procedure allows to maintain the same accuracy close to the boundary line as achieved within the feasible domain.

Application of the optimal control signal map in the forward simulation which is mentioned in Sec. 3.2 is improved by the boundary line in analogy. Since the control signal on the boundary line was evaluated before, interpolation of the control signal is carried out between the grid points of the feasible domain or between the feasible domain and the boundary line.

3.5 Example: Optimal Fishing

This section studies a well-known optimal control problem namely the optimal fishing in a Lotka-Volterra fish population. The fishing problem is chosen because it has an analytic solution.

3.5.1 Continuous-Time Problem

The continuous-time dynamic Lotka-Volterra system is

$$\dot{x}(t) = \frac{2}{100} \cdot \left(x(t) - \frac{x^2(t)}{1000} \right) - u(t), \quad (3.15)$$

where the state variable $x(t)$ is the amount of fish in a lake, the control signal $u(t)$ is the fishing rate. The control signal $u(t)$ is limited to $u(t) \in [0, 10]$. For the considered system the state $x(t)$ is limited to $x(t) \in [0, 1000]$ since

$$\lim_{\substack{t \rightarrow \infty \\ u(t)=0}} x(t) = 1000. \quad (3.16)$$

The objective is to maximize the amount of fish caught, which is equivalent to minimize

$$J = \int_0^{t_f} -u(t) dt \quad (3.17)$$

within a fixed time t_f while the minimal amount of fish in the population at the final time must be $x_{f,min} = 750$. This can be stated as the optimal control problem

$$\min_{u(t)} \int_{t=0}^{t_f} -u(t) dt \quad (3.18a)$$

s.t.

$$\dot{x}(t) = \frac{2}{100} \cdot \left(x(t) - \frac{x^2(t)}{1000} \right) - u(t) \quad (3.18b)$$

$$x(0) = 250 \quad (3.18c)$$

$$x(t_f) \geq 750 \quad (3.18d)$$

$$x(t) \in [0, 1000] \quad (3.18e)$$

$$u(t) \in [0, 10] \quad (3.18f)$$

$$t_f = 200. \quad (3.18g)$$

The solution to the above optimal control problem is straightforward to determine and has the form

$$u^o(t) = \begin{cases} 0 & \text{if } t \in [0, t_a] \\ 5 & \text{if } t \in (t_a, t_f - t_b) \\ 0 & \text{if } t \in [t_f - t_b, t_f] \end{cases} \quad (3.19a)$$

where

$$t_a = t_b = 100 \cdot \operatorname{artanh} \left(\frac{1}{2} \right). \quad (3.19b)$$

The final maximum amount of fish caught is

$$\begin{aligned} J_{analytic}^o &= -5 \cdot (t_f - t_a - t_b) \\ &= -1000 \cdot \left(1 - \operatorname{artanh} \left(\frac{1}{2} \right) \right) \\ &\approx -450.694 \end{aligned} \quad (3.20)$$

3.5.2 Discrete-Time Problem

In order to evaluate the optimal solution by means of dynamic programming, the continuous-time state dynamics (3.15) must be discretized. Using an Euler forward approximation with a time step $t_s = 0.2$ h, the discrete-time model is

$$x_{k+1} = f(x_k, u_k) + x_k, \quad k = 0, 1, \dots, N - 1 \quad (3.21a)$$

where

$$f(x_k, u_k) = t_s \cdot \left(\frac{2}{100} \cdot \left(x_k - \frac{x_k^2}{1000} \right) - u_k \right). \quad (3.21b)$$

The state x_k is the amount of fish in a lake, the control signal u_k is the constant fishing rate during one time step. The discrete-time optimal control problem is:

$$\min_{u_k \in [0, 10]} \sum_{k=0}^{N-1} -u_k \cdot t_s \quad (3.21c)$$

s.t.

$$x_{k+1} = f(x_k, u_k) + x_k \quad (3.21d)$$

$$x_0 = 250 \quad (3.21e)$$

$$x_N \geq 750 \quad (= x_{f,min}) \quad (3.21f)$$

$$x_k \in [0, 1000] \quad (3.21g)$$

$$N = \frac{200}{t_s} + 1. \quad (3.21h)$$

As mentioned in Sec. 3.3, use of a big, but finite value \mathcal{J}_∞ to penalize infeasible states improves numerics. This value should be chosen as small

as possible but larger than any value of the (feasible) cost-to-go that could occur. Since this simple example allows for analytic solutions the maximum cost-to-go of the continuous-time problem is evaluated in order to choose a suitable value for \mathcal{J}_∞ . The minimum cost-to-go $\mathcal{J}_t(x)$ is obviously at $t = 0$ and $x = 1000$ and yields:

$$\begin{aligned}\mathcal{J}_{t=0}(x = 1000) &= 500 \operatorname{artanh}\left(\frac{1}{2}\right) - 1000 - 125\pi \\ &\approx -1118.\end{aligned}\tag{3.22}$$

For the fishing problem, at $t = 0$, the minimum cost-to-go (3.22) is approximately 1118 less than the cost-to-go at $t = t_f = 200$

$$\mathcal{J}_{t=200}(x \in \mathcal{X}_{t=200}) = 0.\tag{3.23}$$

The penalty of the infeasible states at t_f must therefore be penalized by value larger than 1118 to ensure that the final state constraint is met.

Consequently, the penalty \mathcal{J}_∞ used for the cost-to-go of infeasible states is set to a value greater than $\mathcal{J}_\infty > 1118$. For the example here a value of

$$\mathcal{J}_\infty = 1200\tag{3.24}$$

is chosen and is used in the DP-algorithm.

The output of the dynamic programming algorithm is an optimal control signal map, specifying the optimal control signal at each time step k and each state $x_k \in \mathcal{X}_k$. The optimal control signal map for the Lotka-Volterra system is shown in Fig. 3.5. It shows that the optimal control is ‘not fishing’ ($u = 0$) if the fish population is small ($x < 500$), ‘moderate fishing’ ($u = 5$) if the population is $x = 500$ and ‘full fishing’ ($u = 10$) if the population is large ($x > 500$). Toward the end of the problem, one must stop fishing as late as possible, such that the population reaches the specified minimum final size of $x_{f,min} = 750$. The resulting optimal state trajectory, i.e., the fish population for an initial state of $x_0 = 250$ is shown as the black solid line. The solution of the dynamic programming clearly reflects the optimal control found for the continuous problem (3.19a).

3.5.3 Resolution Study

The accuracy of the solution obtained with dynamic programming can degrade due to numeric issues as mentioned earlier. The state space must

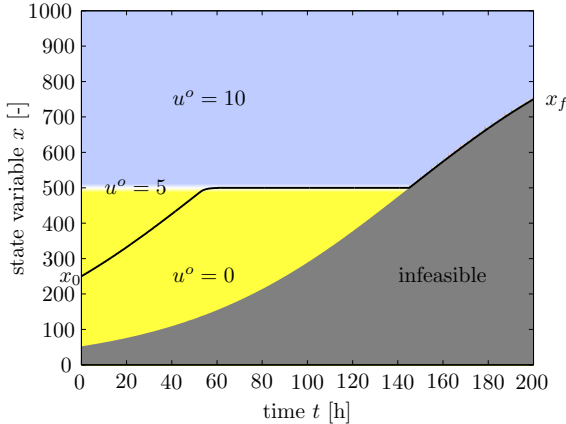


Figure 3.5: The optimal control signal map, determined using dynamic programming, for the discrete-time Lotka-Volterra system. The optimal state trajectory for $x_0 = 250$ when using the map is shown as the solid black line.

be discretized for the DP-algorithm. The resolution of the state space discretization is a critical quantity. On one hand, the computational effort increases with higher resolution. On the other hand, accuracy of the solution improves with increasing resolution.

Therefore, a study is carried out here to quantify the accuracy of the solution obtained by DP for the simple example of the fishing problem. The fishing problem has been chosen because an analytic solution exists that can be used as a benchmark. The resolution study is carried out for the basic DP, but also for the new method presented in this chapter, i.e., the boundary line DP.

The quality of the solution is expressed as the relative difference between optimal cost obtained by DP and the analytic optimal solution, $\frac{J_{analytic}^o - J_{dp}^o}{J_{analytic}^o}$. Figure 3.6 shows this deviation of the optimal solution evaluated with DP (basic and boundary line) from the analytic optimal solution.

Since the analytic solution is evaluated for the original continuous-time problem, the discrete-time solution can never achieve the analytic optimal solution. This discretization error is indicated in Fig. 3.6 with the dotted line marked as ‘minimum time-discretization error’. It emphasizes that the solution using the boundary line DP converges well toward the discrete-

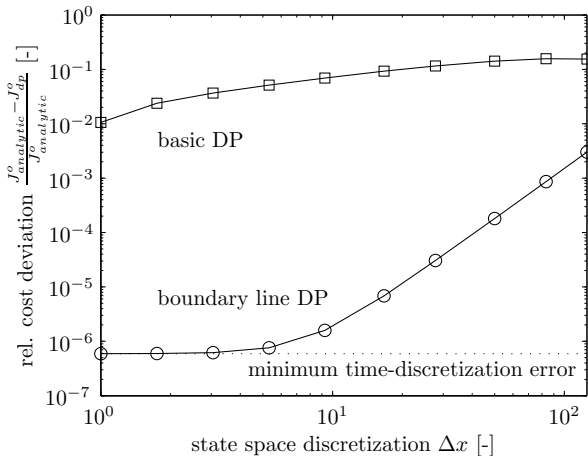


Figure 3.6: The relative deviation of the cost computed by dynamic programming compared to the optimal analytic solution for the fishing problem.

time optimum. Furthermore, this figure illustrates the importance of the boundary line: the numeric solution with the boundary line DP is closer to the analytic solution than with the basic DP for the same resolution by a factor of 50 to 68000. It is interesting to note that the cost (3.21c) resulting from boundary line DP is inferior to the cost resulting from basic DP over the entire range of resolution that was investigated, i.e., the solution using the boundary line DP at lowest resolution ($\Delta x = 125$) is closer to the analytic solution than the solution of the basic DP at highest resolution ($\Delta x = 1$).

The relative deviation of the final state achieved by the DP (basic and boundary line) from the optimal final state is shown in Fig. 3.7 for different resolutions. The optimal final state is the lowest admissible final state for this example, i.e., $x^o(t_f) = x_{f,min}$. The figure shows clearly that the final state deviation of the basic DP decreases with decreasing Δx , i.e., increasing resolution. Using the boundary line DP, the final state deviation is negligible over the entire range of resolutions investigated here.

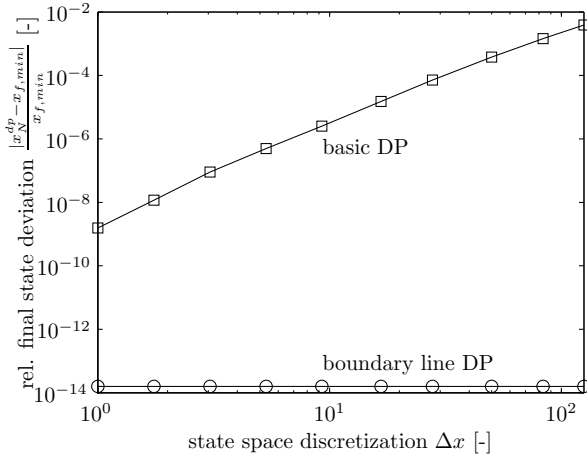


Figure 3.7: The relative deviation of the actual final state and the optimal final state for the fishing problem.

3.5.4 Computational Effort

The computational effort of an optimization method is often a crucial factor that determines whether a method is being applied in practice for a given problem or not. Therefore, not only the accuracy of a solution as shown in Sec. 3.5.3 is relevant, but also the corresponding computational cost.

The number of model-function evaluations for the basic DP with an equally spaced grid is given by:

$$N_{feval}^{DPbasic} = N_x \cdot N_u \cdot N. \quad (3.25)$$

This is only true for a single dimensional state space and a scalar control signal. N_x is the number of grid points for the state space, N_u for the control signal, and N for the time discretization.

When using the boundary line DP, the infeasible domain is well known. Consequently, computation for the grid points in this infeasible domain (see Fig. 3.1) can be omitted [23]. The number of infeasible grid points at a time-step k is denoted as $N_{k,x}^{infeas}$. Hence, the number of function

evaluations that can be saved are:

$$N_{feval}^{infeas} = N_u \cdot \sum_{k=0}^{N-1} N_{k,x}^{infeas}. \quad (3.26)$$

The cost to evaluate the boundary line cannot be neglected. The number of function evaluations needed to compute the line is denoted with N_{feval}^{line} .

Consequently, the number of function evaluations needed for solving the DP with the boundary line is given by:

$$N_{feval}^{DPline} = N_{feval}^{DPbasic} - N_{feval}^{infeas} + N_{feval}^{line}. \quad (3.27)$$

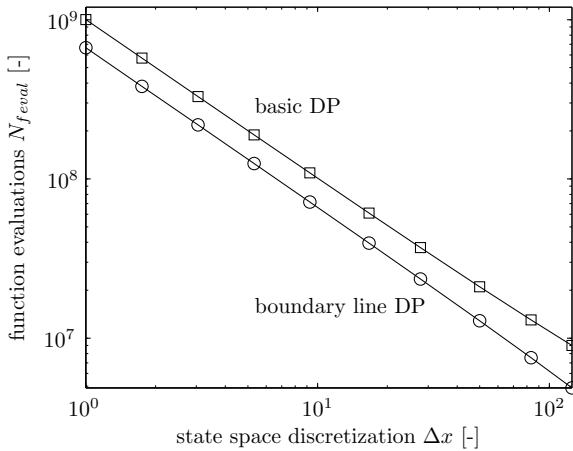


Figure 3.8: Number of function evaluations needed to find the solution of the fishing problem.

Figure 3.8 shows the number of function evaluations for the fishing problem over the discretization step Δx . It shows that more computations can be saved due to the infeasible domain than what is needed to evaluate the boundary line. The boundary line DP requires less function evaluations by a factor of 1.5 to 1.85 than the basic DP over the entire range of discretization steps investigated here. Further it should be recalled that the accuracy of the solution is considerably higher, even if the computational burden is lower.

More interesting is a comparison of solutions of similar accuracy. Therefore, the solution using the basic DP at lowest discretization step $\Delta x = 1$ is

Table 3.1: Comparison at similar accuracy for the fishing problem.

		basic DP	boundary line DP
state space discretization [-]	Δx	1	125
amount of fish caught [-]	$-J$	445.936	449.340
function evaluations [-]	N_{feval}	1002001000	4877143

compared to the solution of the boundary line DP at highest discretization step $\Delta x = 125$. The values are shown in Table 3.1. These results reveal that the boundary line DP is computationally a factor of $\frac{1002001000}{4877143} \approx 205$ more efficient than the basic DP although the accuracy of the solution is still better ($449.340 > 445.936$). This result motivates to apply the method to more complex systems.

3.6 Application on the Hybrid Vehicle

The optimal control problem of the energy management for the parallel hybrid electric vehicle as formulated by (3.2) is solved using dynamic programming for the NEDC with the same algorithm as applied to the optimal fishing problem. The initial condition is $\xi_0 = 0.55$, the final target set is $\xi_{f,min} = 0.55$ and $\xi_{f,max} = 0.7$, and the state constraints are $\xi_{min} = 0.4$ and $\xi_{max} = 0.7$. In Fig. 3.9 the resulting optimal torque split is shown at each state-of-charge over the duration of the driving cycle for the hybrid vehicle. Similarly to the fishing problem, the optimal state-of-charge trajectory is close to the boundary of the feasible state region at the end of the problem.

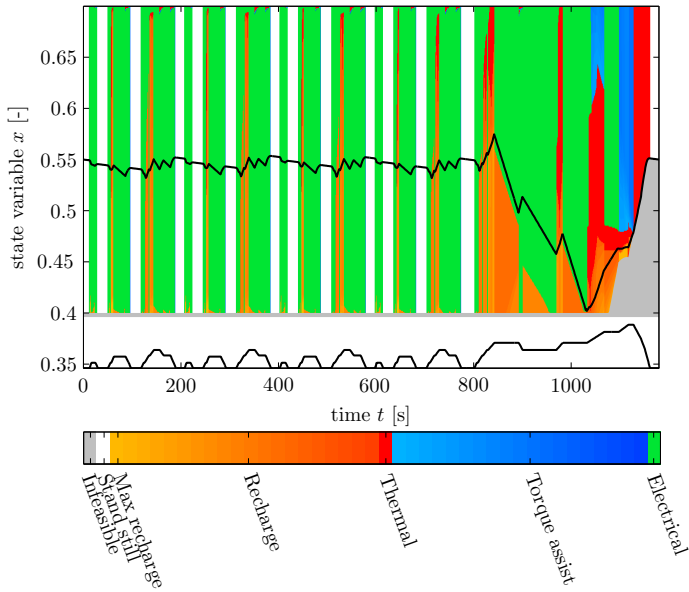


Figure 3.9: Output of the dynamic programming algorithm. The optimal input map for a full HEV driving the NEDC and the state-of-charge trajectory (black) when using the optimal control signal map.

3.7 Conclusions

The deterministic dynamic programming algorithm is briefly introduced and numerical issues with final state constraints are pointed out. A method is presented to handle these numerical issues appropriately. This method is referred to as boundary line method and it is evaluated on an example where analytical solutions exist. This investigation shows clearly that the accuracy of the final state has been increased considerably, even at relatively low state-space resolution.

In addition, this method proves to be computationally very efficient, since the resolution of the state-space could have been decreased considerably while maintaining the same accuracy as with the basic DP algorithm. Further, computation of the grid points lying within the infeasible domain can be omitted, reducing computational cost further. The additional computational steps required to compute the boundary line are negligible compared to the computations that can be saved by application of this method. However, the method applies so far to optimal control problems with one state variable, only.

Finally, the optimal control map for the fuel optimal torque split on a full parallel hybrid vehicle is shown as a further example. The algorithm shown in this chapter is being used extensively in the following chapters mainly to evaluate the performance of suboptimal solutions with respect to the theoretical optimum.

Chapter 4

From Optimal Toward Causal Control

The optimal control evaluated with dynamic programming in Chapter 3 clearly yields the global optimal control for the given driving cycle. However, it cannot be applied for real-time applications due to many limitations. First, the driving cycle, i.e., the disturbance has to be known a priori. This means, that the control resulting from DP is fully predictive, hence, non-causal. Second, it is computationally expensive and therefore not suitable for real-time application. Therefore, part of the optimality has to be sacrificed in order to derive a causal control. Nevertheless, the global optimal solution is very valuable since it allows to benchmark the suboptimal, but causal controllers with respect to the global optimum that could be achieved theoretically. If a causal controller achieves performance that is close to the global optimum, it proves to be an appropriate control. Further, the global optimum can be applied to get insight into the structure of the optimal solution.

This chapter moves stepwise toward a fully causal control. First, the structure of an optimal control is derived by means of Pontryagin's minimum principle in Sec. 4.1. In order to render the problem solvable, some simplifications of the model have to be admitted. Pontryagin's minimum principle yields necessary conditions for the optimal control only. Hence, global optimality is not guaranteed. In Sec. 4.1.3, the necessary conditions for optimality that yield a two-point boundary value problem are solved numerically.

The step toward a causal controller is taken in Sec. 4.2, where the necessary conditions of optimality together with the insights of the optimal control are being used to derive a suboptimal, but fully causal control. At this stage, this causal control is only using information of the current state of the plant. This control relies on the model presented in Chapter 2 and

the resulting control cannot be expressed with analytic functions, it rather needs to perform some simple optimization using the model equations in real-time at every time sample. Although this online optimization can be carried out on a standard engine control unit (ECU), a computationally less expensive control is presented in Sec. 4.3 based on a simplified model. This simplified control is not only computationally attractive since the set of control candidates is solved analytically, this simplified control even yields a well defined control law. This law consists of simple rules that rely only on parameters of the powertrain. With this at hand, one can prove, that, for the simplified yet realistic model, rule-based strategies can be derived from optimal control theory.

4.1 Pontryagin's Minimum Principle

The optimal control problem formulated in Sec. 3.1 in its general form (3.1) and in its specific form (3.2) for the fuel optimal control of the full parallel HEV is hard to be solved using Pontryagin's minimum principle. This is a consequence of the problem having state constraints, having a partially constraint final state, and being time-variant. The state constraints, that could be well handled in DP, increase the complexity of the solution using Pontryagin's minimum principle considerably. As indicated in [24] generally and in [25] specifically for HEVs, such a problem can be solved if the number of intervals where the state constraints become active is known. In typical (time-invariant) optimal control problems the state constraints are active only during one interval in time. However, for the problem described in this work, it is a priori unknown at what time instances and how often the state constraints become active. The authors of [26] present an iterative, heuristic method to solve the optimal control problem of a state constrained HEV. However, the method is acausal and yields a suboptimal solution which is close to the global optimal solution. In this section, the state is assumed to be unconstrained unless otherwise stated in order to keep the problem solvable. This assumption can lead to solutions that violate the state constraints being present in the real model. However, this approach allows to derive the structure of an optimal control. At a later stage, a feedback control is introduced to keep the state-of-charge around some reference value. This SoC-control induces some additional fuel cost. Hence, a part of the optimality has to be sacrificed to keep the SoC away

from its constraints.

Furthermore, the optimal control problem (3.1) is defined with a target set for the final state. Physical considerations yield clearly that the fuel optimal solution of the HEV-problem will always target the lower bound of this target set. Any final state-of-charge that is higher than the necessary minimum final state corresponds to some energy stored in the battery that could have been used to further reduce fuel consumption. Hence, the target set of the final state can be reduced to a single point without loss of optimality of the solution:

$$\xi(t_f) \in [\xi_{f,min}, \xi_{f,min}] = \xi_{f,min} = \xi_f. \quad (4.1)$$

Summarizing, the optimal control problem of the HEV is with

- fixed final time t_f which is given by the duration of the driving cycle,
- unconstrained state by assumption,
- and fixed final state since the final target set can be reduced to a single point without impact on the optimal solution.

4.1.1 Necessary Conditions for Optimality

In order to state the necessary conditions for optimality, the Hamiltonian needs to be defined first. From (3.2b) and (3.2g) it results as

$$H(\xi(t), u(t), \lambda(t), t) = H_l \overset{*}{m}_f(u(t), t) - \lambda(t) \frac{I_{BT}(\xi(t), u(t), t)}{Q_0}, \quad (4.2)$$

where $\lambda(t)$ is the costate, which is sometimes also referred to as augmented variable, adjoint variable, or Lagrange multiplier.

According to Pontryagin's minimum principle, the optimal control signal u^o must satisfy the following necessary conditions [24, 27]:

1. State dynamics, boundary conditions, and costate dynamics:

$$\dot{\xi}^o(t) = \nabla_{\lambda} H|_{\circ} = - \frac{I_{BT}(\xi^o(t), u^o(t), t)}{Q_0} \quad (4.3a)$$

$$\xi^o(0) = \xi_0 \quad (4.3b)$$

$$\xi^o(t_f) = \xi_f \quad (4.3c)$$

$$\dot{\lambda}^o(t) = -\nabla_{\xi} H|_{\circ} = \lambda(t) \frac{1}{Q_0} \frac{\partial}{\partial \xi} I_{BT}(\xi^o(t), u^o(t), t) \quad (4.3d)$$

2. For all $t \in [0, t_f]$, the Hamiltonian $H(\xi^o(t), u^o(t), \lambda^o(t), t)$ has a global minimum with respect to $u \in [u_{min}(t), u_{max}(t)]$ at $u = u^o(t)$, i.e.,

$$H(\xi^o(t), u^o(t), \lambda^o(t), t) \leq H(\xi^o(t), u(t), \lambda^o(t), t). \quad (4.3e)$$

4.1.2 Physical Interpretation of the Necessary Conditions

The first of the necessary conditions (4.3a) simply yields back the state dynamics of the system. The second (4.3b) and third condition (4.3c) impose the initial and final condition on the system. If the final condition is chosen identical to the initial condition, the vehicle will be operated such that the battery's charge is sustained over the driving cycle and the entire energy consumption of the vehicle is covered from fuel energy. The fourth condition (4.3d) yields the dynamics of the costate. For the current problem, neither an initial nor a final condition on the costate are being imposed. The optimal, continuous-time control problem, which is of infinite size, is reduced to a problem of finite size using Pontryagin's minimum principle. The remaining problem consists only on finding an initial condition on the costate such that all the necessary conditions are met. This is a one-dimensional problem, here. The physical meanings of the costate λ and the Hamiltonian H are not obvious so far. Introducing the following substitution of the costate with a dimensionless variable

$$s(\xi(t), t) := -\frac{\lambda(t)}{V_{oc}(\xi(t))Q_0}, \quad (4.4)$$

yields the following expression for the Hamiltonian:

$$\begin{aligned} H(\xi(t), u(t), s(t), t) &= H_l \cdot \overset{*}{m}_f(\cdot) + s(\cdot)V_{oc}(\cdot)Q_0 \frac{I_{BT}(\cdot)}{Q_0}, \\ &= P_f(u(t), t) + s(\xi(t), t) \cdot P_{BT,i}(\xi(t), u(t), t), \end{aligned} \quad (4.5)$$

where P_f and $P_{BT,i}$ are the fuel power and the *inner* battery power given by

$$P_f(\cdot) = H_l \cdot \overset{*}{m}_f(\cdot) \quad (4.6)$$

$$P_{BT,i}(\cdot) = V_{oc}(\cdot) \cdot I_{BT}(\cdot). \quad (4.7)$$

The physical meaning of the Hamiltonian and the introduced variable s become much clearer from the form of equation (4.5). The fuel power P_f and the inner battery power $P_{BT,i}$ are summed up, weighted by s . If for example the vehicle is operated in pure thermal mode, the battery's current is zero and the value of the Hamiltonian is the current (fuel) power consumption of the vehicle. If the engine would now be operated at slightly higher load than required from the driving cycle, the electric path must provide some negative power to meet the power balance. This negative power is a recharging power according to the sign definition introduced in Chapter 2 of the model. The value of the Hamiltonian is then the increased fuel power reduced by a weighted negative electric power. It seems that the value of the Hamiltonian represents an *equivalent fuel power*. The normalized costate variable s converts the inner battery power into a quantity of equivalent fuel power. Hence, the variable s is referred to as *equivalence factor* as firstly mentioned in [28, 29].

Finally, the necessary condition (4.3e) simply expresses that the optimal control action at every time is found as the global minimizer of the Hamiltonian along the optimal trajectory. In other words, the equivalent fuel power computed with the optimal equivalence factor must be minimized at every time. This minimization of the Hamiltonian typically yields a finite set of optimal control signals out of the continuous space of admissible control signals.

In literature, such approaches for evaluating the fuel optimal control of HEVs have been introduced much earlier. The authors of [5, 6, 7] found by physical reasoning that minimizing some equivalent fuel consumption at every time step, i.e., minimizing a local cost function instead of minimizing the integral cost function, yields results that are very close to the optimal solution. Later, it was shown by [10] that the idea of minimizing a local cost function can be derived from optimal control.

4.1.3 Two-Point Boundary Value Problem

The problem resulting from the necessary conditions for optimality (4.3) from Sec. 4.1.1 is a two-point boundary value problem (2PBVP). To solve this problem, the initial condition for the costate $\lambda(0)$ must be found such that the resulting final state $\xi(t_f)$ from applying the Hamiltonian minimizing control meets the specified final state ξ_f . This initial costate can be found by a shooting method.

Since the sensitivity of the current of the battery I_{BT} on the state-of-charge ξ is small, the partial derivative $\frac{\partial I_{BT}(\cdot)}{\partial \xi}$ is assumed to be zero. With this assumption, the costate dynamics (4.3d) result as

$$\dot{\lambda}(t) = \lambda(t) \frac{1}{Q_0} \frac{\partial}{\partial \xi} I_{BT}(\xi(t), u(t), t) \approx 0. \quad (4.8)$$

Hence, the costate is a constant and is identical to its initial value:

$$\lambda(t) = \lambda(0) = \lambda_0. \quad (4.9)$$

In order to justify this assumption, the two-point boundary value problem with the assumed constant costate is solved for the problem without state constraints. The simulations are carried out for four regulatory driving cycles, namely NEDC, CADC, ARB-02, and FTP-75. These driving cycles are shown in Appendix B. The engine-off phase of the FTP-75 of 600 s has been removed because thermal effects are neglected in the model.

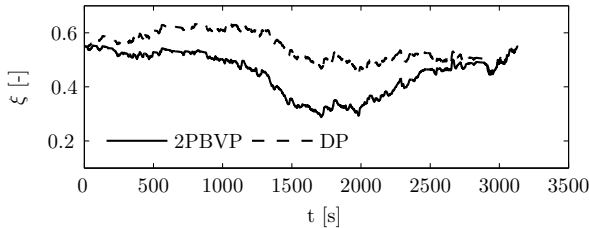
The resulting state trajectory for CADC is shown in Fig. 4.1. This graph shows that both state-of-charge trajectories have identical initial and final states as specified. The trajectory resulting from DP is with higher values for the state-of-charge. This is a consequence of the battery having a higher efficiency at higher SoC. Since the dynamics of the costate are neglected, the two-point boundary value problem does not account for this effect appropriately. In order to quantify the optimality of the solution, the resulting fuel consumption of the two-point boundary value problem is compared to the fuel consumption resulting from DP. The relative difference between the fuel consumption FC_S achieved by any strategy S and the fuel consumption FC_{DP} resulting from DP is expressed as the *relative excess consumption* rEC which is defined as

$$rEC = \frac{FC_S - FC_{DP}}{FC_{DP}}. \quad (4.10)$$

The resulting fuel consumptions FC are summarized in Table 4.1, together with the relative excess consumption rEC , the constant costate λ_0 , and the maximum and minimum value of the state-of-charge trajectory. The final states, achieved for the two-point boundary value problem and for DP, lie within $6 \cdot 10^{-4}$ from the specified final state for all four cycles. The maximum difference between these two final states over all four cycles is less than $2 \cdot 10^{-10}$. This shows, that the simulations are valid and well comparable.

Table 4.1: Simulation results for the two-point boundary value problem.

Cycle	FC (2PBVP/DP) [l/100km]	rEC [%]	λ_0 [J]	max/min($\xi(t)$) [-]
NEDC	4.79/4.79	0.166	$-1.454 \cdot 10^7$	0.55/0.28
CADC	6.67/6.67	0.055	$-1.387 \cdot 10^7$	0.55/0.29
ARB-02	6.64/6.64	0.007	$-1.386 \cdot 10^7$	0.72/0.49
FTP-75	4.47/4.47	-0.005	$-1.452 \cdot 10^7$	0.60/0.41

**Figure 4.1:** State-of-charge trajectories for the two-point boundary value problem with a constant costate and for DP on CADC.

The fuel consumption resulting from solving the two-point boundary value problem with the assumption of a constant costate is very close to the optimum evaluated by DP. It is important to note that the solution of DP has some very small deviation from the global optimum, resulting in a negative rEC for the case of the FTP-75 driving cycle. This is due to the fact, that DP can only be evaluated on a discretized state-space. Since the optimal cost-to-go at the end of each time-step is interpolated linearly between the grid points, some small errors occur due to nonlinearities in the optimal cost-to-go. The two-point boundary value problem, in contrast, is evaluated continuously in the state-space. This can lead to slightly better fuel consumption in some special cases. It is important to note that the two-point boundary value problem is acausal because the initial condition for the costate has to be evaluated using the entire driving cycle.

4.2 Causal Approach

All the controls presented so far in this chapter are acausal, i.e., the decision of the control action depends on information on the future driving cycle. In order to derive a control law that can be used in a real vehicle, it must be fully causal. Therefore, a fully causal control strategy is derived in this section. Hence, it must be assumed that there is no information available on future driving conditions. Since the future driving cycle is unknown at this stage and the battery is bounded, it must be made sure that the state-of-charge remains within some bounds. This issue can be addressed by penalizing state-of-charge deviations from some set-point that lies in between the lower and the upper bound of the battery. This results in an extension of the original optimal control problem stated in (3.2). The cost functional J given by equation (3.2g) is then extended with such a penalty on state-of-charge deviation.

4.2.1 Derivation of Causal Control with SoC-Penalty

The cost functional (3.2g) extended with a penalty on state-of-charge deviations results in the extended cost functional \tilde{J} , given by

$$\tilde{J}(u(t)) = \int_0^{t_f} \left\{ H_l \cdot \dot{m}_f(u(t), t) + \alpha \left(\frac{\xi_{ref}(t) - \xi(t)}{\Delta \xi_{nrm}} \right)^{2q} \right\} dt, \quad (4.11)$$

where α is a weighting parameter, $\Delta \xi_{nrm}$ normalizes the deviation, and $q \in \mathbb{N}$ determines the order of the penalty. The normalization with $\Delta \xi_{nrm}$ is introduced to assure that a deviation of $\Delta \xi_{nrm}$ from the set-point ξ_{ref} yields a penalty of α independent of the choice of q .

The Hamiltonian resulting for this extended cost functional is

$$\tilde{H}(\xi, u, \lambda) = H_l \cdot \dot{m}_f(u) + \alpha \left(\frac{\xi_{ref} - \xi}{\Delta \xi_{nrm}} \right)^{2q} - \lambda(t) \cdot \frac{I_{BT}(\xi, u)}{Q_0}, \quad (4.12)$$

and the H-minimizing control results as

$$u^o = \underset{u}{\operatorname{argmin}} \tilde{H}(\xi^o, u, \lambda^o). \quad (4.13)$$

Assuming the optimal cost-to-go function $\tilde{J}^o(\xi, t)$ corresponding to the extended cost functional \tilde{J} would be known, the optimal costate is found

as the gradient of the optimal cost-to-go in the state. This is a result from Hamilton-Jacobi-Bellman-theory and the interested reader is referred to [24]. Hence, the optimal costate is then given by

$$\lambda^o(\xi, t) = \frac{\partial \tilde{\mathcal{J}}^o(\xi, t)}{\partial \xi}. \quad (4.14)$$

Since no knowledge is available on future driving conditions, it is not possible to evaluate the optimal cost-to-go function $\tilde{\mathcal{J}}^o(\xi, t)$. Therefore, a (suboptimal) cost-to-go function is estimated as a function of the state-of-charge, but independent of time. The (suboptimal, time-invariant) cost-to-go function is estimated as follows: The cost functional (4.11) penalizes the fuel consumption as well as any SoC deviation from the reference value. The fuel consumption is assumed to consist of two parts. The first part represents the fuel energy $\mathcal{J}_{f,1}(\xi)$ that would be used to re- or discharge the battery in future from the actual state-of-charge back to the reference value. The second part represents the remaining fuel energy use $\mathcal{J}_{f,2}$ which is assumed to be independent of the current state-of-charge. Therefore, the estimated cost-to-go function is written as

$$\tilde{\mathcal{J}}(\xi) = \mathcal{J}_{f,1}(\xi) + \mathcal{J}_{f,2} + \mathcal{J}_{SoC}(\xi), \quad (4.15)$$

where \mathcal{J}_{SoC} denotes the cost due to SoC deviations from the reference value.

Since only the gradient of the cost-to-go function in the state-of-charge is of interest (4.14), the term $\mathcal{J}_{f,2}$ does not need to be resolved. The fuel energy used to compensate the current state-of-charge needs to be approximated. The energy stored in the battery at a state-of-charge of $\xi(t)$ with respect to the energy at the reference state-of-charge ξ_{ref} is computed by

$$E_{BT,\Delta\xi} = Q_0 \int_{\xi(t)}^{\xi_{ref}} V_{oc}(\tilde{\xi}) d\tilde{\xi}. \quad (4.16)$$

This energy due to a deviation from the reference state-of-charge must be compensated in future using the thermal path. Hence, the fuel energy used/saved to recharge/discharge the battery depends on the efficiency of the engine, but also on the efficiency of the electric path. These efficiencies depend on the future operating points and are unknown at this stage. Therefore, a constant average conversion efficiency η_c is assumed.

The fuel energy required to compensate the state-of-charge deviation is consequently estimated by

$$\mathcal{J}_{f,1}(\xi) \cong \frac{E_{BT,\Delta\xi}}{\eta_c} = \frac{Q_0}{\eta_c} \int_{\xi(t)}^{\xi_{ref}} V_{oc}(\tilde{\xi}) d\tilde{\xi}. \quad (4.17)$$

The SoC penalty term \mathcal{J}_{SoC} is estimated based on the assumption that the SoC is controlled such that it is brought back from the current value $\xi(t)$ to the reference value ξ_{ref} in time T_h . This future SoC trajectory $\xi_{fut}(\tau)$ is assumed to be affine in time

$$\xi_{fut}(\tau) = \xi(t) - \frac{\xi(t) - \xi_{ref}}{T_h} \cdot \tau. \quad (4.18)$$

The cost resulting from the second term of (4.11) combined with the assumed future SoC trajectory from (4.18) is

$$\mathcal{J}_{SoC}(\xi) = \int_0^{T_h} \alpha \left(\frac{\xi_{ref} - \xi_{fut}(\tau)}{\Delta\xi_{nrm}} \right)^{2q} d\tau = \frac{\alpha T_h}{1 + 2q} \cdot \left(\frac{\xi_{ref} - \xi(t)}{\Delta\xi_{nrm}} \right)^{2q}. \quad (4.19)$$

Hence, the estimation of the cost-to-go function obtained from (4.15), (4.17), and (4.19) is

$$\begin{aligned} \tilde{\mathcal{J}}(\xi) &= \mathcal{J}_{f,1}(\xi) + \mathcal{J}_{f,2} + \mathcal{J}_{SoC}(\xi) \\ &= \frac{Q_0}{\eta_c} \int_{\xi(t)}^{\xi_{ref}} V_{oc}(\tilde{\xi}) d\tilde{\xi} + J_{f,2} + \frac{\alpha T_h}{1 + 2q} \cdot \left(\frac{\xi_{ref} - \xi(t)}{\Delta\xi_{nrm}} \right)^{2q}. \end{aligned} \quad (4.20)$$

The corresponding suboptimal, time-invariant costate resulting from (4.14) and (4.20) thus becomes

$$\lambda(\xi) = \frac{\partial \tilde{\mathcal{J}}(\xi)}{\partial \xi} = -\frac{Q_0 V_{oc}(\xi)}{\eta_c} - \tilde{\alpha} \cdot (\xi_{ref} - \xi(t))^{2q-1}, \quad (4.21)$$

with the substitution

$$\tilde{\alpha} := \frac{2q\alpha T_h}{(1 + 2q)\Delta\xi_{nrm}^{2q}}. \quad (4.22)$$

Summarizing, the suboptimal but causal control $u(\xi)$ is the minimizer of the extended Hamiltonian \tilde{H} (4.12), where the suboptimal, causal costate $\lambda(\xi)$ is computed with (4.21). An interesting property of the extended Hamiltonian is that the term containing the SoC-penalty is not an explicit function of the control signal u . Hence, the extended Hamiltonian \tilde{H} yields the same minimizer as the original Hamiltonian H (4.3e).

4.2.2 Summary of the Causal Control: ECMS

In order to express the H-minimizing control with more intuitive quantities, the substitution of λ with s (4.4) is used again. The resulting, causal equivalence factor is then

$$s(\xi) = \frac{1}{\eta_c} + \frac{\tilde{\alpha}}{Q_0 V_{oc}(\xi)} \cdot (\xi_{ref} - \xi(t))^{2q-1}. \quad (4.23)$$

The average conversion efficiency η_c varies slightly with the driving profile because it depends on the operating points of the components and these operating points are depending on the driving cycle. Therefore, the value of η_c is adjusted during operation to keep the state-of-charge trajectory around the set-point ξ_{ref} . This can be achieved using an integrator with integration time T_i . Furthermore, $1/\eta_c$ is substituted by s_0 for convenience.

Summarizing, the suboptimal, causal control is given by

$$u = \underset{\tilde{u}}{\operatorname{argmin}} \{P_f(\tilde{u}) + s(\xi) \cdot P_{BT,i}(\xi, \tilde{u})\} \quad (4.24a)$$

$$s(\xi(t)) = s_0 + \int_0^t \frac{\xi_{ref} - \xi(\tau)}{T_i} d\tau + \frac{\tilde{\alpha}(\xi_{ref} - \xi(t))^{2q-1}}{Q_0 V_{oc}(\xi)}. \quad (4.24b)$$

where $P_f(u) = H_l \cdot \dot{m}_f(u)$ is again the fuel power consumed by the engine and $P_{BT,i}(\xi, u) = V_{oc}(\xi) I_{BT}(\xi, u)$ is the inner battery power for the actual torque split.

Since the Hamiltonian represents an equivalent fuel power that must be minimized at every time, this control is referred to as equivalent consumption minimization strategy (ECMS) in consistency with the literature [28, 29].

This ECMS can easily be implemented in a vehicle. A block diagram of the structure of such an implementation is shown in Fig. 4.2. The inputs to the strategy are:

- The state-of-charge of the battery. This quantity cannot be measured directly, but there exist reliable methods to estimate it with sufficient accuracy. The authors of [30] successfully developed an extended Kalman filter to estimate the SoC. The necessary measurements are the terminal current I_{BT} and the terminal voltage V_{BT} of the battery.
- The reference value ξ_{ref} for the state-of-charge. For the case where no information on future driving conditions is available, this quantity is set to a constant value.

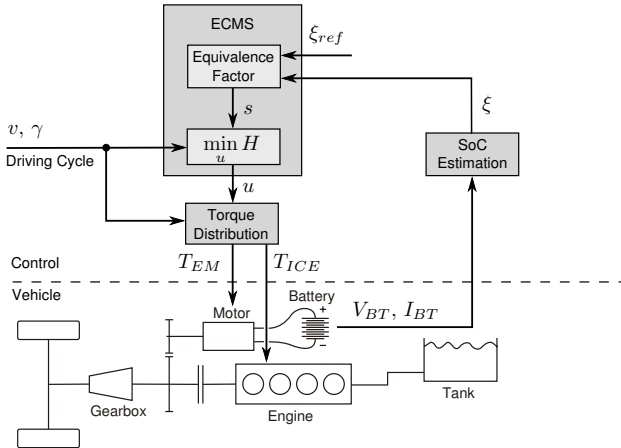


Figure 4.2: System level block diagram of the ECMS control system with the vehicle.

- The demand determined by the driving cycle. In a real vehicle, it is the driver that requests a torque from the powertrain by the accelerator and brake pedals, the rotational speed of the gearbox is measured. In the simulation environment used here, the requested torque and speed at the gearbox are computed from the data of the driving cycle.

Such an implementation has been carried out successfully on a prototype of a full parallel HEV together with the industrial partner.

This control strategy has some important properties that are worth to be recalled here. A first important point is its causality. All the decisions are only taken from information on the present and the past. The ECMS is therefore non-predictive. Secondly, this structure includes a feedback path such that the state-of-charge is controlled. A third property is that the strategy is capable to track some reference value for the state-of-charge. This property will be used in Chapter 5 to extend this non-predictive ECMS.

4.2.3 Results and Limitations of the ECMS

The non-predictive ECMS from Sec. 4.2.2 is compared now to the global optimum obtained using DP. However, no non-predictive strategy can guarantee to be perfectly charge sustaining. Therefore, the non-predictive ECMS is simulated first with an initial state-of-charge of $\xi(0) = 0.55$ achieving some final state $\xi(t_f)$. The DP solution is then evaluated using these initial and final conditions on ξ . Since the precision of the achieved final state is crucial to yield a proper evaluation, numerical issues in the DP algorithm must be treated appropriately as discussed in Chapter 3 and [20, 21]. This procedure of evaluating the non-predictive against the global optimal strategy with identical initial and final state yields a ‘fair’ comparison of the two strategies without the need for converting electric energy into a fuel equivalent. The relative difference between suboptimal and optimal fuel consumption are again expressed with the relative excess consumption rEC (4.10) that is defined in Sec. 4.1.3.

The driving cycles used for the evaluations are standard regulatory driving cycles such as the NEDC, the CADC, the ARB-02, and the FTP-75. These regulatory driving cycles are shown in Appendix B. In addition, new driving cycles with topographic profiles are proposed here. These cycles are labeled FTPelv, US06elv, and SWISSelv whose profiles are shown in Fig. 4.3. The first cycle, FTPelv, is constructed by addition of an altitude profile to the FTP-75. The engine-off phase of the FTP-75 of 600 s has been removed for the FTPelv cycle because thermal effects are neglected. The altitude profile is obtained from the public database ADVISOR [31], namely from its driving cycle ‘NREL2VAIL’ that is a measured driving cycle. From this altitude profile, only the section from km 14 to km 32 is considered. The second cycle, US06elv, consists of a part of the speed profile of the regulatory driving cycle US06 and is scaled down to a maximum speed of 80 km/h. The altitude profile is extracted from topographic maps of a real, representative road in the surroundings of Zurich. The third cycle, SWISSelv, has been recorded in Switzerland and shows a relatively large amount of elevation changes.

The parameters used to evaluate the ECMS are summarized in Table 4.2. They are tuned for the urban part of the Common Artemis Driving Cycle (CADC-Urban) and for the vehicle defined in Chapter 2 as follows: The parameter q is chosen as $q = 2$ in order to penalize large SoC deviations severely while having a soft penalty on small deviations. The

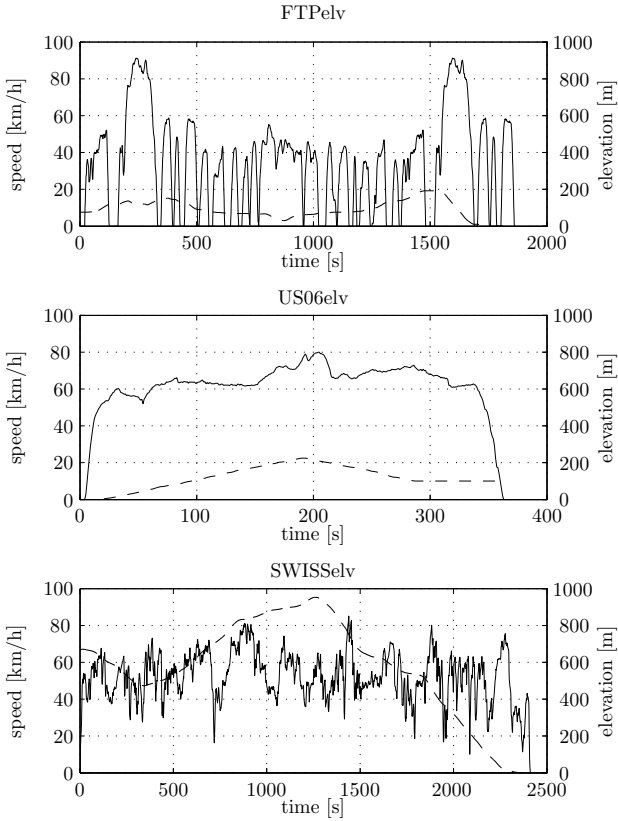


Figure 4.3: The three driving cycles with speed (solid) and topographic profiles (dashed).

Table 4.2: Parameters for the ECMS.

Parameter	Value	Unit
s_0	2.8	-
T_i	100	s
ξ_{ref}	0.55	-
$\Delta\xi_{nrm}$	0.1	-
q	2	-
T_h	500	s
α	2000	W

reference SoC ξ_{ref} is centered between the lower and the upper bound, the typical SoC deviation used for normalization is set to $\Delta\xi_{norm} = 0.1$. The crucial parameters, however, are s_0 , α , and T_i . In a first step, the basic equivalence factor s_0 is evaluated by using no SoC control, i.e., $\alpha = 0$ and $T_i = \infty$. An iterative search for the charge-sustaining s_0 yields $s_0 = 2.77$ for urban part of CADC. Hence, a rounded value of $s_0 = 2.8$ is applied. The control parameters α and T_i are found manually such that the SoC deviation from the set point is less than 0.05.

Table 4.3: Simulation results for the ECMS.

Cycle	FC (ECMS/DP) [l/100km]	rEC [%]
NEDC	5.46 / 5.33	+2.4
CADC	6.72 / 6.71	+0.2
ARB-02	6.74 / 6.72	+0.3
FTP-75	4.73 / 4.70	+0.7
FTPelv	4.55 / 4.20	+8.3
US06elv	8.07 / 7.64	+5.7
SWISSelv	3.90 / 3.54	+10.1

The simulation results are summarized in Table 4.3, which shows the fuel consumption and the relative excess consumption rEC as defined by (4.10). These results show that the ECMS provides close to optimum fuel consumption for most flat standard cycles. The rEC increases only for driving cycles with long recuperation phases such as the NEDC that has a long final deceleration phase. The situation changes substantially as soon as elevation changes are considered. This can be seen in the simulation results of the cycles FTPelv, US06elv, and SWISSelv, where the topographic profile leads to an rEC value ranging from 5.7% up to 10.1%. This large difference between achieved fuel consumption and optimal fuel consumption is mainly due to the fact that the (non-predictive) ECMS tries to keep the SoC near the reference value ξ_{ref} that is centered between the lower and upper constraints, ξ_{min} and ξ_{max} , respectively. Consequently, if a longer recuperation phase occurs, only a fraction of the recuperable energy can be stored in the battery before its capacity limits are reached. Therefore, better approaches are necessary which avoid this limitation, particularly in hilly driving profiles. As announced by [12], this can only

be achieved by using predictive strategies.

4.3 Optimal Control with a Simplified Model

The causal control presented in Sec. 4.2 is a purely model based approach that yields a fuel consumption which is close to the global optimum for most driving cycles. The control signal is found by online minimization of the Hamiltonian. This minimization is carried out numerically and requires some evaluations of the Hamiltonian. This is computationally expensive and the control law resulting from minimizing the Hamiltonian is not explicit.

In this section, a simplified model of the hybrid vehicle is presented. This simplified model allows for analytical minimization of the Hamiltonian and yields an explicit control law that is a function of powertrain parameters, the requested power, and the equivalence factor, only. This analytic control law is computationally very attractive and shows clearly the relation between requested power, the equivalence factor, and the resulting optimal control signal.

In a first part, a very simple model is introduced. This model has almost no constraints on the electric motor and the engine. Further, the powertrain parameters are assumed to be not a function of the rotational speed. Hence, this model is speed-independent and has no input constraints. However, the resulting control law is very simple and offers great understanding. This is presented in Sec. 4.3.1.

In a second part, namely Sec. 4.3.2, the model is extended with input constraints, namely on the electric motor and the engine. Further, the powertrain parameters are expressed as a function of the rotational speed of the powertrain, i.e., the model is speed-dependent. This extended model is validated in Sec. 4.3.2 using the original model that was introduced in Chapter 2.

4.3.1 Optimal Control with Unconstrained, Speed-Independent Model

In this section, the simplified, unconstrained model of a parallel hybrid electric powertrain is presented. Based on this model, the optimal control is derived and illustrated.

Unconstrained, Speed-Independent Model

For a parallel hybrid electric powertrain whose structure is illustrated in Fig. 4.4, we use a simplified model relating the total power demand $P_d(t)$, the motor power $P_m(t)$, and the engine power $P_e(t)$ to the fuel power $P_f(t)$, the battery power $P_b(t)$, and the energy content in the battery $E_b(t)$. Assuming a battery model with a voltage source V_{OC} in series with a resistor R , the battery current I_b is given by

$$I_b = \frac{V_{OC} - \sqrt{V_{OC}^2 - 4RP_b}}{2R}. \quad (4.25)$$

The total power loss over the resistance is

$$P_l(P_b) = RI_b^2 = \frac{\left(V_{OC} - \sqrt{V_{OC}^2 - 4RP_b}\right)^2}{4R}. \quad (4.26)$$

Approximating the power loss using a Taylor series around $P_b = 0$ yields

$$P_l(P_b) \approx P_l(0) + \left. \frac{\partial P_l}{\partial P_b} \right|_0 \cdot \frac{P_b}{1!} + \left. \frac{\partial^2 P_l}{\partial P_b^2} \right|_0 \cdot \frac{P_b^2}{2!} + \mathcal{O}(P_b^3) \quad (4.27)$$

$$= 0 + 0 \cdot P_b + \frac{R}{V_{OC}^2} \cdot P_b^2 + \mathcal{O}(P_b^3). \quad (4.28)$$

The battery power loss in the simplified model is therefore assumed to be

$$P_l(P_b) = \frac{R}{V_{OC}^2} \cdot P_b^2 = \beta P_b^2. \quad (4.29)$$

The model equations are

$$P_e(t) = P_d(t) - P_m(t) \quad (4.30a)$$

$$P_f(t) = \frac{P_e(P_m(t), P_d(t)) + P_0}{e} \cdot B \quad (4.30b)$$

$$P_b(t) = P_m(t) \cdot \eta^{-\text{sign}(P_m(t))} \quad (4.30c)$$

$$\frac{d}{dt} E_b(t) = -P_b(P_m(t)) - \beta P_b(P_m(t))^2, \quad (4.30d)$$

where B is equal to one when the fuel injection is active (engine on) and the clutch between engine and motor is engaged, ($P_e(t) > 0$), P_0 is the engine friction power, e its internal efficiency, η the efficiency of the electric motor,

and $\beta = \frac{R}{V^2}$. The only state variable of this model is the energy content of the battery $E_b(t)$ given by (4.30d). In the remainder of this section the time dependencies of the variables P_d , P_e , P_m , P_f , P_b , and E_b in the model equations (4.30) are omitted to increase readability. The parameters of the un-constrained, speed-independent model are given in Table 4.4.

Initially, the only constraint to the model is that the engine cannot provide any negative power,

$$P_e \in [0, \infty) \quad (4.31)$$

$$P_m \in (-\infty, \infty). \quad (4.32)$$

However, in Sec. 4.3.2 constraints are added to the model in order to achieve a more realistic behavior.

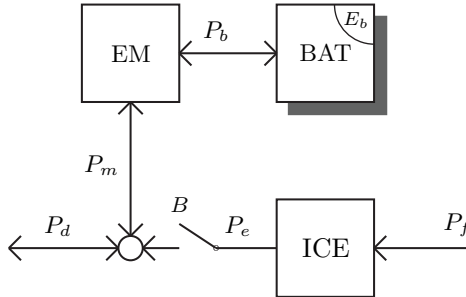


Figure 4.4: Topology of the parallel hybrid electric powertrain. EM and ICE are static blocks while BAT is a dynamic block with the state variable E_b . The variable B decides whether the engine is on and the clutch is closed.

Table 4.4: Parameters of the powertrain.

Parameter	Value	Unit
P_0	$4.5 \cdot 10^3$	W
e	0.4	-
η	0.9	-
R	0.5	Ω
V_{OC}	300	V
$\beta = \frac{R}{V_{OC}^2}$	$\approx 5.6 \cdot 10^{-6}$	W^{-1}

Optimal Control

The optimal control problem consists of finding the optimal power signal for the electric motor P_m^o such that the fuel consumption is minimized and the charge in the battery is sustained over the driving cycle. The requested power profile P_d is given by the driving cycle as a disturbance and the final time t_f , being the duration of the cycle, is fixed.

The optimal control problem is formulated by the cost functional, the system dynamics, input constraints and state constraints, and the initial and the final condition. The cost functional to be minimized, which is the total fuel (energy) consumption over the driving cycle, is

$$J = \int_0^{t_f} P_f(\tau) d\tau. \quad (4.33)$$

While the system dynamics and input constraints are given by (4.30)–(4.32), the state constraints are neglected throughout this section. The initial and the final condition are chosen equal to zero such that charge sustenance is guaranteed

$$E_b(0) = E_b(t_f) = 0. \quad (4.34)$$

Hence, a positive (negative) battery energy content $E_b(t)$ indicates that the battery is charged (discharged) at time t compared to the initial condition. Note that the energy content of batteries is in general bounded. However, the optimal control problems solved here neglect the bounds on the state. This assumption allows for explicit solutions. Nevertheless, as it will be shown in Sec. 4.3.4, the battery's energy content can still be kept within reasonable bounds by an appropriate causal control.

Resulting Optimal Control Law

The optimal control problem stated above is solved using Pontryagin's minimum principle. This method has been successfully applied in Sec. 4.1 and 4.2. However, the simplified model presented here allows solving explicitly for the optimal control law, which can be represented as a clearly defined map. This map is shown in Fig. 4.5 for a powertrain with the parameters specified in Table 4.4. It contains the optimal motor power as a function of a constant equivalence factor s and the requested power P_d . The constant equivalence factor s is introduced in Sec. 4.3.1 below,

where the optimal control law is derived in detail. The optimal control law consists of only four regions, namely pure electric driving (including recuperation), pure thermal, boosting, and recharging.

The power limits $P_{lim}^{(\cdot)}$ separating the four regions in the control map are given by

$$P_{lim}^{bo}(s) = \frac{-\left(\frac{s}{\eta} - \frac{1}{e}\right) + \sqrt{4\frac{s\beta}{\eta^2} \frac{P_0}{e}}}{2\frac{s\beta}{\eta^2}} \quad (4.35a)$$

$$P_{lim}^{th}(s) = \frac{-\left(\frac{s}{\eta} - \frac{1}{e}\right) + \sqrt{\left(\frac{s}{\eta} - \frac{1}{e}\right)^2 + 4\frac{s\beta}{\eta^2} \frac{P_0}{e}}}{2\frac{s\beta}{\eta^2}} \quad (4.35b)$$

$$P_{lim}^{re}(s) = \frac{-\left(\frac{s}{\eta} - \frac{1}{e}\right) + \sqrt{\left(\frac{s}{\eta} - \frac{1}{e}\right)^2 - \left(\frac{s}{\eta} - \frac{1}{e\eta^2}\right)^2 + 4\frac{s\beta}{\eta^2} \frac{P_0}{e}}}{2\frac{s\beta}{\eta^2}} \quad (4.35c)$$

$$P_{lim}^{re-}(s) = \frac{-(s\eta - \frac{1}{e}) + \sqrt{4s\beta\eta^2 \frac{P_0}{e}}}{2s\beta\eta^2}. \quad (4.35d)$$

These power limits show the clear advantage of the simplified model presented in this section, namely the fact that the resulting optimal control is a simple rule-based controller. However, it is completely defined by physical powertrain parameters and it is derived using Pontryagin's minimum principle.

The optimal control corresponding to the map shown in Fig. 4.5 is mathematically expressed as

$$P_m^o(P_d, s) = \begin{cases} \frac{\eta(\frac{\eta}{e} - s)}{2s\beta}, & \text{if } (P_d > 0) \cap (s < \frac{\eta}{e}) \\ & \cap (P_d > P_{lim}^{bo}(s)) \\ 0, & \text{if } (P_d > 0) \cap (\frac{\eta}{e} \leq s \leq \frac{1}{\eta e}) \\ & \cap (P_d > P_{lim}^{th}(s)) \\ -\frac{s - \frac{1}{\eta e}}{2s\beta\eta}, & \text{if } (P_d > 0) \cap (s > \frac{1}{\eta e}) \\ & \cap (P_d > P_{lim}^{re}(s)) \\ -\frac{s - \frac{1}{\eta e}}{2s\beta\eta}, & \text{if } (P_d < 0) \cap (P_d > P_{lim}^{re-}(s)) \\ P_d, & \text{otherwise.} \end{cases} \quad (4.36)$$

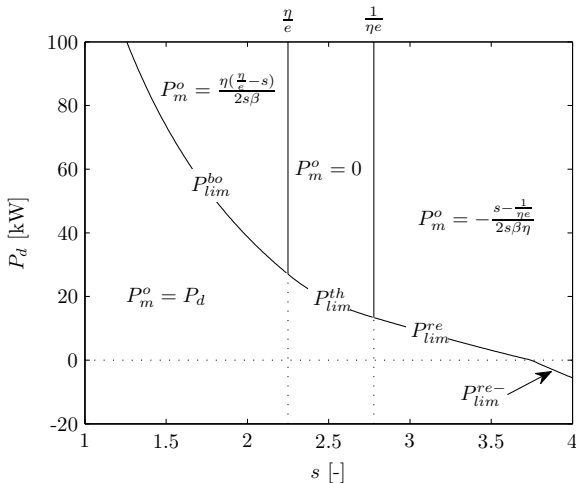


Figure 4.5: Overview of the regions with the different optimal control P_m^o (separated by solid lines) and the power limits $P_{lim}^{(\cdot)}$ for the unconstrained problem.

Example on a Driving Cycle

The optimal control law (4.36) as a function of the power demand P_d and the equivalence factor s is applied in this section to a regulatory driving cycle, namely the CADC which is shown in Appendix B. The remaining problem consists of finding a constant equivalence factor that guarantees the charge sustenance for the driving cycle. Figure 4.6 shows the final energy content in the battery when the optimal control law (4.36) is applied with the powertrain parameters given in Table 4.4. The charge-sustaining equivalence factor is found by a root finding algorithm at $E_b(t_f) = 0$.

The shaded area in Fig. 4.7 illustrates the instances during which the engine is used to recharge the battery, with $P_m = -2187.1$ W. As stated by the optimal control law (4.36), the threshold that determines between pure electric and recharging operation is a power limit as shown in the upper graph of Fig. 4.7. The bottom part of the figure shows the speed profile and illustrates clearly that there is no speed limit deciding between electric or recharging modes.

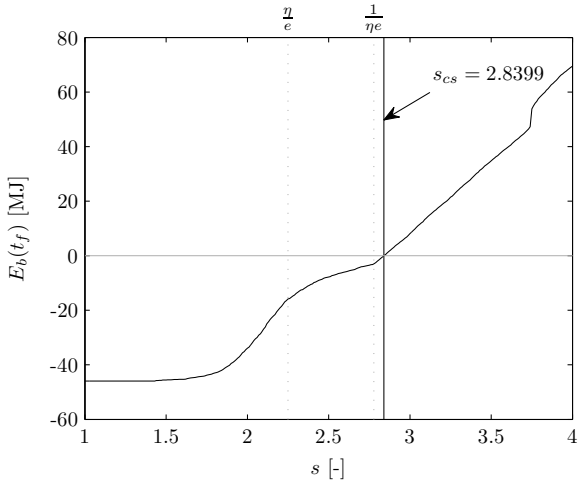


Figure 4.6: Energy in the battery E_b at final time t_f on CADC as a function of the equivalence factor s . The charge-sustaining value s_{cs} is indicated by the vertical line.

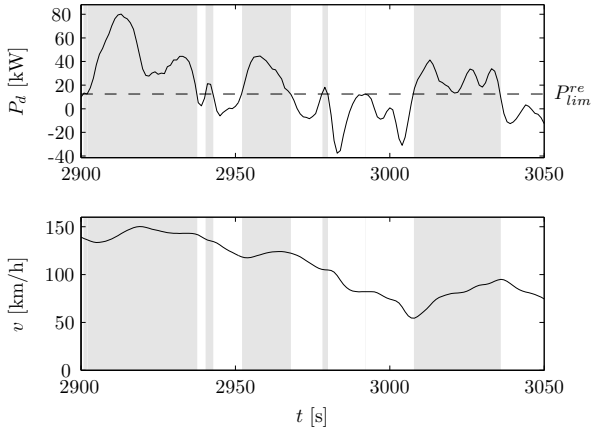


Figure 4.7: Power and speed profile $P_d(t)$ and $v(t)$ of CADC on the interval $t \in [2900, 3050]$ with the optimal control. Gray indicates recharging mode ($P_m = -2187.1$ W), white indicates electric mode ($P_m = P_d$).

Pontryagin's Minimum Principle: Derivation of the Optimal Control Law

As mentioned above, this section shows the detailed derivation of the optimal control law using the simplified model. The formulation of the optimal control problem defined by (4.30)–(4.34) yields the Hamiltonian [27]

$$\begin{aligned} H &= P_f - \lambda \cdot (P_b + \beta P_b^2) \\ &= \frac{P_d - P_m + P_0}{e} \cdot B - \lambda \left(P_m \eta^{-\text{sign}(P_m)} + \beta P_m^2 \eta^{-2 \text{sign}(P_m)} \right). \end{aligned} \quad (4.37)$$

If the control P_m^o is optimal, then the conditions (4.38) are satisfied according to Pontryagin's minimum principle.

$$\frac{d}{dt} E_b^o = -P_m^o \cdot \eta^{-\text{sign}(P_m^o)} - \beta \left(P_m^o \cdot \eta^{-\text{sign}(P_m^o)} \right)^2 \quad (4.38a)$$

$$E_b^o(0) = 0 \quad (4.38b)$$

$$E_b^o(t_f) = 0 \quad (4.38c)$$

$$\frac{d}{dt} \lambda^o = -\nabla_{E_b} H|_o = 0 \quad (4.38d)$$

$$H(P_m^o, \lambda^o, t) \leq H(P_m, \lambda^o, t) \quad (4.38e)$$

These conditions are necessary for optimality. Since the Hamiltonian is not a function of the state variable E_b , the optimal costate λ^o is constant. Throughout this section the constant optimal costate (4.39), with inverted sign, is referred to as *equivalence factor*, s , since it is weighting the electric power in the battery with the chemical power provided by fuel in the Hamiltonian (4.37).

$$\lambda^o(t) = -s \quad (4.39)$$

Equation (4.38e) states that P_m^o can only be optimal if it is the global minimizer of the Hamiltonian. Therefore, the Hamiltonian is carefully analyzed in the following to derive the optimal control law. The Hamiltonian (4.37) expressed as a piecewise function is

$$H = \begin{cases} \frac{P_d + P_0}{e} + \left(s\eta - \frac{1}{e} \right) P_m + s\beta\eta^2 P_m^2, & \text{if } P_m \leq 0 < P_d - P_m \\ \frac{P_d + P_0}{e} + \left(\frac{s}{\eta} - \frac{1}{e} \right) P_m + \frac{s\beta}{\eta^2} P_m^2, & \text{if } 0 \leq P_m < P_d \\ \frac{s}{\eta} P_m + \frac{s\beta}{\eta^2} P_m^2, & \text{if } P_m = P_d \geq 0 \\ s\eta P_m + s\beta\eta^2 P_m^2, & \text{if } P_m = P_d \leq 0 \end{cases} \quad (4.40)$$

The first interval $P_m \leq 0 < P_d - P_m$ indicates that the electric motor power is negative $P_m < 0$ and the engine power positive $P_e = P_d - P_m > 0$.

To simplify the explanations, the four parts of the Hamiltonian (4.40), together with the special case $P_m = 0 < P_d$, are defined as

$$H_{re} = \frac{P_d + P_0}{e} + \left(s\eta - \frac{1}{e} \right) P_m + s\beta\eta^2 P_m^2, \quad \text{for } P_m < 0 < P_d - P_m \quad (4.41a)$$

$$H_{th} = \frac{P_d + P_0}{e}, \quad \text{for } P_m = 0 < P_d \quad (4.41b)$$

$$H_{bo} = \frac{P_d + P_0}{e} + \left(\frac{s}{\eta} - \frac{1}{e} \right) P_m + \frac{s\beta}{\eta^2} P_m^2, \quad \text{for } 0 < P_m < P_d \quad (4.41c)$$

$$H_{el} = \frac{s}{\eta} P_m + \frac{s\beta}{\eta^2} P_m^2, \quad \text{for } P_m = P_d \geq 0, \quad (4.41d)$$

$$H_{el}^- = s\eta P_m + s\beta\eta^2 P_m^2, \quad \text{for } P_m = P_d \leq 0, \quad (4.41e)$$

where H_{re} is the Hamiltonian for recharging, H_{th} represents pure thermal operation, H_{bo} boosting, H_{el} pure electric propulsion, and H_{el}^- pure electric recuperation.

To find the control P_m that minimizes the Hamiltonian (4.40), the first and second derivatives of the Hamiltonian with respect to the control P_m are analyzed. Since the Hamiltonian is not differentiable at $P_m = 0$ and $P_m = P_d$, the derivatives are only analyzed for H_{re} and H_{bo}

$$\frac{\partial H_{re}}{\partial P_m} = \left(s\eta - \frac{1}{e} \right) + 2s\beta\eta^2 P_m, \quad \text{for } P_m < 0 < P_d - P_m \quad (4.42)$$

$$\frac{\partial H_{bo}}{\partial P_m} = \left(\frac{s}{\eta} - \frac{1}{e} \right) + 2\frac{s\beta}{\eta^2} P_m, \quad \text{for } 0 < P_m < P_d. \quad (4.43)$$

Since the parameters β and η are positive and s is assumed to be positive¹, the second derivatives of the Hamiltonians H_{re} and H_{bo} are positive

$$\frac{\partial^2 H_{re}}{\partial P_m^2} = 2s\beta\eta^2 > 0 \quad (4.44)$$

$$\frac{\partial^2 H_{bo}}{\partial P_m^2} = 2\frac{s\beta}{\eta^2} > 0. \quad (4.45)$$

To analyze the change in the derivative $\frac{\partial H}{\partial P_m}$ at the point $P_m = 0$ the limits of the first derivatives (4.42) and (4.43) are investigated. The limits when

¹A posteriori checking of the optimal solution will reveal that this assumption was valid.

P_m is approaching zero are

$$\lim_{P_m \rightarrow 0^-} \frac{\partial H_{re}}{\partial P_m} = s\eta - \frac{1}{e} \quad (4.46)$$

$$\lim_{P_m \rightarrow 0^+} \frac{\partial H_{bo}}{\partial P_m} = \frac{s}{\eta} - \frac{1}{e}, \quad (4.47)$$

where

$$\lim_{P_m \rightarrow 0^-} \frac{\partial H_{re}}{\partial P_m} < \lim_{P_m \rightarrow 0^+} \frac{\partial H_{bo}}{\partial P_m}. \quad (4.48)$$

Equation (4.48) is true for any s since $0 < \eta < 1$. Equation (4.48), together with the property of the second derivative (4.44)–(4.45), proves that

$$\frac{\partial H_{re}}{\partial P_m} < \frac{\partial H_{bo}}{\partial P_m}. \quad (4.49)$$

This property will be used in the following for the minimization of the Hamiltonian.

Minimization for $P_d > 0$

The minimum of the Hamiltonian can be found, depending on the value of s , in different intervals of the control P_m . A sketch of the Hamiltonian for all intervals of s is shown in Fig. 4.8. There is a discontinuity in the Hamiltonian at $P_m = P_d$. Hence, this control can be an optimal control candidate for all intervals in s .

The minimization of the Hamiltonian for its continuous part is carried out by analyzing its derivatives. If the limit of the derivative of H_{bo} (4.47) is negative, i.e. $s < \frac{\eta}{e}$, the optimum of the Hamiltonian is either in H_{bo} or in H_{el} . If the limit of the derivative of H_{re} (4.46) is positive, i.e. $s > \frac{1}{\eta e}$, the optimum of the Hamiltonian is either in H_{re} or in H_{el} . Finally, if the limit of the derivative of H_{bo} (4.47) is positive and the limit of the derivative of H_{re} (4.47) is negative, then the optimum is either in H_{th} or in H_{el} . These conclusions can be summarized as

$$\min_{P_m} H(P_m) = \begin{cases} \min\{H_{el}, H_{bo}\}, & \text{if } s < \frac{\eta}{e} \\ \min\{H_{el}, H_{th}\}, & \text{if } \frac{\eta}{e} \leq s \leq \frac{1}{\eta e} \\ \min\{H_{el}, H_{re}\}, & \text{if } s > \frac{1}{\eta e} \end{cases} \quad (4.50)$$

To find the control P_m that minimizes the Hamiltonian H_{bo} (4.41c), the

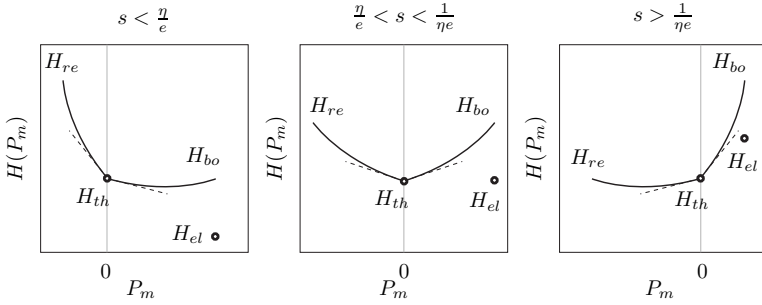


Figure 4.8: Schematic overview of the shape of the Hamiltonians H_{re} and H_{bo} for all intervals of s .

derivative (4.43) is set to zero and solved for P_m .

$$\frac{\partial H_{bo}}{\partial P_m} = \left(\frac{s}{\eta} - \frac{1}{e} \right) + 2 \frac{s\beta}{\eta^2} P_m = 0 \quad (4.51)$$

$$\Rightarrow P_m = P_m^{bo}(s) \triangleq \frac{\eta \left(\frac{\eta}{e} - s \right)}{2s\beta} \quad (4.52)$$

To find the control P_m that minimizes the Hamiltonian H_{re} (4.41a), the derivative (4.42) is set to zero and solved for P_m .

$$\frac{\partial H_{re}}{\partial P_m} = \left(s\eta - \frac{1}{e} \right) + 2s\beta\eta^2 P_m = 0 \quad (4.53)$$

$$\Rightarrow P_m = P_m^{re}(s) \triangleq -\frac{s - \frac{1}{\eta e}}{2s\beta\eta} \quad (4.54)$$

The candidates for the optimal control P_m^o corresponding to (4.50) are therefore

$$P_m^o \in \begin{cases} \{P_d, P_m^{bo}(s)\}, & \text{if } s < \frac{\eta}{e} \\ \{P_d, 0\}, & \text{if } \frac{\eta}{e} \leq s \leq \frac{1}{\eta e} \\ \{P_d, P_m^{re}(s)\}, & \text{if } s > \frac{1}{\eta e}. \end{cases} \quad (4.55)$$

The control that minimizes the Hamiltonian is determined by comparing the Hamiltonians in (4.50) when using the corresponding optimal control candidates in (4.55).

For $s < \frac{\eta}{e}$, only $H_{el}(P_d)$ and $H_{bo}(P_m^{bo}(s))$ can be optimal according to (4.50) and (4.55). Therefore, the condition for pure electric driving is

$H_{el}(P_d) < H_{bo}(P_m^{bo}(s))$. Solving this inequality for the power demand P_d yields the condition for pure electric driving, namely

$$P_d < P_{lim}^{bo}(s) \triangleq \frac{-\left(\frac{s}{\eta} - \frac{1}{e}\right) + \sqrt{4\frac{s\beta}{\eta^2} \frac{P_0}{e}}}{2\frac{s\beta}{\eta^2}}. \quad (4.56)$$

For $\frac{\eta}{e} \leq s \leq \frac{1}{\eta e}$, the condition $H_{el}(P_d) < H_{th}(0)$ yields as condition for pure electric driving

$$P_d < P_{lim}^{th}(s) \triangleq \frac{-\left(\frac{s}{\eta} - \frac{1}{e}\right) + \sqrt{\left(\frac{s}{\eta} - \frac{1}{e}\right)^2 + 4\frac{s\beta}{\eta^2} \frac{P_0}{e}}}{2\frac{s\beta}{\eta^2}}. \quad (4.57)$$

For $s > \frac{1}{\eta e}$, from $H_{el}(P_d) < H_{re}(P_m^{re}(s))$ it follows

$$P_d < P_{lim}^{re}(s) \triangleq \frac{-\left(\frac{s}{\eta} - \frac{1}{e}\right) + \sqrt{\left(\frac{s}{\eta} - \frac{1}{e}\right)^2 - \left(\frac{s}{\eta} - \frac{1}{e\eta^2}\right)^2 + 4\frac{s\beta}{\eta^2} \frac{P_0}{e}}}{2\frac{s\beta}{\eta^2}}. \quad (4.58)$$

It is interesting to note that for equality of the above conditions, i.e., $P_d = P_{lim}^{(\cdot)}$, the Hamiltonian has two identical minima. For a constant power demand, this would result in singular optimal control as investigated by [32]. The only charge-sustaining solution would be either pure thermal propulsion or duty cycling between pure electric and recharging. In reality, the power profile is never constant over the entire problem duration. Consequently, the optimal control for $P_d = P_{lim}^{(\cdot)}$ is chosen to be pure electric $P_m^o = P_d$ without loss of optimality.

Minimization for $P_d < 0$

When $P_d < 0$, both boosting H_{bo} and pure thermal driving H_{th} are not possible since $P_e \in [0, \infty)$. The Hamiltonian H_{re} given by (4.41a) is possible when $P_d - P_m > 0$. Equation (4.41a) remains the same when $P_d < 0$. However, the Hamiltonian for pure electric recuperation (4.41e) is different from the one of pure electric driving (4.41d). During braking phases ($P_d < 0$), the only candidates are therefore $H_{re}(P_m^{re}(s))$ and $H_{el}^-(P_d)$.

Pure electric recuperation is optimal if

$$H_{el}^-(P_d) < H_{re}(P_m^{re}(s)) \quad (4.59)$$

$$P_d < P_{lim}^{re-}(s) \triangleq \frac{-(s\eta - \frac{1}{e}) + \sqrt{4s\beta\eta^2 \frac{P_0}{e}}}{2s\beta\eta^2}. \quad (4.60)$$

4.3.2 Optimal Control with Input-Constrained and Speed-Dependent Model

The optimal control of the simplified model presented in Sec. 4.3.1 is being extended toward a more realistic model in this section. First, input constraints, i.e., power limits on the engine and the motor are being imposed. Second, the model is extended to a time-variant model, i.e., its parameters are speed-dependent.

Input-Constrained Model

The only constraint in the model thus far has been that the engine cannot provide any negative power. This single input constraint is not sufficient, however. The minimum and maximum power limits of the electric motor must be considered as well as the maximum power of the combustion engine. Hence, this section extends the optimal control law in presented Sec. 4.3.1 with the following power constraints:

$$P_e \in [0, P_{emax}] \quad (4.61a)$$

$$P_m \in [P_{mmin}, P_{mmax}]. \quad (4.61b)$$

As a consequence of these constraints, the power balance (4.30a) cannot always be fulfilled. For example, very high power demands that exceed the maximum power of engine and motor together, $P_d > P_{emax} + P_{mmax}$, are infeasible. Similarly, strongly negative power demands $P_d < P_{mmin}$ are infeasible for the powertrain. However, for such strong negative power demands, the remaining braking power is assumed to be absorbed by the conventional brakes such that $P_m = P_{mmin}$.

The control P_m can now be limited to P_{mmin} , P_{mmax} , or to $P_d - P_{emax}$ indirectly by the engine. Hence, the optimal control that minimizes the Hamiltonian is not only a function of s , but also of the constraints being active. The power limits shown in Fig. 4.5 that separate the different operating modes are now extended with additional limits due to the

constraints. Figure 4.9 shows an example of the new power limits for a powertrain with the parameters listed in Table 4.4 and Table 4.5. Note that this is only an example and that there will be other active power limits if the parameters change. Figure 4.9 shows that the number of power limits and the number of regions with different operating modes have increased. The power limits that are added to the previous limits (4.35) are $P_{emax} + P_m^{bo}(s)$, P_{emax} , $P_{emax} + P_m^{re}(s)$, $P_{emax} + P_{mmin}$, P_{mmax} , P_{mmin} , $P_{lim}^{re,m}(s)$, and $P_{lim}^{re,m-}(s)$. These power limits are derived analogously to the limits (4.35). The regions in Fig. 4.9 are also separated by the two new equivalence factor limits $s_{lim}^{bo,m}$ and $s_{lim}^{re,m}$. The equations for the power limits $P_{lim}^{re,m}(s)$ and $P_{lim}^{re,m-}(s)$ are given in the Appendix by (C.6) and (C.9) respectively. The equations for the equivalence factor limits $s_{lim}^{bo,m}$ and $s_{lim}^{re,m}$ are given in the Appendix by (C.2) and (C.4). These equations are explained further in Appendix C.

Table 4.5: Power limits of the powertrain.

Parameter	Value	Unit
P_{emax}	$75 \cdot 10^3$	W
P_{mmax}	$25 \cdot 10^3$	W
P_{mmin}	$-25 \cdot 10^3$	W

All new power limits that result from including the constraints on the engine and motor must be calculated for determining the optimal control at the actual operating condition. Therefore, the computational effort for determining the optimal control P_m^o from the equivalence factor s and the current power demand P_d has increased.

A more efficient way of determining the optimal control P_m^o is to, as described in [11], evaluate the Hamiltonian (4.40) for the possible optimal control candidates given by

$$\mathcal{P}(P_d, s) = \{0, P_d, P_m^{bo}(s), P_m^{re}(s), P_{mmax}, P_{mmin}, P_d - P_{emax}\}. \quad (4.62)$$

The optimal control is then determined by evaluating the Hamiltonian for the control candidates in (4.62) and selecting the control that yields the minimum. This selective minimization of the Hamiltonian must respect

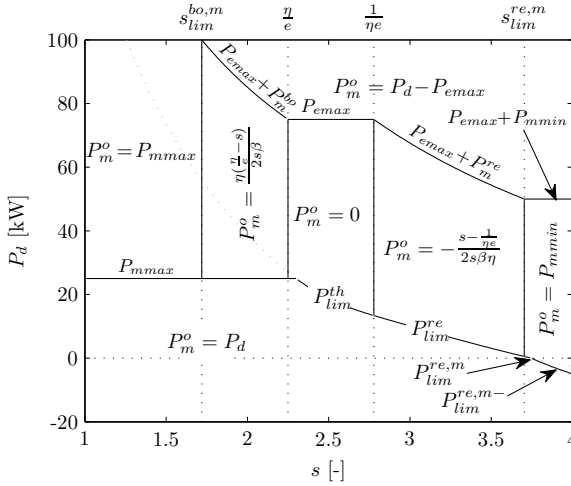


Figure 4.9: Overview of the regions with the different optimal control P_m^o (separated by solid lines) and the power limits $P_{lim}^{(\cdot)}$ for the constrained problem.

the constraints (4.61a) and (4.61b), as well as the power balance (4.30a)

$$P_m^o(P_d, s) = \underset{P_m \in \mathcal{P}(P_d, s)}{\operatorname{argmin}} H(P_m, P_d, s) \quad (4.63a)$$

s.t.

$$P_e = P_d - P_m \quad (4.63b)$$

$$P_m \in [P_{mmin}, P_{mmax}] \quad (4.63c)$$

$$P_e \in [0, P_{emax}]. \quad (4.63d)$$

The method of selectively minimizing the Hamiltonian for the optimal control candidates is referred to as selective Hamiltonian minimization (SHM), here. Note that, for many operating conditions, a careful implementation of the SHM can utilize the constraints (4.63b)–(4.63d) in order to minimize the feasible candidates in $\mathcal{P}(s)$. It is therefore possible to reduce the computational effort to perform the minimization (4.63a).

Example on a Driving Cycle

When the power constraints in the engine and motor are included, the method of finding the charge-sustaining equivalence factor is the same as in

Sec. 4.3.1, i.e., a root finding algorithm is used. Note that the initial guess of the algorithm must be larger than $s_{lim}^{bo,m}$ since below this equivalence factor the operating modes do not change and the final energy in the battery is constant. The charge-sustaining equivalence factor for CADC is slightly different when including the constraints $s_{cs} = 2.8463$ compared to the unconstrained case $s_{cs} = 2.8399$ because of the new regions shown in Fig. 4.9.

Figure 4.10 shows a section of the optimal charge-sustaining control for the CADC where four different modes can be observed. These modes are recharging $P_m = -2409.0$ W, electric driving and recuperation $P_m = P_d$, maximum recuperation $P_m = P_{mmin}$, and boosting or recharging limited by the engine $P_m = P_d - P_{emax}$. This figure clearly shows that the different operating modes are separated by power limits (top graph) and not by speed limits (bottom graph).

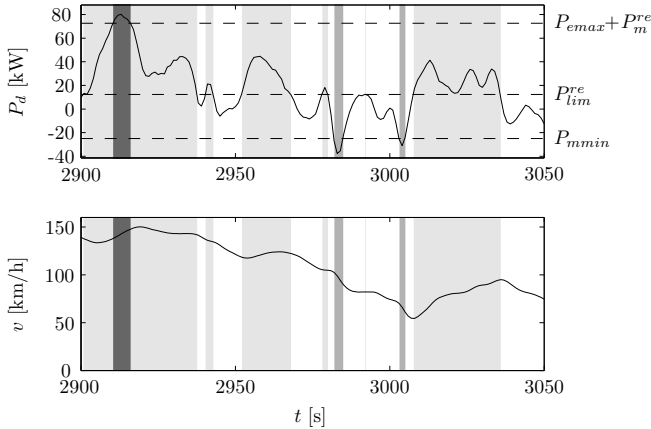


Figure 4.10: Power and speed profile $P_d(t)$ and $v(t)$ of CADC on the interval $t \in [2900, 3050]$ with the optimal control. Light gray indicates recharging mode ($P_m = -2409.0$ W), medium gray indicates maximum recuperation ($P_m = P_{mmin}$), dark gray indicates boosting or recharging limited by engine ($P_m = P_d - P_{emax}$), and white indicates electric mode ($P_m = P_d$).

Input-Constrained, Speed-Dependent Model

The model described in Sec. 4.3.2 does not depend on the rotational speed of the crankshaft. In reality, however, several component param-

eters are speed-dependent. This section investigates a modified version of the model given by equations (4.30) including the input constraints (4.61a) and (4.61b), where e , P_0 , and P_{emax} are replaced by $e(\omega)$, $P_0(\omega)$, and $P_{emax}(\omega)$, respectively.

In the electric path, only the parameters of the electric motor are speed-dependent, strictly speaking. This would result in the parameters $\eta(\omega)$, $P_{mmax}(\omega)$, and $P_{mmin}(\omega)$. The battery characteristics are indeed not speed-dependent. However, the parameter β , which captures nonlinearities in the battery, can also be used to capture the nonlinearities in the electric motor. Consequently, the entire electric path is integrated in the parameters $\eta(\omega)$, $\beta(\omega)$, $P_{mmax}(\omega)$, and $P_{mmin}(\omega)$.

The speed-dependent model is finally obtained by fitting the parameters of the simplified, speed-independent model to measured data for a set of rotational speeds. The following data of a real powertrain are typically available to fit the speed-dependent model:

- A stationary fuel consumption map of the engine as a function of the rotational speed and the torque,
- the maximum torque curve of the engine,
- the idle speed of the engine,
- a stationary electric consumption map of the motor as a function of the rotational speed and the torque,
- the maximum and minimum torque lines of the motor,
- the open-circuit voltage and the inner resistance curves for charging and discharging of the battery as a function of the state-of-charge.

Original Model

In order to evaluate the simplified model introduced in Sec. 4.3.2 using speed-dependent parameters versus the real powertrain, the more detailed model presented in Chapter 2 is used. Since at this stage measurements of a lithium-ion battery are available, these data are used here. The open-circuit voltage and the inner resistance for charging and discharging of this battery pack are shown in Fig.4.11, its capacity is $Q_0 = 6.2$ Ah. This more detailed model with the Li-ion battery is referred to as the *original model*

in the following. This original model relies on measured data, namely the consumption maps and the maximum torque lines of the engine and the electric motor, and the characteristics of the battery given by the open-circuit voltage and the inner resistance over the state-of-charge.

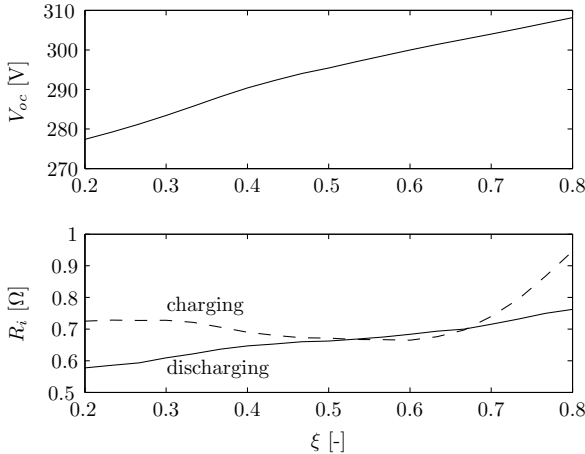


Figure 4.11: Measured characteristics of the Li-ion battery pack. The top graph shows the open-circuit voltage and the bottom graph shows the inner resistance for charging and discharging.

Fitting of Speed-Dependent Parameters

The speed-dependent parameters of the simplified model are evaluated for each rotational speed such that the sum of the absolute errors between the simplified model and the original model is minimized. Such a fit is shown in Fig. 4.12 for $\omega = 1000$ rpm and $\omega = 3000$ rpm. It clearly shows that the engine can be well approximated with an affine function and that the electric path is well described by a piecewise quadratic function.

The resulting speed-dependent parameters for the simplified model are shown in Fig. 4.13, while the corresponding efficiency maps are shown in Figs. 4.14 and 4.15. The peak efficiency in Fig. 4.14 is very high for an SI engine. This is a consequence of the affine approximation that tends to underestimate the fuel consumption at high loads due to enrichment.

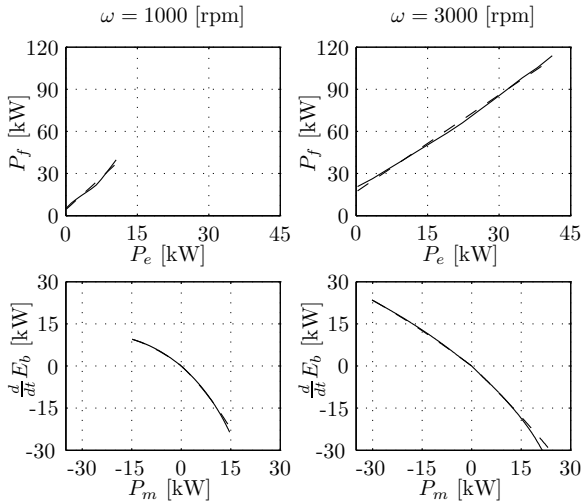


Figure 4.12: Characteristics of the engine (top) and the electric path (bottom) for two selected speeds for the original model (solid) and the fitted simplified model (dashed).

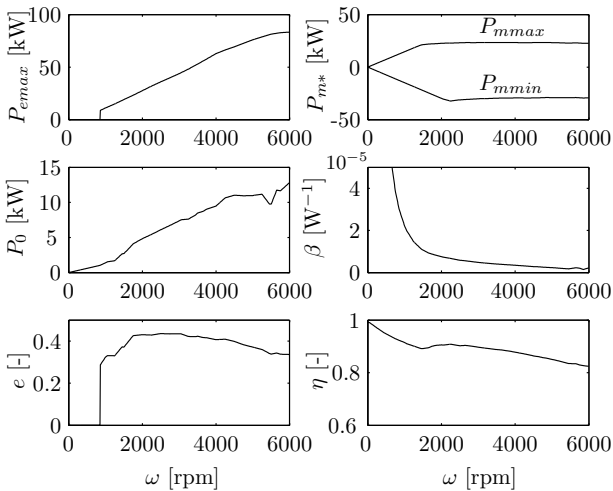


Figure 4.13: Parameters of the simplified, speed-dependent model of the parallel propulsion system.

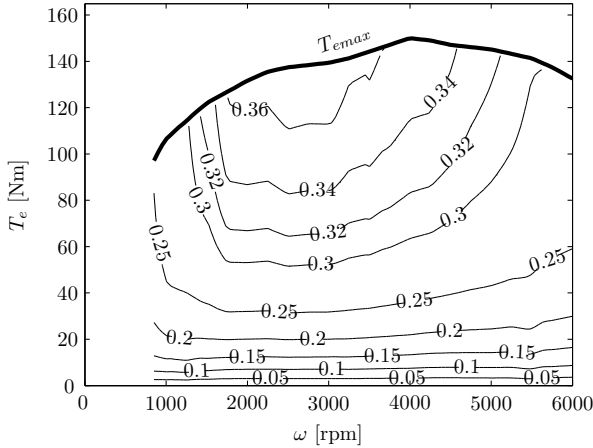


Figure 4.14: Engine map of the simplified, speed-dependent model with iso-efficiency and peak torque lines.

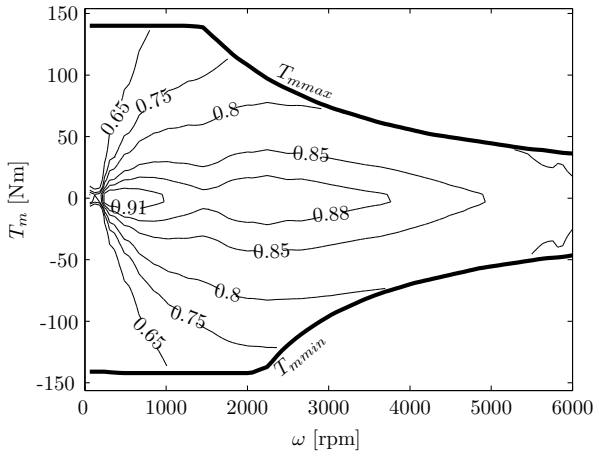


Figure 4.15: Efficiency map of the electric path of the simplified, speed-dependent model. The efficiency includes electric motor and battery.

Optimal Control

Using the speed-dependent model, the derivation and the solution of the optimal control problem stated in (4.30)–(4.34) do not change from those

using the speed-independent model above. The optimal control policy given in (4.63a) is still optimal when speed-dependent parameters are used. However, the power limits are now dependent on the rotational speed and thus the different regions shown in Fig. 4.9 vary with the rotational speed. Therefore, the regions defining the optimal control increase by one dimension, namely the speed ω . Figure 4.16 shows the regions for the charge-sustaining equivalence factor for CADC. In order to improve readability, this figure is expressed with torque values instead of power.

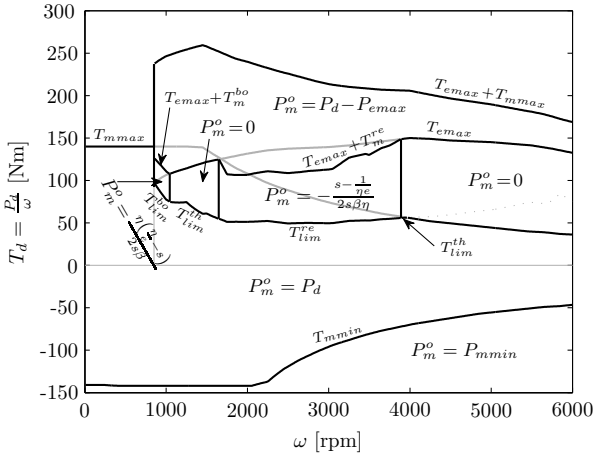


Figure 4.16: Overview of the regions with the different optimal control P_m^o (separated by solid lines) for the constrained, speed-dependent problem. The regions are represented for the charge-sustaining equivalence factor s_{cs} for CADC as a function of gearbox speed ω and torque T_d .

4.3.3 Model Validation

In this section, the simplified model (4.30) with the speed-dependent parameters shown in Fig. 4.13 and the constraints (4.61) is validated by the original model in Sec. 4.3.2. The validation is carried out by application of a feedforward control signal to both models. Both the state trajectory $E_b(t)$ and the cost functional $E_f(t)$ are being compared for three driving cycles. The driving cycles used in this section are the CADC, the NEDC, and the FTP-72 as shown in Appendix B. The feedforward signal ap-

plied here is the charge-sustaining optimal control signal evaluated for the simplified model. The charge-sustaining optimal control for the CADC is shown in Fig. 4.16. Figure 4.17 shows the state trajectory $E_b(t)$ and

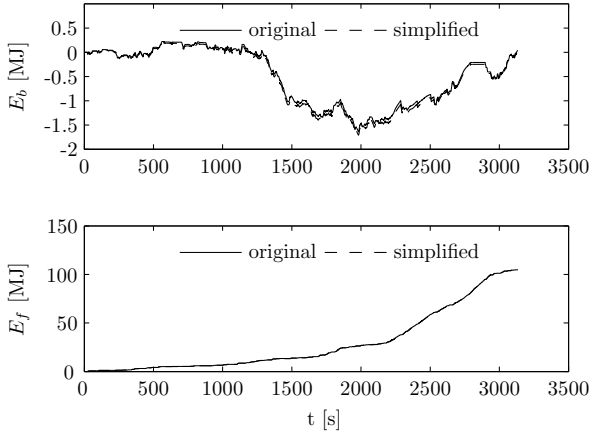


Figure 4.17: Signals for the simplified and original models when using the optimal control determined using the simplified model for the CADC. The upper graph shows the state trajectory E_b , while the lower graph shows the fuel energy E_f .

the cost functional $E_f(t)$ of both models for the CADC. Note that the models are actuated with the same signal. Both trajectories match very well and justify the simplifications adopted when the simplified model was formulated from the original model.

The relative deviations of the two models for both signals at the final time t_f are defined as

$$\epsilon_{ff,E_b} = \frac{E_{b,orig}(t_f) - E_{b,simp}(t_f)}{\int_0^{t_f} |\dot{E}_{b,orig}(\tau)| d\tau} \quad (4.64)$$

$$\epsilon_{ff,E_f} = \frac{E_{f,orig}(t_f) - E_{f,simp}(t_f)}{E_{f,orig}(t_f)}. \quad (4.65)$$

Table 4.6 shows that the final energy content of the battery $E_b(t_f)$ as well as the final fuel energy use $E_f(t_f)$ of the simplified model fit the original model well. The largest error, i.e., the error in the final energy content ϵ_{ff,E_b} for NEDC, is 1.6%.

Note that the error in the final state ϵ_{ff,E_b} cannot be separated from the error in the cost functional ϵ_{ff,E_f} since a surplus in final battery energy $E_b(t_f)$ could have been used to lower the fuel energy $E_f(t_f)$. Therefore, in order to compare the error in fuel consumption only, the two simulations carried out must have identical initial and final battery energy levels. This is achieved by first obtaining the fuel consumption by simulating the original model with the feedforward $P_{m,simp}^o$ derived for the simplified model. This fuel consumption is then compared to the optimal fuel consumption having identical initial and final battery energy levels. The optimal fuel consumption for the original model is found by means of dynamic programming [13, 14]. The dynamic programming algorithm has been implemented using the ideas introduced in Chapter 3 and [20, 21]. The difference in fuel consumption between these two simulations reveals the losses introduced by using a simplified model for the evaluation of the control. This increase in fuel consumption is expressed by the relative excess consumption rEC as introduced by (4.10) in Sec. 4.1.3

$$rEC_{ff} = \frac{E_{f,orig}^{ff,simp}(t_f) - E_{f,orig}^{dp}(t_f)}{E_{f,orig}^{dp}(t_f)}. \quad (4.66)$$

These increases in fuel consumption are shown in Table 4.7. Note that the simplified model is state independent while in the original model the battery is dependent on the state. A large deviation of the state will therefore increase the error between the models. Part of the relative excess consumption rEC_{ff} in Table 4.7 is a consequence of the relatively large state deviations $E_b(t)$ when applying $P_{m,orig}^o$. The solution from dynamic programming accounts for the state dependencies of the original model and reduces the state deviation.

Table 4.6: Validation of the simplified model versus the original model.

Variable	CADC	NEDC	FTP-72
ϵ_{ff,E_b}	0.2%	1.6%	1.1%
ϵ_{ff,E_f}	0.2%	0.7%	1.0%

Table 4.7: Increased fuel consumption due to simplified model for control.

Variable	CADC	NEDC	FTP-72
rEC_{ff}	0.8%	1.2%	1.5%

4.3.4 Application of Simplified Model

The simplified, speed-dependent model which was validated in Sec. 4.3.3 can be used for energy management in a real vehicle. The control of the powertrain at each time sample is then evaluated by the following algorithm:

1. Read the requested power P_d and the actual speed ω .
2. Evaluate the speed-dependent parameters for the rotational speed ω .
3. For a given s , evaluate the control P_m^o that minimizes the Hamiltonian according to (4.63a).
4. Apply P_m^o to the electric motor and $P_d - P_m^o$ to the engine.

The constant equivalence factor must be found such that charge sustenance is achieved for the given driving cycle as described in Sec. 4.3.1. Such a controller cannot be realized because it relies on future information, i.e., it is non-causal. However, suboptimal approaches can be taken to render the control causal.

Causal Feedback Control

The causal feedback control used here is identical to the one presented in Sec. 4.2.2. It evaluates the equivalence factor s such that the state-of-charge ξ is controlled. The feedback law is given by (4.24b) with the values given in Table 4.2 together with the battery capacity $Q_0 = 6.2$ Ah, the open-circuit voltage $V_{oc}(\xi = 0.6) = 300$ V, and the reference state-of-charge $\xi_{ref} = 0.6$.

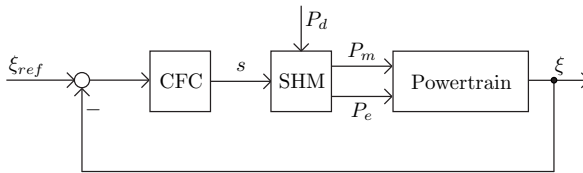


Figure 4.18: Schematic of the control loop.

Anti-Windup

The causal feedback control (CFC) given by (4.24b) contains an integral part to avoid static errors. This integral part can lead to undesired behavior, called *wind-up* of the integrator, if the controller output is saturated [33]. The controller for this consideration is only the function (4.24b) with $\xi_{ref} - \xi(t)$ being the controller input and $s(t)$ being the controller output as schematically shown in Fig. 4.18. For equivalence factors s being less than $s_{lim}^{bo,m}$ (C.2), the control of the powertrain is independent of the equivalence factor as it can be seen in Fig. 4.9. Hence, the controller output $s(t)$ is saturated for $s < s_{lim}^{bo,m}$. For very high values of $s(t)$, such a saturation does not occur because the power limit $P_{lim}^{re,m-}$ converges for $s \rightarrow \infty$ to the minimum power limit of the motor P_{mmin} . This means that for $s > s_{lim}^{re,m}$, there is always more recharging of the battery for larger values of s . Consequently, an anti-windup scheme is implemented with a saturation of $s(t) \in [s_{sub}, \infty)$, where

$$s_{sub} = \min_{\omega} s_{lim}^{bo,m}(\omega) \quad (4.67)$$

$$= \min_{\omega} \frac{\eta(\omega)^2}{e(\omega)(2P_{mmax}(\omega)\beta(\omega) + \eta(\omega))}. \quad (4.68)$$

Example on a Driving Cycle

The causal controller relying on the simplified model is finally applied on the original model. To benchmark its performance, the optimal solution having the same initial and final conditions as the causal controller $E_{b,orig}^{fb,simp}(t_f) = E_{b,orig}^{dp}(t_f)$ is found using dynamic programming. The relative excess fuel consumption is expressed by

$$rEC_{fb} = \frac{E_{f,orig}^{fb,simp}(t_f) - E_{f,orig}^{dp}(t_f)}{E_{f,orig}^{dp}(t_f)} \quad (4.69)$$

and is shown in Table 4.8.

The state trajectories resulting from applying the simplified model for causal control of the original model are shown in Fig. 4.19 for the CADC. The figure also shows the optimal state trajectory determined using dynamic programming.

The sub-optimality of the control can be explained by two effects. First, the model used to evaluate the control is simplified, i.e., it does not perfectly represent the real plant. This effect is investigated in Sec. 4.3.3.

Second, the causal controller cannot take into account any future information on the driving cycle. In contrast, the optimal solution from dynamic programming fully exploits information on the driving cycle.

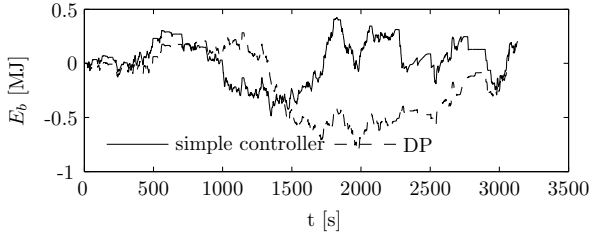


Figure 4.19: State trajectory resulting from applying the simplified model for causal control of the original model (solid), and the state trajectory using DP on the original model (dashed) for CADC.

Table 4.8: Relative fuel excess consumption using the simplified model for control of original model.

Variable	CADC	NEDC	FTP-72
rEC_{fb}	1.1%	1.7%	1.7%

However, the causal controller given by (4.24b), (4.62), and (4.63) with the speed-dependent parameters shown in Fig. 4.13 is computationally cheap and simple to implement. The controller also achieves results which are within 1.7% from the global optimum for three driving cycles.

4.3.5 Conclusions for the Simplified Model

In this section, the explicit solution to the optimal control problem of a simplified speed-independent unconstrained hybrid electric powertrain has been derived and studied. The solution to the optimal control problem shows how simple power limits determine the optimal operating mode for the hybrid powertrain. In contrast to many rule-based controllers which use a speed threshold between electric and thermal/recharge mode, this study shows that the solution of the optimal control problem yields a power threshold.

The unconstrained problem has been extended to the case where the electric motor and combustion engine have power constraints. The derivation of the optimal control is similar to the unconstrained case. However, there are several additional power limits deciding the optimal control.

The speed-independent, constrained model has been further extended to a speed-dependent model. The powertrain parameters were fitted to measured data. The explicit solution to the problem can still be determined with several additional power limits. The charge-sustaining optimal control map is shown for the CADC in terms of torque demand and rotational speed. It shows that the optimal control can be expressed as a simple rule-based map where all regions are defined by model parameters. However, a computationally cheaper method is proposed where the Hamiltonian is selectively minimized for a set of explicit optimal control candidates. The benefit of this formulation is the simple structure and the low number of possible minima.

The model has been validated using the original model that relies on measured data. A comparison of the signals of the original and the simplified model by applying a feedforward signal has been carried out. It shows a maximum error of 1.6% in the final state and 1.0% in the final cost for three commonly used driving cycles. Despite the broad simplifications the model captures the most important characteristics of the original hybrid powertrain.

The simplified model is used in a causal energy management strategy, where the equivalence factor is updated by a causal controller. When using the simplified model for causal control the fuel consumption is within 1.7% from the global optimum for three driving cycles. The simplicity and the high performance in fuel economy prove that the proposed strategy is well suited for real-time control of parallel hybrid electric powertrains.

The formulation of the simplified model further allowed to analytically derive a saturation in the equivalence factor that can be used to implement an anti-windup scheme in a causal equivalence factor controller.

Chapter 5

Predictive Control for the State-of-Charge

It was indicated in Sec. 4.2 and [12] that a non-predictive strategy performs poorly in the presence of constraints on the battery's state-of-charge if the amount of recuperated energy is large compared to the storage capacity of the battery. This is due to the fact that there will be future recuperation phases during which the controller has no action on the state. If such phases occur and the strategy is non-predictive, it is likely that the state runs into its constraints. Hence, only a predictive strategy can prevent this.

Therefore, a predictive strategy is introduced in this chapter. Many predictive approaches have been presented in literature as for example [9, 23]. However, most of these approaches assume that the future driving profile is known at a high accuracy. In contrast, the approach presented here requires only the current state of the powertrain and data available from navigation systems, such as the average traveling speed on the future road segments and the corresponding elevation profile. These data are available from standard navigation systems if these devices are extended with topographic maps. To evaluate these data, the destination of the trip has to be known by the navigation system. Typically, the driver specifies the destination. If the driver plans a trip he often took in the past, he typically does not specify a destination. For these cases, an algorithm can be used to detect the planned trip out of a set of previously driven trips. Such an algorithm has been successfully developed and tested by [34].

This predictive strategy uses an algorithm that generates a time-varying trajectory $\xi_{ref}(t)$ for the reference of the state-of-charge to avoid the events where the battery's state-of-charge runs into its constraints due to recuper-

ation. This algorithm is referred to as predictive reference signal generator (pRSG), here. This predictive reference signal generator exploits all available information of the future driving profile and respects the state constraints on the battery's SoC. The underlying algorithm is computationally very attractive, since the problem could be formulated as a quadratic program (QP). Figure 5.1 illustrates schematically the extension of the existing ECMS with the pRSG.

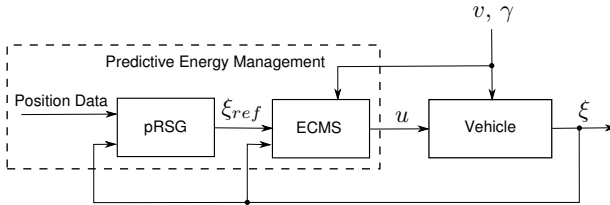


Figure 5.1: Block diagram of the pRSG-ECMS control system.

5.1 Method

The operation of an HEV can be categorized into two main types of operation. The first type of operation consists of all operations where the supervisory control can explicitly control the SoC by favoring or penalizing the use of the electric path. The time intervals during which the supervisory control is using this type of operation are referred to as *free* segments in the following. The second type of operation consists of all operations where the supervisory control cannot explicitly control the SoC. This is typically the case when the powertrain is either in boosting ($T_{GB} > T_{ICE,max}$) or in recuperation mode ($T_{GB} < 0$); the use of the electric path is determined purely by the driver/cycle. These time intervals are referred to as *fixed* segments. Since the SoC cannot be explicitly controlled during fixed segments, it can happen that the SoC violates its constraints as discussed in the previous section. If this happens during a recuperation phase, some of the available recuperable energy must be wasted in the conventional brakes in order to respect the upper SoC constraint. Therefore, the ECMS needs to be extended in order to assure that information on the future driving profile is used to prevent such energy wasting events. This objective is achieved by computing a time-varying reference trajectory for the SoC.

In a first step, the future fixed segments are identified from data of the navigation system. With this information the future recuperable energies of the fixed segments are estimated and converted into future SoC changes. This is presented in Sec. 5.1.1.

In a second step, the SoC reference trajectory is synthesized on the basis of that information. The reference trajectory is assumed to be a piecewise affine function of time, where each affine segment corresponds to a free or a fixed segment. The parameters of the piecewise affine SoC reference trajectory are computed such that the SoC constraints of the battery are not violated. The necessary computations can be formulated as a quadratic program, which is solved very efficiently. The precise formulation of this optimization is presented in Sec. 5.1.2.

5.1.1 Prediction of Recuperation Time Segments

In order to predict the time segments where recuperation takes place, only information provided by the navigation system is used, namely the topographic profile (5.1) and the average traveling speed on each road segment (5.2) between the actual position and the destination. These data points are specified at the discrete distances $d_{h,m}$ and $d_{v,n}$, respectively.

$$h_m = h(d_{h,m}) \quad (5.1)$$

$$\bar{v}_n = \bar{v}(d_{v,n}) \quad (5.2)$$

The two sets of data, represented in Fig. 5.2 (top and center graphs), are mapped to a common grid d_i (5.3) as illustrated by the dashed vertical lines. As a result, each road segment with length Δd_i is characterized by its grade γ_i and its average speed \bar{v}_i .

$$d_i = d_{h,m} \cup d_{v,n} \quad (5.3)$$

The estimated force acting on the vehicle over the segment i is given by

$$\bar{F}_{unlim,i} = \frac{1}{2} \rho A_f c_d \bar{v}_i^2 + c_r m_v g \cos \gamma_i + m_v g \sin \gamma_i, \quad (5.4)$$

where ρ is the air density, A_f is the frontal area of the vehicle, c_d is the aerodynamic drag coefficient, c_r is the rolling friction coefficient, m_v is the vehicle mass, and g is the gravitational acceleration.

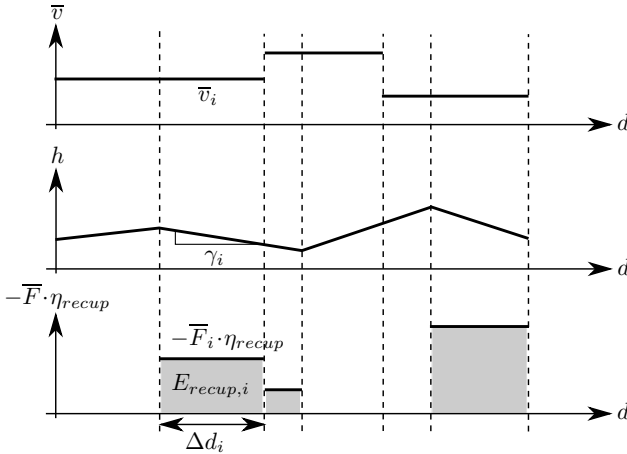


Figure 5.2: Data from the navigation system mapped to a common grid (top and center graphs) with the estimated recuperation force and the resulting recuperated energy due to elevation changes (bottom graph).

During recuperation, high electric power flows can occur. These power flows can exceed the limitation $P_{el,min} (< 0)$ of the electric path that includes the electric motor, the power converter, and the battery. Therefore, the (negative) force is limited by

$$\bar{F}_i = \max \left\{ \bar{F}_{unlim,i}, \frac{P_{el,min}}{\bar{v}_i \cdot \eta_{recup}} \right\}. \quad (5.5)$$

The efficiency η_{recup} of the electric path during a recuperation phase is assumed to be constant. It accounts for all of the losses from the wheels to the battery. The assumption of a constant η_{recup} could be relaxed easily by accounting for the operating-point dependent efficiencies of all components. Such an expansion would, however, not change the main results of this work.

Figure 5.2 (bottom graph) illustrates the average force corrected with the recuperation efficiency for each road segment. The resulting estimated amount of potential energy that is recuperated over each interval i , indicated in this figure by the grey area, is given by

$$E_{recup,i} = \begin{cases} -\bar{F}_i \cdot \Delta d_i \cdot \eta_{recup}, & \text{if } \bar{F}_i < 0 \\ 0, & \text{else.} \end{cases} \quad (5.6)$$

In order to derive the SoC reference trajectory, the recuperated energies $E_{recup,i}$ are converted to the equivalent SoC changes $\Delta\tilde{\xi}_i$ using (5.7). The superscript $\tilde{\cdot}$ is used in the following to denote variables of the fixed segments. For this conversion, the SoC is assumed to be near a given set-point ξ_{set} . This assumption is made because the SoC level at which each recuperation will occur is unknown at this stage. The corresponding distances Δd_i are converted to time intervals using (5.8).

$$\Delta\tilde{\xi}_i = \frac{E_{recup,i}}{Q_0 V_{oc}(\xi_{set})} \quad (5.7)$$

$$\Delta\tilde{t}_i = \frac{\Delta d_i}{\bar{v}_i} \quad (5.8)$$

To reduce the computational burden caused by generating the SoC reference trajectory, at each time step all successive segments of recuperation are lumped into one segment of recuperation. Each of these N aggregated recuperation segments is then saved as a triple \tilde{R}_i containing its (future) starting time, its duration, and the SoC change that is expected

$$\tilde{R}_i = \{\tilde{t}_i, \Delta\tilde{t}_i, \Delta\tilde{\xi}_i\}. \quad (5.9)$$

5.1.2 Synthesis of an SoC Reference Trajectory

The data about future expected recuperation segments \tilde{R}_i is used to synthesize a reference trajectory for the SoC. As illustrated in Fig. 5.3, the problem that has to be solved is to find a piecewise-affine reference trajectory for the SoC that never violates the SoC boundaries. This trajectory consists of the fixed segments in which recuperation takes place and of the free segments that lie between two fixed segments. The fixed segments are known by their (future) starting time \tilde{t}_i , their duration $\Delta\tilde{t}_i$, and their change in SoC $\Delta\tilde{\xi}_i$. If the value of the SoC at each start of a fixed segment $\tilde{\xi}_i$ is defined, the entire reference trajectory is determined. Hence, the SoC values $\tilde{\xi}_i$ are the unknowns that have to be found in order to be able to synthesize the SoC reference trajectory.

The reference trajectory ξ_{ref} must:

- remain within the interval $\Omega = [\xi_{ref,min}, \xi_{ref,max}]$ at all times;
- keep the final SoC of the reference trajectory within a target interval $\Omega_f = [\xi_{set} - \delta\xi_f, \xi_{set} + \delta\xi_f]$; and

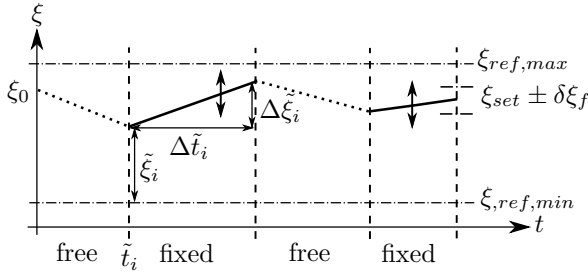


Figure 5.3: Synthesis of the reference SoC trajectory by varying the initial condition $\tilde{\xi}_i$ for each recuperation phase.

- minimize the rate of change of the SoC during the free elements of the reference trajectory.

The last point is a choice that is made to extend the lifetime of the battery. In fact, minimizing the rate of change corresponds to minimizing the currents drawn from the battery, which is known to be beneficial for batteries [35].

Assumptions

The following problem formulation is based on the assumptions that

- the fixed segments correspond to recuperation phases only, i.e. $\Delta\tilde{\xi}_i > 0 \forall i = 1, \dots, N$;
- the reference trajectory starts in a free segment;
- fixed and free segments are alternating; and
- the final segment is a fixed segment.

The assumption that the fixed segments consist only of recuperation phases is made because boosting phases in general are very short and are, therefore, considered as disturbances. This assumption is not strictly necessary, but it reduces considerably the number of linear inequality constraints in the quadratic program formulated below. The assumption that the reference trajectory starts on a free segment is not restricting. If the vehicle is in a fixed segment when the optimization is started, the reference signal up to the end of this segment is already fixed. Hence, the problem can be

formulated to begin at the end of this first segment. The assumption that fixed and free segments are alternating is a consequence of the aggregation of the recuperation phases as discussed in Sec. 5.1.1. The last point simply reflects the assumption that the vehicle will be brought to standstill at the end of each trip.

Problem Formulation

The objectives mentioned above can now be rephrased mathematically as follows:

- The SoC must be in the set Ω (lower bound, upper bound) and the final SoC (lower final state, upper final state) must be in the set Ω_f

$$\tilde{\xi}_i \geq \xi_{ref,min} - \varepsilon_i \quad (5.10a)$$

$$\tilde{\xi}_i + \Delta\tilde{\xi}_i \leq \xi_{ref,max} + \varepsilon_i \quad (5.10b)$$

$$\tilde{\xi}_N + \Delta\tilde{\xi}_N \geq \xi_{set} - \delta\xi_f - \varepsilon_f \quad (5.10c)$$

$$\tilde{\xi}_N + \Delta\tilde{\xi}_N \leq \xi_{set} + \delta\xi_f + \varepsilon_f, \quad (5.10d)$$

where ε_i and ε_f are slackness variables that are introduced to guarantee the feasibility by softening the state constraints. Equation (5.10a) has to be fulfilled for all $i = 1, \dots, N$. The assumption that $\xi_{set} + \delta\xi_f < \xi_{ref,max}$ implies that (5.10b) has to be fulfilled only for all $i = 1, \dots, N - 1$. For $i = N$, (5.10b) is always fulfilled when (5.10d) is fulfilled. Summarizing, there are $2N + 1$ inequalities that must be satisfied.

- The minimization of the slopes of the free segments and the penalties on the slackness variables are expressed by

$$\min_z \left\{ \alpha_{\varepsilon,f} \cdot \varepsilon_f^2 + \sum_{i=1}^N \left(\frac{\Delta\hat{\xi}_i^2}{\Delta\hat{t}_i^2} + \alpha_\varepsilon \cdot \varepsilon_i^2 \right) \right\}, \quad (5.11a)$$

where

$$\Delta\hat{\xi}_i = \tilde{\xi}_i - (\tilde{\xi}_{i-1} + \Delta\tilde{\xi}_{i-1}) \quad (5.11b)$$

$$\Delta\tilde{\xi}_0 = 0 \quad (5.11c)$$

$$\Delta\hat{t}_i = \tilde{t}_i - (\tilde{t}_{i-1} + \Delta\tilde{t}_{i-1}) \quad (5.11d)$$

$$\tilde{t}_0 = 0 \quad (5.11e)$$

$$\Delta\tilde{t}_0 = 0. \quad (5.11f)$$

The superscript $\hat{\cdot}$ denotes variables of the free segments.

The unknown vector z of length $2N + 1$ is given by

$$z = [\tilde{\xi}_1, \dots, \tilde{\xi}_N, \varepsilon_1, \dots, \varepsilon_N, \varepsilon_f]^T, \quad (5.11g)$$

where $\tilde{\xi}_i$ represent the SoC at the beginning of each i -th fixed segment. The slackness variables are penalized using the positive weights α_ε and $\alpha_{\varepsilon,f}$, respectively.

The problem defined by (5.10) and (5.11) can be formulated as a standard QP

$$\begin{aligned} \min_z \quad & z^T Q z + p^T z \\ \text{s.t.} \quad & A z \leq b. \end{aligned} \quad (5.12)$$

The matrices Q , p , A , and b can be derived from (5.10) and (5.11) and are listed in Appendix D. The matrix Q is tridiagonal, and all elements of the main diagonal are strictly positive. Furthermore, the other two diagonals contain some zeros each. With these properties, the matrix Q is positive-definite. Consequently, the QP (5.12) is convex and can be solved in polynomial time.

Synthesis of the Reference Trajectory

The desired SoC reference trajectory $\xi_j(t_j)$ is now determined by the first N elements $\tilde{\xi}_i$ of the solution z of the QP, by the starting SoC value ξ_0 , and by the SoC changes $\Delta\tilde{\xi}_i$. This is shown in (5.13).

$$\xi_j = \begin{cases} \xi_0, & \text{if } j = 1 \\ \tilde{\xi}_i, & \text{if } j = 2i, i = 1, \dots, N \\ \tilde{\xi}_i + \Delta\tilde{\xi}_i, & \text{if } j = 2i + 1, i = 1, \dots, N \end{cases} \quad (5.13a)$$

$$t_j = \begin{cases} 0, & \text{if } j = 1 \\ \tilde{t}_i, & \text{if } j = 2i, i = 1, \dots, N \\ \tilde{t}_i + \Delta\tilde{t}_i, & \text{if } j = 2i + 1, i = 1, \dots, N \end{cases} \quad (5.13b)$$

Since the SoC reference trajectory is calculated from data on the aggregated time grid (5.9), it is projected back to the original time grid by linear interpolation and finally re-mapped from time to the positions d_i using (5.3).

5.2 ECMS with Predictive Reference Signal Generator

At this point, the non-predictive ECMS can be combined with the predictive reference signal generator as illustrated in Fig. 5.1. Instead of a constant value, the ECMS obtains now a time- or position-dependent reference value $\xi_{ref}(t)$. This reference signal requests that the SoC of the battery is lowered by the ECMS before some important recuperation phases occur. This ensures that most of the available energy can be recuperated. In the following, this predictive energy management strategy is referred to as pRSG-ECMS. The block diagram in Fig. 5.4 shows the system consisting of the predictive controller and the vehicle on a system level.

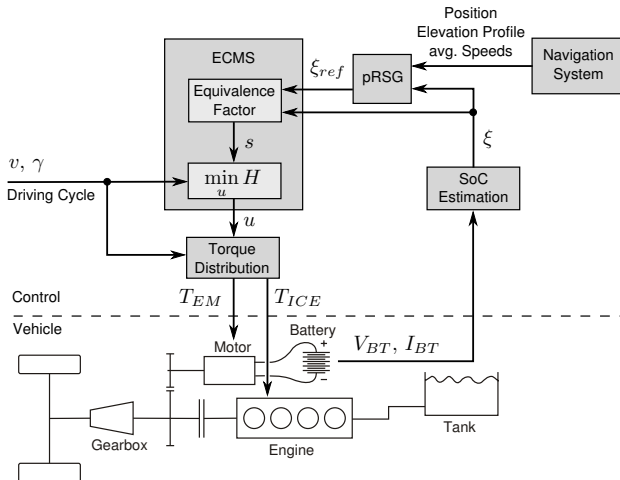


Figure 5.4: System level block diagram of the pRSG-ECMS control system with the vehicle.

5.2.1 Definition of Test Framework

Since both strategies, namely the pRSG-ECMS and the standard ECMS, are causal, neither of them can guarantee that the specified final SoC is achieved exactly. Consequently, the resulting fuel consumption (FC) of each strategy over a driving cycle cannot be compared with the other

because the change of the electric energy content in the battery over the cycle is not equal in both cases. Therefore, each strategy is compared with the corresponding global optimal solution. This optimal solution is evaluated for the same initial and final state as resulting from each strategy. The relative excess consumption rEC introduced in Sec. 4.2.3 is used in all cases to compare the results.

5.2.2 Simulation of the Navigation System

To assess the quality of the proposed method, simulations of all three cases (ECMS, pRSG-ECMS, and DP) must be carried out. The pRSG-ECMS requires the data provided by the navigation system to be available. These data points are derived from the exact driving profiles for simulation as follows:

- Topographic data points provided by the navigation system are assumed to be exact. Therefore, the data points defined in the driving profile are used for the simulation as well as for the prediction.
- In contrast, the speed profile cannot be predicted exactly by the navigation system. Therefore, using the exact driving profile, an average speed is computed which is used as the simulated output available from the navigation system. This approximation is very rough on purpose. Fig. 5.5 shows this approximation for the first part of SWISSelv. The algorithm that was used to construct the simulated average traveling speed is listed in Appendix E.

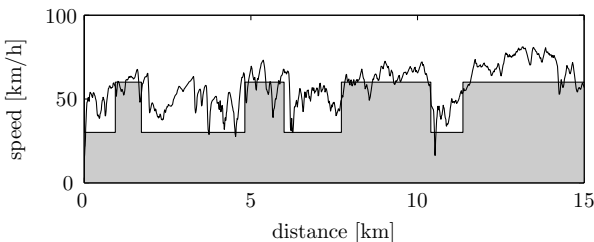


Figure 5.5: Approximated data of the simulated average traveling speed (filled) as provided by the navigation system (first part of the SWISSelv cycle) together with the real driving cycle (solid line).

5.3 Simulation Results

This section shows the results of the simulations carried out for the three test cycles with elevation changes (FTPelv, US06elv, and SWISSelv). The parameters for the ECMS and for the pRSG-ECMS are identical to assure that both strategies yield the same results on flat terrain. The parameters are listed in Table 4.2. The additional parameters used for the pRSG are shown in Table 5.1.

Fuel consumption and the relative excess consumption of the two causal strategies are summarized in Table 5.2. In hilly environment, the pRSG-ECMS performs considerably better than the ECMS. The fuel consumption with the pRSG-ECMS deviates by less than 5.1% from the optimal solution for the cycles investigated here. For the cycle US06elv, the pRSG-ECMS yields almost optimal fuel consumption. This is explained by the fact that the driving cycle has an almost constant speed near the value of 60 km/h that closely matches the estimation of the navigation system. Furthermore, the altitude profile of this driving cycle shows a relatively uniform road grade, first ascending, then descending.

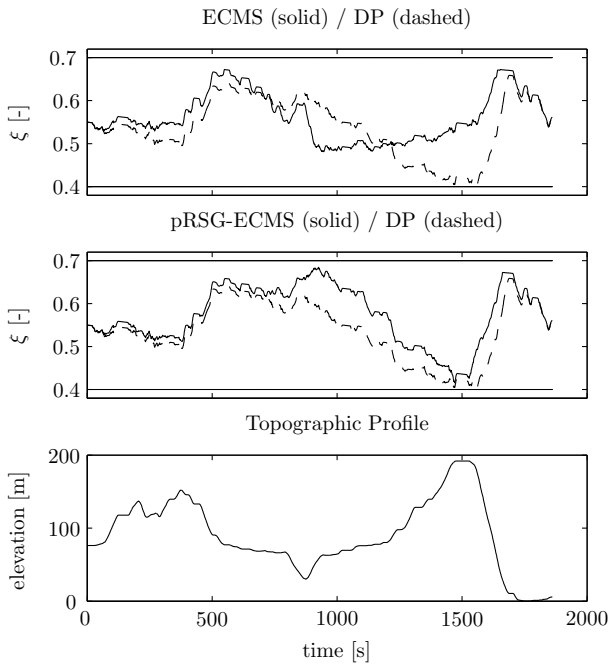
Figures 5.6, 5.7, and 5.8 show the state trajectories of the ECMS and the pRSG-ECMS with the corresponding optimal state trajectories obtained with DP (dashed). In addition, the topographic profile is shown to point out the interconnection between (future) elevation and SoC. These figures illustrate that, particularly for the US06elv, the state trajectory obtained with the pRSG-ECMS is closer to the optimal solution than that obtained with the standard ECMS. A comparison of the topographic profile with the SoC trajectory shows that the proposed strategy lowers the SoC before important recuperation events take place.

Table 5.1: Parameters for the pRSG-ECMS.

Parameter	Value	Unit
η_{recup}	0.7	-
ξ_{min}	0.4	-
ξ_{max}	0.7	-
$\delta\xi_f$	0.01	-
α_ε	10^8	s^{-2}
$\alpha_{\varepsilon,f}$	10^7	s^{-2}

Table 5.2: Simulation results for three cycles with elevation changes.

Cycle	Strategy	FC (Strategy/DP)	rEC
		[l/100km]	[%]
FTPelv	ECMS	4.55 / 4.20	+8.3
	pRSG-ECMS	4.42 / 4.20	+5.2
US06elv	ECMS	8.07 / 7.64	+5.7
	pRSG-ECMS	7.45 / 7.45	+0.0(2)
SWISSelv	ECMS	3.90 / 3.54	+10.1
	pRSG-ECMS	3.63 / 3.54	+2.4

**Figure 5.6:** SoC trajectories of ECMS vs. DP and pRSG-ECMS vs. DP for cycle FTPelv and its elevation profile.

5.4 Conclusions

The non-predictive, causal control strategy from Sec. 4.2 (ECMS) is extended in this chapter with an algorithm that computes a reference tra-

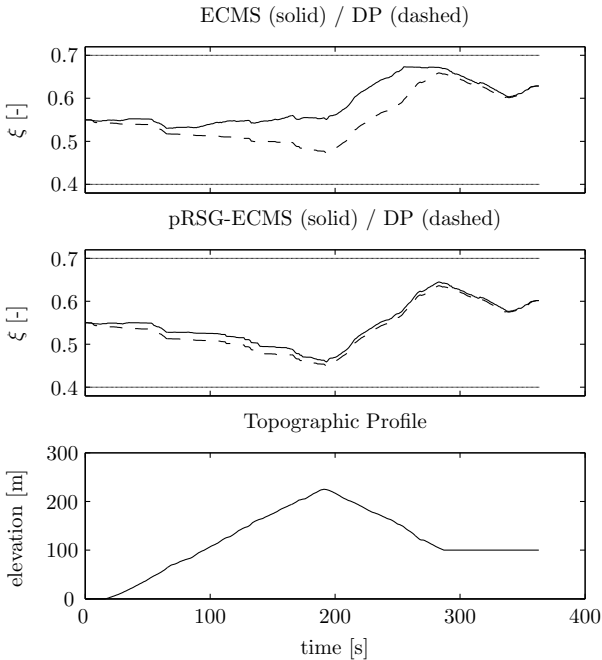


Figure 5.7: SoC trajectories of ECMS vs. DP and pRSG-ECMS vs. DP for cycle US06elv and its elevation profile.

jectory for the state-of-charge of the battery. This reference trajectory assures that the state-of-charge is kept well within its constraints even if large amounts of energy resulting from elevation changes are recuperated. The algorithm presented here is computationally efficient since it could be formulated as a quadratic program. Further, it relies only on data from the navigation system assuming this system comprises topographic maps. Consequently, the algorithm is well suited for real-time application in the control unit of a hybrid vehicle.

Simulation results have shown that the fuel consumption can be reduced considerably compared to the non-predictive strategy from Sec. 4.2 for driving cycles with topographic profiles. For the SWISSelv driving cycle with great elevation changes, the non-predictive strategy showed an increased fuel consumption toward the global optimum by 10.1%. In contrast, the predictive strategy improved the fuel consumption such that it

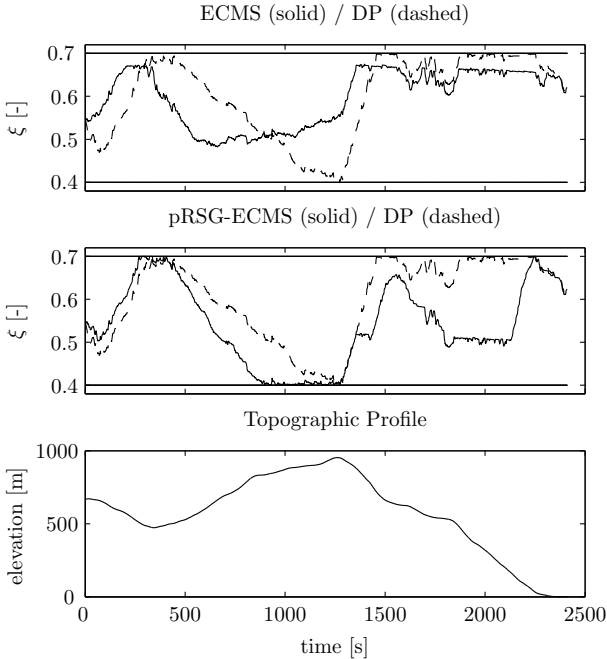


Figure 5.8: SoC trajectories of ECMS vs. DP and pRSG-ECMS vs. DP for cycle SWISSelv and its elevation profile.

was only 2.4% higher than the global optimum for this specific driving cycle. The smallest improvement was observed for the FTPelv cycle where the relative excess consumption improved from 8.3% to 5.2% by application of the predictive reference trajectory.

Since the predictive algorithm developed in this chapter does not assume a specific powertrain topology, it can be used for any hybrid powertrain if the corresponding non-predictive energy management strategy allows for reference tracking of the state-of-charge. Furthermore, the proposed algorithm seems to be very promising for application in a plug-in HEV. Such a vehicle has a considerably larger battery than a standard HEV, allowing to use electric energy as a primary energy source. Hence, the initial condition of the battery is typically ‘fully charged’, the optimal final condition ‘completely discharged’, i.e., the condition on charge sustenance can be omitted for plug-in HEVs. This final condition is optimal

in the sense of monetary energy cost for the current prices on electricity and fuel in most countries [36]. The predictive algorithm presented here can be used for plug-in HEVs by simply setting the target final state of the battery ξ_{set} equal to the lower constraint $\xi_{ref,min}$. Clearly, the end of the trip corresponds to the place where the battery will be recharged.

Chapter 6

Predictive Engine Start/Stop Decision

The models deployed in the previous chapters of this thesis all neglect the energetic costs that result from a start of the engine. However, such costs are present in reality. To start the engine, some additional torque must be provided by the electric path to accelerate the engine. This yields a consumption of electric energy which at some time must be generated from fuel. In addition to the electric consumption, some additional fuel must be injected at each engine start to build up the wall film for the case of port fuel injected engines, as it will be discussed later.

If a control strategy does not include such starting costs in the underlying model, frequent engine starts can occur. This happens especially for constant speed sections where such a ‘duty cycling’ at high frequency is indeed optimal if no starting costs are present. If such a duty cycling is commanded by the control strategy in a real vehicle, fuel consumption increases due to the starting cost. Further, the comfort for the driver is reduced and wear of the components is increased, especially for the clutch. To avoid such duty cycling, introduction of an additional penalty on each engine start has been proposed in literature [8]. Such a penalty indeed reduces the frequency of the duty cycling for constant speed profiles. However, on a real driving cycle, the engine start is delayed by the penalty that can lead to inefficient operating points of the powertrain. It is clear, that the optimal decision can only be found if the future driving profile is taken into account.

In this chapter, the global optimal solution is evaluated with DP for the base model that does not include any starting cost, but also for two different models including starting cost. This investigation shall reveal the

impact of the starting cost on the fuel consumption but also on the number of engine starts. Later, a suboptimal, model predictive control (MPC) is investigated to evaluate how much of this theoretical fuel saving potential can be realized as a function of the length of the prediction horizon.

6.1 Model of the Hybrid Powertrain Including Engine Start

The original model from Chapter 2 is extended in this section with a simple physical model for the engine start. Since the state of the engine must be saved in the computation in order to be able to detect a change of the engine state, the state vector of the model increases by one dimension. In the original model, the only state variable was the state-of-charge ξ of the battery. Here, a new state variable is introduced to describe the state of the engine. Since the engine can only be on or off, this variable is binary. Let's call this variable x_{ICE} . The resulting state vector is

$$x = \begin{bmatrix} \xi \\ x_{ICE} \end{bmatrix}. \quad (6.1)$$

6.1.1 ICE Start

The engine in full parallel HEVs is typically started by closing the clutch such that some torque is transmitted to the engine. Consequently, the engine is accelerated up to the speed of the gearbox input ω_{GB} . In order to guarantee the driver's comfort, the electric motor must compensate the torque transmitted by the clutch in addition to the torque that needs to be provided for propulsion. Injection of fuel starts as soon as the engine reaches the speed of the gearbox and the clutch is fully engaged. However, at the beginning of the injection, additional fuel must be injected to the fuel used for combustion. This additional fuel is necessary to build up the wall-film [37, 38] in the intake manifold. Consequently, there are two effects contributing to the cost that must be accounted for an engine start: Firstly, the additional electric energy necessary to provide the torque to accelerate the engine. This electric energy is finally compensated by chemical energy, i.e., resulting as fuel cost. Secondly, some additional amount of fuel to build up the wall-film must be injected. This results directly in an increase of

the fuel consumption. The wall film is only relevant in a port fuel injected (PFI) engine. For a direct injected (DI) engine, it can be neglected. Both engine types are studied in this chapter.

There exist many other possibilities to start the engine. However, the starting procedure shown here represents the standard engine start in full parallel HEVs.

To model the starting of the ICE in the quasi-static simulation (QSS), the simulation must be refined in order to capture the starting sequence which is faster than one sampling period $\Delta t = 1$ s of the QSS. Therefore, the sampling period during which a start occurs is divided in two periods as illustrated in Fig. 6.1: First, the starting period of length t_{st} is defined where the engine is accelerated from zero speed up to the speed of the gearbox ω_{GB} . Then, the propulsion period of length $t_{pr} = \Delta t - t_{st}$ results during which the powertrain is in regular propulsion mode. The starting torque $T_{st} = 45$ Nm is constant and defined by the controller of the clutch, i.e., the clutch is closed by a controller such that this constant torque is being transmitted until the speeds of both sides of the clutch match.

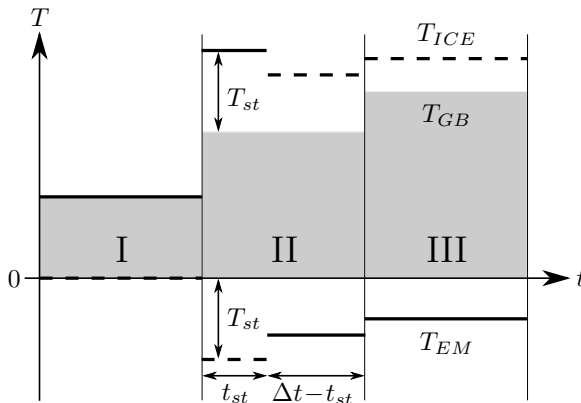


Figure 6.1: The quasi-static torques of the gearbox (gray box), electric motor (solid line), and combustion engine (dashed line) during pure electric driving (I), ICE start (II), and recharging (III).

The time required to accelerate the engine from zero speed to the rotational speed of the gearbox ω_{GB} can be computed with the engines inertia Θ_{ICE} , the starting torque T_{st} , and the brake torque of the dragged engine

$T_{brq} = -18$ Nm as follows

$$t_{st} = \frac{\Theta_{ICE} \cdot \omega_{GB}}{T_{st} - T_{brq}}. \quad (6.2)$$

For the case where the maximum torque of the electric motor is not sufficient to fulfill the requested torque at the gearbox during the starting period, it is possible to compensate for the missed torque in the propulsion period of this sampling period such that the energy provided to the gearbox corresponds to the requested value. The resulting torque at the gearbox for the propulsion period is then given by

$$T_{GB,pr} = \frac{\Delta t \cdot T_{GB} - t_{st} \cdot (T_{EM,eff,ac} - T_{st})}{\Delta t - t_{st}}, \quad (6.3)$$

where $T_{EM,eff,ac}$ is the torque that is effectively provided by the electric motor. The electric motor is capable to be overloaded for a short time. During the starting sequence of the engine, the motor is allowed to be overloaded by the starting torque T_{st} . Hence, the effectively available torque during the starting sequence is given by

$$T_{EM,eff,ac} = \min(T_{GB} + T_{st}, T_{EM,max}(\omega_{GB}) + T_{st}). \quad (6.4)$$

The mass of the fuel wall film that has to be build up at every start is modeled to be constant given by the variable m_{wf} . The assumption of a constant value for this parameter will be discussed below and its sensitivity is investigated in Sec. 6.2.3.

6.1.2 ICE Stop

In order to stop the engine, the clutch is disengaged and the injection is stopped. However, the engine carries out a few revolutions until it comes to a full stop. During that time, the fuel stored in the wall film is evaporated, passes through the cylinders, and is finally lost for propulsion after the next engine start. Similarly, the kinetic energy stored in the engine cannot be recuperated by the electric path. This is a consequence of the parallel topology where the speed of the motor is fully determined by the speed of the gearbox input.

6.1.3 Combined Backward/Forward Approach

Quasi-static, backward-facing models are commonly applied to estimate fuel consumptions for vehicles on a given driving cycle [17, 18, 39]. *Quasi-static* means for such models that all signals are assumed to be constant over one time step. Further, the consumption of the power converters is evaluated for static operation. The term backward-facing describes the direction of the signals. Simulations that are backward-facing start the computations from the cycle, through the powertrain, back to the power converters. This direction is inverse to the physical direction. Physically, the starting point is a cause (e.g. force) that results in an effect (e.g. acceleration), i.e., *forward-facing*. In backward-facing models the effect is given and the corresponding cause is calculated. This procedure allows for fast computations of the fuel consumption for a given driving cycle.

However, such backward-facing approaches fail if the requested driving cycle is not feasible due to limitations in the powertrain such as maximum torques, currents, and so forth. This issue becomes more important for the model presented in this chapter, since the maximum torque depends strongly on the state of the engine. In the case of strategies with a limited prediction horizon, the vehicle can run into a situation, where the vehicle accelerates with engine being off. If the requested acceleration is then too high for the electric motor only, some torque from the engine is required to fulfill the requested torque. However, starting the engine reduces the available torque additionally. This results in a situation where the requested torque cannot be provided by any means for the actual engine state. Nevertheless, the driving cycle per se is feasible: if the engine was started earlier, this situation would be perfectly feasible.

In this study fully predictive strategies as well as control strategies with limited prediction horizon are investigated. Therefore, a purely backward-facing model cannot be applied for all cases as explained above. Consequently, a combined approach is taken: The signals are computed in a backward fashion, first. If some signals are being limited, the entire path is calculated forwards with the limited signals resulting in the maximum feasible acceleration. This results in a speed profile deviating from the original driving cycle. This *combined backward/forward approach* is also used in the ADVISOR simulation toolbox [31]. In order to guarantee comparability, the modified driving cycle is being saved after each simulation and being applied for computation of the optimal reference fuel consumption.

6.2 Optimal Control

In order to evaluate the optimal control to drive the model presented in Sec. 6.1 from some initial state x_0 to some final state x_f , deterministic dynamic programming (DP) is again applied as introduced in Chapter 3. Since the second state variable, namely the engine state, is binary, only one state variable, namely the state-of-charge, needs to be discretized.

The cost function to be minimized is again the fuel energy consumption

$$J = \int_0^{t_f} H_l \cdot \dot{m}_f^*(\tau) d\tau, \quad (6.5)$$

where \dot{m}_f^* is the fuel mass flow, and H_l is the lower heating value of the fuel.

The motivation to evaluate the global optimum is manifold. Firstly, the optimal solution for three different models is being compared. These models encompass a model without any modeling of the ICE starting, a model with PFI where ICE starting is modeled, and a model with DI also including ICE starting. This comparison shall point out whether it is worth to model the ICE starting or not. Secondly, a sensitivity analysis is carried out in order to investigate the sensitivity of the mass of the wall film on the fuel consumption. Thirdly, the global optimum is used in Sec. 6.3 as a benchmark to gauge suboptimal solutions.

6.2.1 Three Different Models

The optimal fuel consumption is evaluated here for three different models. The first model is referred to as *base model* where ICE-starting is not modeled. This model is the one used in the previous chapters and is described in Chapter 2. For this model, the engine can be started at any time if the speed of the gearbox is above idle speed. There is no energy necessary to start the engine, neither from the electric path, nor from any additional fuel consumption.

The other two models contain a simple model for the engine start as introduced in Sec. 6.1.1. The amount of fuel m_{wf} that is lost at each start is assumed to be zero $m_{wf} = 0$ g for a direct injected engine, for a port fuel injected engine it is assumed with $m_{wf} = 0.3$ g.

6.2.2 Results from DP for the Three Models

The simulations carried out in this chapter use four regulatory driving cycles, namely NEDC, FTP-72, LA-92, and CADC. These driving cycles have no topographic profile and their speed profiles are shown in Appendix B. The simulation results obtained by DP with an initial and final state of $x_0 = x_f = [0.55, 0]^T$ for the four driving cycles and the three models are summarized in Table 6.1. The fuel consumption FC which is equivalent to the cost function (6.5) is, obviously, always minimal for the model without any starting cost.

The fuel consumption of the model with starting cost and direct injection is increased by 0.9%–3.9% compared to the base model. The model with starting cost and port fuel injection shows the highest fuel consumption of the three models with an increase of 1.7%–5.1% compared to the base model. The order of these results is not surprising since the base model neglects the electric and chemical energy required for starting the engine completely, the DI-model takes into account the electric starting energy, and the PFI-model additionally consumes chemical energy for each start. The interesting point is that the increase in fuel consumption is mainly caused by modeling the electric part of the starting, whereas the energy lost by the wall film introduces a smaller increase in fuel consumption. Further, the number of ICE starts are also reported in Table 6.1. In order to improve comparability over the cycles, the number of starts per unit of time is also given. A similar conclusion can be drawn here: Modeling the electric starting cost yields the biggest change, i.e., reduction of the number of starts. Modeling the wall film fuel mass yields a further reduction of the number of ICE starts, but its effect is less pronounced.

6.2.3 Sensitivity Analysis

The wall film mass m_{wf} is the most uncertain parameter of this model. Its value is not constant during operation, it varies mainly with temperature of the engine, but also with the operating point [37, 38]. Consequently, the wall film mass that is lost at each engine stop is determined by the engine temperature and operating point at the time of the shutdown. However, the wall film mass is assumed to be constant for simplicity. Therefore, a careful analysis is carried out to investigate the sensitivity of the fuel consumption to the the wall film mass in order to validate this assumption.

Table 6.1: Simulation results of DP with the base model where ICE starting is not modeled, and the two models where ICE starting is modeled once with $m_{wf} = 0.3$ g for PFI, once with $m_{wf} = 0$ g for DI. The relative difference to the model without modeling of ICE starting is indicated in parenthesis.

Cycle	model with ICE-starting	FC [l/100km]	N_{st} [-]	$\frac{N_{st}}{t_f}$ [min ⁻¹]
NEDC	no	4.80	24	1.22
	yes (DI)	4.85 (+0.9%)	12 (-50.0%)	0.61
	yes (PFI)	4.88 (+1.7%)	8 (-66.7%)	0.41
FTP-72	no	4.35	63	2.76
	yes (DI)	4.49 (+3.2%)	21 (-66.7%)	0.92
	yes (PFI)	4.54 (+4.4%)	17 (-73.0%)	0.75
LA-92	no	5.46	91	3.80
	yes (DI)	5.68 (+3.9%)	30 (-67.0%)	1.25
	yes (PFI)	5.74 (+5.1%)	24 (-73.6%)	1.00
CADC	no	6.67	252	4.82
	yes (DI)	6.86 (+2.9%)	72 (-71.4%)	1.38
	yes (PFI)	6.92 (+3.7%)	62 (-75.4%)	1.19

This sensitivity analysis is carried out by evaluation of the optimal control with a constant wall film mass in the range $m_{wf} \in [0, 0.5]$ g. The resulting optimal control is then applied to the model with the ‘true’ wall film mass $m_{wf} = 0.3$ g. The resulting fuel consumption normalized with the minimal fuel consumption achieved on each driving cycle is shown in Fig. 6.2. These results reveal that a wrongly estimated wall film mass yields an excess in fuel consumption of less than 0.3 % even if the parameter is estimated with a value of 0 g instead of 0.3 g. If the more realistic range of 0.3 ± 0.1 g is considered, the excess in fuel consumption is less than 0.1%. Consequently, the sensitivity of the wall film mass on the fuel consumption is very small and the assumption of a constant value proves to be sufficient for the current purposes.

Although the fuel energy consumption is the objective function to be minimized in this chapter, it is worth to have a look at the number of engine starts N_{st} over the driving cycle. Figure 6.3 depicts the number of engine starts normalized with the minimum number of starts for each cycle. These results reveal that the number of ICE starts decreases with the mass

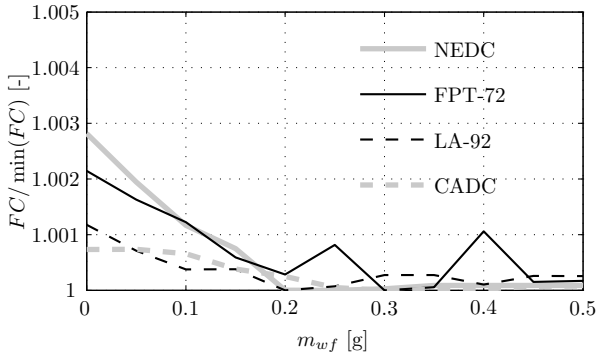


Figure 6.2: Sensitivity of the assumed wall film mass m_{wf} in the control on the fuel consumption FC . The ‘real’ wall film mass of the model is $m_{wf} = 0.3$ g.

of the wall film that is assumed in the control, as expected. However, as resulting from Fig. 6.2, choosing a too high value for m_{wf} can be beneficial in terms of components wear and comfort, since this reduces the number of ICE starts further while sacrificing only little fuel economy.

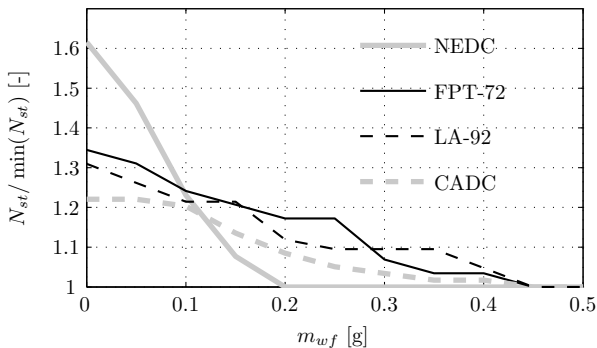


Figure 6.3: Sensitivity of the assumed wall film mass m_{wf} in the control on the number of ICE starts N_{st} normalized by the minimum ICE starts achieved for each cycle. The ‘real’ wall film mass of the model is $m_{wf} = 0.3$ g.

6.3 Suboptimal Control

Since there is no information on the entire future driving conditions available in reality, a study on the optimal prediction horizon is carried out to answer the question ‘what prediction horizon is necessary to capture most of the fuel saving potential’. To answer this question, a model predictive control scheme [40] is being set up.

6.3.1 Model Predictive Control

The MPC scheme applied here evaluates the optimal control signal starting from the current state of the system and solving an optimal control problem for the known disturbance (driving cycle) over the prediction horizon t_h . From the resulting control signal of length t_h only the first element is used during the current time step. The rest of the signal is dismissed and one time step later, the optimal control problem is solved again over the time horizon t_h . In order to solve the optimal control problem at each time, DP is used within the time horizon since this technique yields the optimal solution for a nonlinear, constrained problem. Further, since this study is limited to simulations, computational cost is not an issue here. However, MPC schemes relying on DP can be applied in real-time for the control of hybrid electric vehicles as it has been successfully demonstrated in [23]. The computational effort depends strongly on the number of state variables, but also on the prediction horizon and their discretization, respectively.

Details on the MPC Implementation

Even though the MPC scheme is predictive, the time horizons used here are too short to prevent the state-of-charge from running into its constraints, especially if long recuperation phases occur as discussed in Chapter 5. Therefore, a penalty on the state-of-charge is introduced in the cost function as in Sec. 4.2 with the same values of the tuning parameters.

The optimal control problem solved at every time t for the MPC is minimizing the cost function

$$J_{MPC} = K(x(t + t_h)) + \int_t^{t+t_h} \left\{ H_L \cdot \dot{m}_f^* (\tau) + \alpha \left(\frac{\xi_{ref} - \xi(\tau)}{\Delta \xi_{nrm}} \right)^{2q} \right\} d\tau. \quad (6.6)$$

The final cost $K(x)$ assigned to each state at the end of the time horizon is crucial for the performance of the MPC. If the optimal cost-to-go function $\mathcal{J}(x, t + t_h)$ resulting from the DP problem with the penalty on the state-of-charge would be used for each specific cycle, the MPC solution would be identical with the DP solution. However, the optimal cost-to-go function contains information on the entire future driving behavior which is undesirable for the current study. Therefore, a time-invariant final cost is applied. It is chosen as the temporally averaged optimal cost-to-go function of the DP problem with a penalty on state-of-charge deviations. In order to avoid over-fitting to a specific cycle, the DP was evaluated on a cycle consisting of NEDC, FTP-72, LA-92, and CADC in sequence. To reduce the impact of the final state constraint, this cycle was repeated twice consecutively, but only the first part was used to compute the time-invariant final cost.

The final cost $K(x)$ for the MPC is obtained from the cost-to-go function $\mathcal{J}(x, t_i)$ as

$$K(x) = \frac{\sum_{i=1}^N (\mathcal{J}(x, t_i) - \min_x \mathcal{J}(x, t_i))}{N}, \quad (6.7)$$

where N is the number of (time) samples.

6.3.2 Simulation Results

The simulations are carried out for all four driving cycles, for prediction horizons of $t_h = 1, 2, \dots, 15$ s, and for both engine types PFI and DI. The fuel consumption between these results cannot be compared directly because it depends on the change in the state-of-charge of the battery over the cycle. In order to compare these results, the fuel consumption achieved by the MPC is compared to the optimal fuel consumption evaluated by DP with the same final state as reached using MPC. Further, since the speed profile resulting from the MPC with limited horizon can have small deviations from the original speed profile, the DP solution is evaluated for the speed profile that was stored during the simulation using MPC. The difference of these two fuel consumptions, i.e., the fuel consumption of the suboptimal MPC and the optimal DP, is expressed again as the relative excess consumption rEC as it was used in Sec. 4.2.3, given by (4.10).

The simulation results show that the SoC-penalty used in the MPC scheme is sufficient because the SoC does not reach its constraints in any of the driving cycles. All simulations proved to be valid.

Figures 6.4 and 6.5 illustrate the relative fuel consumption as a function of the prediction horizon and for various cycles for both engine types, respectively. These figures show that with the minimum prediction horizon of $t_h = 1$ s, there is a maximum potential of 4% (3%) for the PFI (DI) engine toward the global optimum. Obviously, the best fuel saving is achieved for the longest prediction horizons, but these graphs are very flat for longer horizons. This reveals that even a relatively short prediction horizon of approximately 4 seconds is sufficient to achieve most of the potential independent of the value of the wall film mass m_{wf} . This result is very promising since predictions of the speed profile over 4 seconds seem to be realistic with current technology. At this point, it must be mentioned that this study relies on the assumption that the prediction within the horizon is perfect. In reality, any prediction is uncertain.

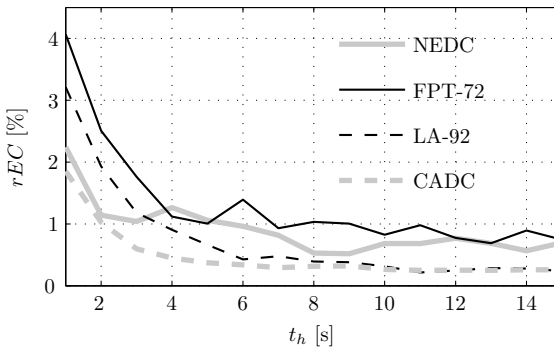


Figure 6.4: Relative fuel consumption for different prediction horizons. Base model is the PFI-engine with $m_{wf} = 0.3$ g.

6.4 Conclusion

This chapter shows the importance of proper modeling of the engine start cost. An evaluation of the optimal fuel consumption of the model without start cost and the two models including start cost for direct injection and port fuel injection has been carried out. This investigation reveals, that the fuel consumption for a model with starting cost can be up to 5.1% higher in the case of PFI, and up to 3.9% higher for DI compared to the

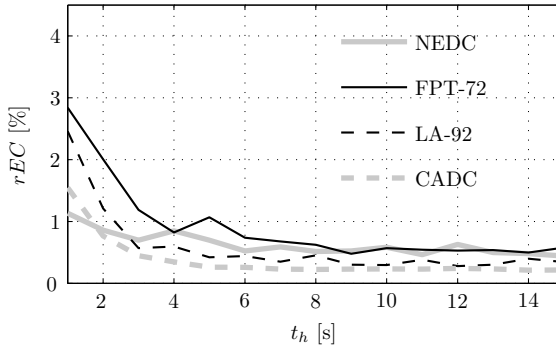


Figure 6.5: Relative fuel consumption for different prediction horizons. Base model is the DI-engine with $m_{wf} = 0$ g.

model that neglects starting cost. These maximum values are observed for the LA-92 driving cycle.

These important differences motivate to include the starting cost in the energy management for parallel electric hybrid vehicles. Since the absolute value of the wall film mass is rather uncertain and since it also depends on the operating points, a sensitivity analysis on this parameter has been carried out. This analysis reveals that the sensitivity is rather small. The maximum excess in fuel consumption is less than 0.3% if the mass is assumed to be zero instead of 0.3 g. For a more reasonable range of 0.3 ± 0.1 g for the wall film mass, the fuel consumption increased by less than 0.1%. These results justify the assumption of a constant wall film mass. Further, it has been observed, that overestimating the wall film mass yields a very small increase in fuel consumption, but the number of engine starts could be further reduced.

The step toward a causal control has been carried out by using a model predictive controller. This MPC control uses dynamic programming over a short time horizon and requires a prediction of the future driving cycle for this horizon. An investigation of the fuel consumption with respect to the global optimum has been carried out for various lengths of the prediction horizon. The results showed clearly, that some prediction is necessary to find an appropriate decision for the engine start and stop. However, a short prediction horizon of about 4 s is sufficient to achieve good fuel consumption. Such a short prediction is realistic with current technology.

Chapter 7

Summary & Conclusions

The aim of this project was to develop novel control strategies for the operation of a full parallel hybrid electric powertrain that minimize the fuel consumption over the driving cycle. In a first step, the global optimal solution was evaluated by means of dynamic programming. This technique requires full knowledge of the driving cycle. The resulting control laws are therefore not immediately useful for real-time implementation. However, they are very valuable in order to benchmark the performance of any other suboptimal, but realizable control strategy.

Since the dynamic programming method requires a discrete-time model of the plant and a quantized state-space, it is prone to numerical errors, particularly when a specified final state is enforced. A novel method has been developed that reduces the mismatch between desired and achieved final state, but also the computational cost significantly.

Causal control strategies were found using Pontryagin's minimum principle. Assuming no knowledge on future driving conditions, a causal, non-predictive controller was derived with this method. This controller minimizes the equivalent fuel cost at every sampling time. The equivalent fuel cost is computed by weighting the fuel consumed by the engine against the electric energy consumed inside the battery using an equivalence factor. Such equivalent fuel consumption minimization strategies are known in literature. However, in this work a novel and detailed derivation is presented that includes a penalty on the deviation of the battery state-of-charge with respect to a desired reference value.

A simplified model has been presented and validated against the original model. This simplified model allowed to derive analytical expressions for the control candidates. This novel control law consists of a simple rule based map which is determined by powertrain parameters only. Eval-

uation of this control law is computationally significantly more efficient than minimizing the Hamiltonian numerically at every time sample. Using this simplified control a lower saturation in the equivalence factor could be found analytically. This allowed to extend the causal control with an anti-windup scheme.

The ECMS achieved a fuel consumption that was very close to the global optimum on most driving cycles. However, as soon as the amount of recuperated energy became important compared to the storage capacity of the battery, the performance of ECMS decreased considerably, as for example in driving cycles with altitude variations. This decrease in performance can be explained by the fact that the ECMS is non-predictive and its derivation assumes an unconstrained battery. If long recuperation phases occur, it is obvious that the state-of-charge of the battery should be lowered prior to each important recuperation phase. This would then allow to capture the recuperable energy within the constraints of the battery. Such a behavior can only be achieved by exploiting some information on the future driving conditions. In this work, a novel algorithm has been developed that exploits data from the navigation system such as the topographic profile and the average traveling speeds of the planned trip. This algorithm is called predictive reference signal generator (pRSG) and computes an appropriate reference trajectory for the state-of-charge to the end of the trip. Since the ECMS is capable to track some reference values for the state-of-charge, the ECMS and the pRSG have been joint to a predictive energy management system. As a result, good performance in terms of fuel consumption was achieved even in driving cycles with topographic profiles. Since the proposed algorithm is formulated as a quadratic program, it is computationally very efficient and well suited for real-time application in the vehicle.

The control strategies developed in this work rely on a model that does not account for any energetic consumption required to start the engine. In reality, there is some additional torque required from the electric motor to accelerate the the engine during startup. Depending on the type of engine, a certain amount of fuel is required for each start. In order to evaluate the impact of the starting cost on the total fuel consumption, the model has been extended with such starting costs. An investigation with DP revealed that the engine start should not be neglected for energetic reasons, as well as for reasons of comfort and components wear. Implementation

of a model predictive controller and a careful analysis with various lengths of the prediction horizon have shown that a short prediction horizon is sufficient for the decision to start or to stop the engine.

The conclusion of this work is that some prediction is helpful to minimize the integral fuel consumption. The proposed predictive energy management finally acts on two time scales: First, an accurate prediction of the torque requested by the driver over a short horizon improves the start/stop decision for the engine considerably. Second, a long-term prediction on the topographic profile and average traveling speeds on the planned trip allows to improve the management of the battery's state-of-charge to maximize the amount of recuperated energy.

Throughout this project, the powertrain components were assumed to be given, i.e., no optimization on the component dimensioning was carried out. Further, all components were modeled isothermally, i.e., thermal effects are neglected. An important topic in the field of hybrid electric vehicles is the aging of the battery. Such aging phenomena are also neglected. If appropriate models on battery aging would exist, the cost functional for the energy management could be extended with a penalty on the variables describing the battery aging. This would yield an energy management strategy that inherently reduces the aging of the battery. However, the battery's wear is not considered explicitly in this thesis. Nevertheless, it is possible to adjust the proposed control strategies to the aging of the battery and other components, because the control is defined by physical parameters of the powertrain. Hence, if the parameters are observed over lifetime of the vehicle, they can be adjusted in the energy management system. An adaptive control would result.

Appendix A

Nomenclature

Nomenclature		
Symbol	Description	Unit
A_f	Frontal area of vehicle	[m ²]
E	Energy	[J]
F	Force	[N]
FC	Fuel consumption	[l/100km]
H	Hamiltonian	[·]
H_l	Lower heating value	[J/kg]
I	Current	[A]
J	Cost functional	[·]
\tilde{J}	Extended cost functional	[·]
\mathcal{J}	Cost-to-go	[·]
P	Power	[W]
Q_0	Nominal battery capacity	[C]
R	Ohmic resistance	[Ω]
T	Torque	[Nm]
T_i	Integration time constant	[s]
T_h	Time horizon	[s]
V	Voltage	[V]
c_d	Aerodynamic drag coefficient	[-]
$c_{r,\{1,0\}}$	Rolling friction coefficients	[s/m], [-]
d	Distance	[m]
e	Internal efficiency of combustion engine	[-]
g	Gravitational acceleration	[m/s ²]
h	Elevation	[m]

Nomenclature

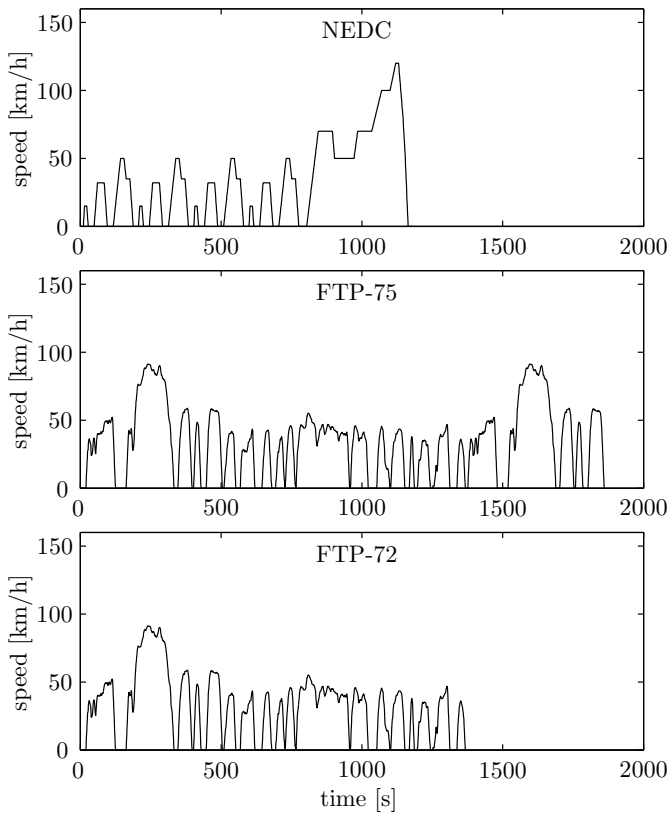
Symbol	Description	Unit
k_{GB}	Gear number	[-]
m	Mass	[kg]
m_{wf}	Mass of wall film	[kg]
\dot{m}_f^*	Fuel mass flow	[kg/s]
q	Parameter of order of SoC-penalty	[-]
r_{WH}	Effective wheel radius	[m]
r_{EC}	Relative excess consumption	[-]
s	Equivalence factor	[-]
t	Time	[s]
t_h	Time horizon of MPC	[s]
t_{st}	Starting time of ICE	[s]
u	Split factor	[-]
u	Control vector	[·]
v	Speed	[m/s]
x	State vector	[·]
z	Unknown vector in the QP	[·]
Θ	Rotational inertia	[kg m ²]
α	Weighting parameter of SoC-penalty	[·]
α_ε	Weighting parameter of slackness variables	[·]
β	Parameter of simplified battery model	[W ⁻¹]
γ	Road grade	[rad]
ε	Slackness variable	[·]
η	Efficiency	[-]
λ	Costate	[·]
ν	Gear ratio	[-]
ξ	State-of-charge	[-]
ρ_a	Air density	[kg/m ³]
τ	Time constant	[s]
ω	Rotational speed	[rad/s]

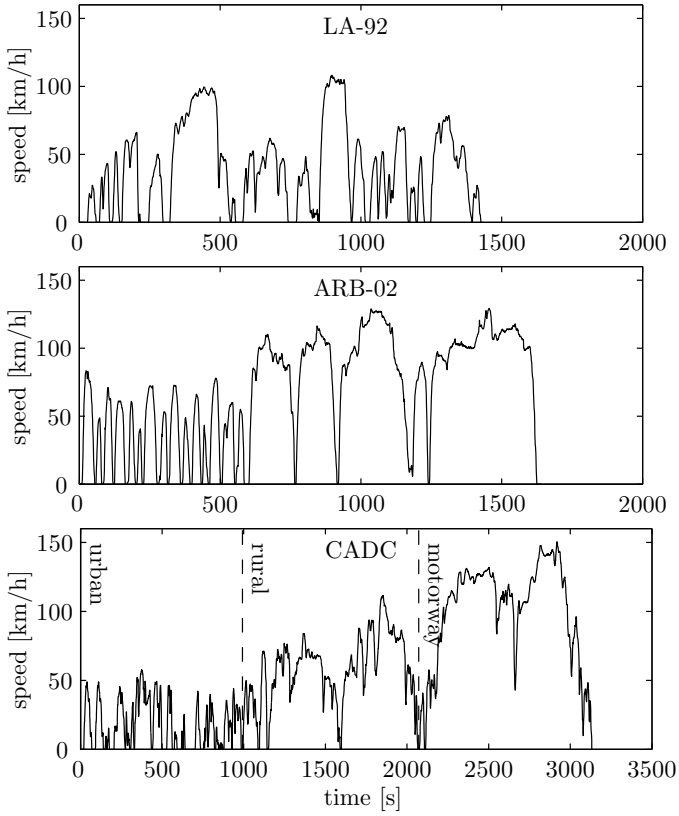
Abbreviations

Acronym	Description
2PBVP	Two-point boundary value problem
CFC	Causal feedback control
DI	Direct injection
DP	Dynamic programming
ECMS	Equivalent minimization strategy
ECU	Engine control unit
HEV	Hybrid electric vehicle
ICE	Internal combustion engine
MPC	Model predictive control
PFI	Port fuel injection
pRSG	Predictive reference signal generator
QP	Quadratic program
QSS	Quasi-static simulation
SHM	Selective Hamiltonian minimization
SI	Spark ignition

Appendix B

Regulatory Driving Cycles





Appendix C

Power Limits

The amount of boosting $P_m^{bo}(s)$ in (4.52) is limited by the electric motor maximum power constraint when

$$P_m^{bo}(s) > P_{mmax} \quad (C.1)$$

which is equivalent to

$$s < s_{lim}^{bo,m} \triangleq \frac{\eta^2}{e(2P_{mmax}\alpha + \eta)}. \quad (C.2)$$

The amount of recharging $P_m^{re}(s)$ in (4.54) is limited by the electric motor minimum power constraint when

$$P_m^{re}(s) < P_{mmin} \quad (C.3)$$

which is equivalent to

$$s > s_{lim}^{re,m} \triangleq \frac{1}{\eta e(1 + 2\alpha\eta P_{mmin})}. \quad (C.4)$$

When the electric motor minimum power constraint is active in the recharging region, electric driving is optimal for $P_d > 0$ when

$$H_{el}(P_d) < H_{re}(P_{mmin}) \quad (C.5)$$

$$P_d < P_{lim}^{re,m}(s) \triangleq \dots$$

$$\frac{-\left(\frac{s}{\eta} - \frac{1}{e}\right) + \sqrt{\left(\frac{s}{\eta} - \frac{1}{e}\right)^2 + 4\frac{s\alpha}{e\eta^2}\Psi_1}}{2\frac{s\alpha}{\eta^2}} \quad (C.6)$$

where

$$\Psi_1 = (P_0 + P_{mmin}(\eta es(1 + P_{mmin}\eta\alpha) - 1)). \quad (C.7)$$

If $P_d < 0$ then recuperation is optimal when

$$H_{el}^-(P_d) < H_{re}(P_{mmin}) \quad (\text{C.8})$$

$$P_d < P_{lim}^{re,m-}(s) \triangleq \dots$$

$$\frac{-\left(\frac{s}{\eta} - \frac{1}{e}\right) + \sqrt{\left(\frac{s}{\eta} - \frac{1}{e}\right)^2 + 4s\alpha\eta^2\Psi_2}}{2\frac{s\alpha}{\eta^2}} \quad (\text{C.9})$$

where

$$\Psi_2 = \left(\frac{P_0}{e} + \left(s\eta - \frac{1}{e} \right) P_{mmin} + s\alpha\eta^2 P_{mmin}^2 \right). \quad (\text{C.10})$$

Appendix D

Matrices of the QP

$$Q_{i,j} = \begin{cases} \frac{1}{\Delta t_i^2} + \frac{1}{\Delta t_{i+1}^2}, & \text{if } i = j = 1, \dots, N-1 \\ \frac{1}{\Delta t_N^2}, & \text{if } i = j = N \\ \alpha_{\varepsilon}, & \text{if } i = j = N+1, \dots, 2N \\ \alpha_{\varepsilon, f}, & \text{if } i = j = 2N+1 \\ -\frac{1}{\Delta t_i^2}, & \text{if } i = j-1 = 2, \dots, N \\ -\frac{1}{\Delta t_i^2}, & \text{if } i = j+1 = 1, \dots, N-1 \\ 0, & \text{else} \end{cases} \quad (\text{D.1})$$

$$p_i = \begin{cases} -\frac{2\xi_0}{\Delta t_N^2}, & \text{if } i = N \wedge N = 1 \\ -\frac{2\xi_0}{\Delta t_1^2} + \frac{2\tilde{\xi}_1}{\Delta t_1^2}, & \text{if } i = 1 \wedge N > 1 \\ -\frac{2\tilde{\xi}_{i-1}}{\Delta t_i^2} + \frac{2\tilde{\xi}_{i-1}}{\Delta t_{i+1}^2}, & \text{if } i = 2, \dots, N-1 \wedge N > 2 \\ -\frac{2\tilde{\xi}_{N-1}}{\Delta t_N^2}, & \text{if } i = N \wedge N > 1 \\ 0, & \text{if } i = N+1, \dots, 2N+1 \end{cases} \quad (\text{D.2})$$

$$A_{i,j} = \begin{cases} -1, & \text{if } i = 1, \dots, 2N-1 \wedge j = i \\ -1, & \text{if } i = 1, \dots, N \wedge j = i+N \\ 1, & \text{if } i = N+1, \dots, 2N-1 \wedge j = i-N \\ -1, & \text{if } i = 2N \wedge j = N \\ -1, & \text{if } i = 2N \wedge j = 2N+1 \\ 1, & \text{if } i = 2N+1 \wedge j = N \\ -1, & \text{if } i = 2N+1 \wedge j = 2N+1 \\ 0, & \text{else} \end{cases} \quad (\text{D.3})$$

$$b_i = \begin{cases} -\xi_{ref,min}, & \text{if } i = 1, \dots, N \\ \xi_{ref,max} - \Delta\tilde{\xi}_{i-N}, & \text{if } i = N+1, \dots, 2N-1 \\ -\xi_{set} + \delta\xi_f + \Delta\tilde{\xi}_N, & \text{if } i = 2N \\ \xi_{set} + \delta\xi_f - \Delta\tilde{\xi}_N, & \text{if } i = 2N+1 \end{cases} \quad (\text{D.4})$$

Appendix E

Construction of the Simulated Data Output of the Navigation System

It is assumed that the navigation system only distinguishes between urban, extra-urban, and highway with the corresponding regulatory speed limits of 50, 80, and 120 km/h, respectively. (Obviously, any other choice would work as well.) The average traveling speed assigned to each of these zones are assumed to be 30, 60, and 100 km/h, respectively.

To obtain the simulated estimated navigation data $\bar{v}(d)$ from the exact speed profile $v(t)$ of the test cycle, the following steps are carried out:

1. Converting the speed signal into an index signal $i(t)$ using threshold values of 55 and 85 km/h. The indices $i = 1, 2, 3$ stand for urban, extra-urban, or highway.
2. Filtering the index signal with a non-causal zero-phase low-pass filter with time constant $\tau = 30$ s.
3. Rounding the filtered index signal back to integers.
4. Replacing the indices back to traveling speeds of 30, 60, or 100 km/h.
5. Mapping of the average speed signal $\bar{v}(t)$ from time to position $\bar{v}(d)$.

Bibliography

- [1] A. Sciarretta and L. Guzzella, “Control of hybrid electric vehicles,” *IEEE Control Systems Magazine*, vol. 27, no. 2, pp. 60–70, 2007.
- [2] N. J. Schouten, A. Salman, and N. A. Kheir, “Energy management strategies for parallel hybrid vehicles using fuzzy logic,” *Control Engineering Practice*, vol. 11, no. 2, pp. 171–177, 2003.
- [3] J.-S. Won and R. Langari, “Intelligent energy management agent for a parallel hybrid vehicle - part II: Torque distribution, charge sustenance strategies, and performance results,” *IEEE Transactions on Vehicular Technology*, vol. 54, no. 3, pp. 935–953, 2005.
- [4] C. Lin, Z. Filipi, Y. Wang, L. Louca, H. Peng, D. Assanis, and J. Stein, “Integrated, feed-forward hybrid electric vehicle simulation in simulink and its use for power management studies,” 2001.
- [5] G. Paganelli, T. M. Guerra, J.-J. Santin, A. Noel, M. Delhom, and E. Combes, “Single shaft parallel hybrid car powertrain: Modelisation and control,” in *International Conference on Advances in Vehicle Control and Safety*, Amiens, France, July 1–4 1998, pp. 415–419.
- [6] G. Paganelli, T. Guerra, S. Delprat, J. Santin, M. Delhom, and E. Combes, “Simulation and assessment of power control strategies for a parallel hybrid car,” *Proceedings of the Institution of Mechanical Engineers, Part D: Journal of Automobile Engineering*, vol. 214, no. 7, pp. 705–717, 2000.
- [7] A. Brahma, Y. Guezennec, and G. Rizzoni, “Optimal energy management in series hybrid electric vehicles,” in *Proceedings of the American Control Conference*, Chicago, IL, 2000, pp. 60–64.
- [8] A. Sciarretta, M. Back, and L. Guzzella, “Optimal control of parallel hybrid electric vehicles,” *IEEE Transactions on Control Systems Technology*, vol. 12, no. 3, pp. 352–363, 2004.

- [9] C. Musardo, G. Rizzoni, Y. Guezennec, and B. Staccia, “A-ECMS: An adaptive algorithm for hybrid electric vehicle energy management,” *European Journal of Control*, vol. 11, no. 4–5, pp. 509–524, 2005.
- [10] S. Delprat, T. Guerra, and J. Rimaux, “Optimal control of a parallel powertrain: from global optimization to real time control strategy,” in *Proceedings of IEEE 55th Vehicular Technology Conference*, vol. 4, Birmingham, AL, May 6–9 2002, pp. 2082–2088.
- [11] R. Cipolone and A. Sciarretta, “Analysis of the potential performance of a combined hybrid vehicle with optimal supervisory control,” in *Proceedings of the 2006 IEEE International Conference on Control Applications*, Munich, Germany, October 2006, pp. 2802–2807.
- [12] M. Salman, M.-F. Chang, and J.-S. Chen, “Predictive energy management strategies for hybrid vehicles,” in *Proceedings of Vehicle Power and Propulsion, IEEE Conference*, Chicago, IL, September 7–9 2005, pp. 21–25.
- [13] R. E. Bellman, *Dynamic Programming*. Princeton, NJ: Princeton University Press, 1957.
- [14] D. Bertsekas, *Dynamic Programming and Optimal Control*. Belmont, MA: Athena Scientific, 1995.
- [15] L. Johannesson and B. Egardt, “A novel algorithm for predictive control of parallel hybrid powertrains based on dynamic programming,” in *Proceedings of the 5th IFAC Symposium on Advances in Automotive Control*, Monterey, CA, August 20–22 2007.
- [16] O. Sundström, L. Guzzella, and P. Soltic, “Optimal hybridization in two parallel hybrid electric vehicles using dynamic programming,” in *Proceedings of the 17th IFAC World Congress*, Seoul, Korea, July 6–11 2008, pp. 4642–4647.
- [17] L. Guzzella and A. Amstutz, “CAE tools for quasi-static modeling and optimization of hybrid powertrains,” *IEEE Transactions on Vehicular Technology*, vol. 48, no. 6, pp. 1762–1769, 1999.
- [18] L. Guzzella and A. Sciarretta, *Vehicle Propulsion Systems: Introduction to Modeling and Optimization*, 2nd ed. Berlin: Springer Verlag, 2007.

- [19] L. Guzzella, “Discrete-event IC engine models: Why the constant speed assumption is valid,” *Journal of Dynamic Systems, Measurement, and Control*, vol. 125, no. 4, pp. 674–676, 2003.
- [20] O. Sundström, D. Ambühl, and L. Guzzella, “On implementation of dynamic programming for optimal control problems with final state constraints,” in *Proceedings of Les Rencontres Scientifiques de l’IFP: Advances in Hybrid Powertrains*, Rueil-Malmaison, France, November 25–26 2008.
- [21] O. Sundström, D. Ambühl, and L. Guzzella, “On implementation of dynamic programming for optimal control problems with final state constraints,” *Oil & Gas Science and Technology — Rev. IFP*, 2009, accepted for publication.
- [22] M. Zahnert, “Optimal engine start/stop in parallel HEVs,” Master’s Thesis, Measurement and Control Laboratory, ETH Zurich, 2008.
- [23] M. Back, S. Terwen, and V. Krebs, “Predictive powertrain control for hybrid electric vehicles,” in *IFAC Symposium on Advances in Automotive Control*, Salerno, Italy, April 2004, pp. 451–457.
- [24] H. P. Geering, *Optimal Control with Engineering Applications*. Berlin, Germany: Springer Verlag, 2007.
- [25] L. V. Pérez and G. O. Garcia, “State constrained optimal control applied to supervisory control in HEVs,” in *Proceedings of Les Rencontres Scientifiques de l’IFP: Advances in Hybrid Powertrains*, Rueil-Malmaison, France, November 25–26 2008.
- [26] G. Rousseau, D. Sinoquet, and P. Rouchon, “Constrained optimization of energy management for a mild-hybrid vehicle,” *Oil & Gas Science and Technology — Rev. IFP*, vol. 62, no. 4, pp. 623–634, 2007.
- [27] M. Athans and P. L. Falb, *Optimal Control*. New York, NY: McGraw-Hill, 1966.
- [28] C. Musardo and B. Staccia, “Energy management strategies for hybrid electric vehicles,” Ph.D. dissertation, Politecnico di Milano, 2003.

- [29] A. Sciarretta, L. Guzzella, and C. Onder, “On the power split control of parallel hybrid vehicles: from global optimization towards real-time control,” *at-Automatisierungstechnik*, vol. 51, no. 5, pp. 195–203, 2003.
- [30] O. Barbarisi, F. Vasca, and L. Glielmo, “State of charge Kalman filter estimator for automotive batteries,” *Control Engineering Practice*, vol. 14, no. 3, pp. 267–275, 2006.
- [31] K. Wipke, M. Cuddy, and S. Burch, “ADVISOR 2.1: a user-friendly advanced powertrain simulation using a combined backward/forward approach,” *IEEE Transactions on Vehicular Technology*, vol. 48, no. 6, pp. 1751–1761, 1999.
- [32] X. Wei, L. Guzzella, V. Utkin, and G. Rizzoni, “Model-based fuel optimal control of hybrid electric vehicle using variable structure control systems,” *Journal of Dynamic Systems, Measurement, and Control*, vol. 129, pp. 13–19, 2007.
- [33] A. H. Glattfelder and W. Schaufelberger, *Control Systems with Input and Output Constraints*. Berlin: Springer Verlag, 2003.
- [34] J. Froehlich and J. Krumm, “Route prediction from trip observations,” in *SAE World Congress & Exhibition*, Detroit, MI, 2008, SAE Technical Paper 2008-01-0201.
- [35] L. Serrao, Z. Chehab, Y. Guezennec, and G. Rizzoni, “An aging model of Ni-MH batteries for hybrid electric vehicles,” in *Proceedings of Vehicle Power and Propulsion, IEEE Conference*, Chicago, IL, September 7–9 2005, pp. 78–85.
- [36] S. J. Moura, H. K. Fathy, D. S. Callaway, and J. L. Stein, “A stochastic optimal control approach for power management in plug-in hybrid electric vehicles,” in *Proceedings of the 2008 ASME Dynamic Systems and Controls Conference*, Ann Arbor, MI, USA, 2008.
- [37] C. F. Aquino, “Transient A/F control characteristics of the 5 liter central fuel injection engine,” in *SAE International Congress and Exposition*, Detroit, MI, 1981, SAE Technical Paper 810494.

- [38] M. Locatelli, C. H. Onder, and H. P. Geering, “An easily tunable wall-wetting model for PFI engines,” in *SAE World Congress*, Detroit, MI, 2004, SAE Technical Paper 2004-01-1461.
- [39] G. Rizzoni, L. Guzzella, and B. M. Baumann, “Unified modeling of hybrid electric vehicle drivetrains,” *IEEE Transactions on Mechatronics*, vol. 4, pp. 246–257, 1999.
- [40] M. Morari and J. H. Lee, “Model predictive control: past, present and future,” *Computers & Chemical Engineering*, vol. 23, no. 4-5, pp. 667 – 682, 1999.

Curriculum Vitae

Personal Data

Name	Daniel Ambühl
Date of birth	October 5, 1979
Place of birth	Davos, Switzerland
Citizen of	Davos, Graubünden
Nationality	Swiss
Address	Talstrasse 29, 7270 Davos Platz

Education

1986 – 1992	Primary and secondary school, Davos Platz, Switzerland
1992 – 1999	Schweizerische Alpine Mittelschule, Davos, Switzerland, Matura Typus C
1999 – 1999	Military Service
1999 – 2001	Studies in Mechanical Engineering at EPF Lausanne, 1 st & 2 nd propaedeutic diploma
2001 – 2002	Internship at Liebherr Machines, Bulle
2002 – 2005	Studies in Mechanical Engineering at ETH Zürich, Diploma in April 2005
2005 – 2009	Doctoral student and research/teaching assistant at the Measurement and Control Laboratory, D-MAVT, ETH Zurich